Microstructures and Macrostructures in Rapid Granular Flows

Meng-Lee Tan

A Dissertation

Presented to the Faculty

of Princeton University

in candidacy for the degree

of Doctor of Philosophy

Recommended for Acceptance

by the Program in

Applied and Computational Mathematics

November 1995

Contents

Abstract

This thesis presents complementary numerical and theoretical studies of 2-dimensional dilute monodisperse systems of inelastic rigid disks under force-free and simple shearing conditions. The dynamics of these systems are simulated on a large scale involving $\mathcal{O}(10^5)$ to $\mathcal{O}(10^6)$ disks using the 'event-driven' algorithm for simulating molecular dynamics. It is found that even one of the simplest models for granular 'gases', viz. a collection of inelastically colliding disks in a periodic force-free enclosure, exhibits features that are markedly different from those known of molecular gases. One such feature is the inherent instability of granular systems to inhomogeneous fluctuations, leading to the formation of dense clusters of particles of low kinetic energy within dilute ambients of energetic particles. For a given value of the coefficient of restitution, $\tilde{e}$, these clusters are separated by a typical distance $L_0 \approx l/\sqrt{1 - \tilde{e}^2}$, where l is the mean free path in the corresponding homogeneous system. Clusters are also found in simply sheared ('Lees-Edwards') systems, which, under certain conditions, exhibit a 'stripwise clustering' microstructure whose dominant length scale is also given by L_0. These systems additionally exhibit hysteretic and strongly time-dependent effects, which include the existence of multiple steady states for a given set of externally imposed parameters and a non-linear cluster scattering mechanism which stabilizes the abovementioned microstructure. A theoretical framework explaining clustering in free and sheared systems is provided which is based on equations of motion for granular flows derived elsewhere using kinetic theory. Using this framework, a heuristic model for hysteresis in sheared systems is also derived. The single-particle velocity distribution function for simply sheared systems is accurately measured using a cumulative sampling technique which is effective in filtering noisy simulation data. The measurement shows that the distribution function has the form of an exponential of a second-order polynomial in the norm of the fluctuating velocity with angle-dependent coefficients—a form markedly different from a Gaussian or generalized Gaussian distribution. Numerous diagnostics of free and sheared granular systems, such as their velocity, density, temperature and stress distributions, are also presented throughout this work.

Preface

My debt to Professor Isaac Goldhirsch as mentor and friend is immense. To him I owe my sensitivity to scientific discovery; and in him I found a consistent champion of my causes both academic and personal. My accomplishment would have been be nought if not for his inspiration, genius, generosity, dedication and his love for conversations of great length and diversity.

I also owe particularly my thanks to Professor Steven Orszag for seeing me through five years at Princeton without indigence and for affording me the hospitality of the Fluid Dynamics Research Center and, prior to 1994, a small windowless room on the second floor of Fine Hall reputed then to possess the greatest accumulation of computing power per capita in the world.

Then I must thank Professor Yuehong Qian for encouraging my participation in his work on lattice-BGK models. I am grateful to Dr. Ananias Tomboulides, Dr. Alexei Chekhlov and Dr. Yansi Zhang for many years of guiding influence and fruitful association. Professor Qian and Dr. Tomboulides taught me much about fluid mechanics when I was a junior graduate student. Dr. Chekhlov and Zhang were my officemates and must thus be thanked for having to endure my perennial presence in the office. I am grateful to Dr. Chekhlov in particular for having interspersed the writing of my thesis with many hours of exasparating discussions on polydisperse topics.

My thesis so written passed into the hands of Professors Sankaran Sundaresan (my principal reader after Professor Goldhirsch), Philip Holmes and Salvatore Torquato, where it was fortunate enough to have received much constructive criticism. I am especially grateful to Professor Sundaresan for his detailed comments and corrections.

Much of the work presented in Chapter 1 was done in collaboration with Professor Goldhirsch and Dr. Gianluigi Zanetti. This work was published in the Journal of Scientific Computing, Vol. 8, No. 1, 1993, in an article entitled 'A Molecular Dynamical Study of Granular Fluids I: The Unforced Granular Gas in Two Dimensions'. Dr. Zanetti wrote much of the original 'event-driven' computer code for simulating molecular dynamics, and I learnt while working with him the art of writing superlative codes—ones truly beyond the reach of our competing researchers in terms of

speed and resolution—for massive computations.

Professor Goldhirsch also provided me with most of the seminal ideas for the work in the later chapters of this thesis. Indeed he has been involved, as it were, 'on both the macroscopic and microscopic levels' of this work, from the broad theoretical overview to many of the fine computational details. However, I must disclaim his responsibility for any errors in my thesis—the responsibility for these lies solely with me.

Finally I must thank Dr. Youngjai Kiem for many years of friendship and also my teachers, colleagues and friends at Princeton University too numerous to mention here who had contributed one way or another to my thesis.

This thesis is dedicated to the memory of my first four-hour long conversation with Isaac Goldhirsch in the winter of 1991.

Princeton, New Jersey   M-L.T.
May 1995

Chapter 1

Introduction

The notion of a granular 'fluid'[1, 2, 3, 4] arises when a system of macroscopic parti-
cles, such as sand or coal particles, are subject to such rapid deformation that contacts
between individual grains do not endure and their motion is rapidly randomized by
frequent collisions. The behavior of the system is analogous to that of a classical fluid,
except that the collisions are inelastic. It is understood that in a granular system the
effect of the interstitial fluid on the dynamics of the particles can be neglected. It is
emphasized that despite the analogy, granular fluids are rheologically very different
from classical fluids. They exhibit many extraordinary phenomena whose source lies,
in many cases, entirely in the inelasticity of the grain-grain interaction. Thus even an
idealized system of identical rigid spheres interacting inelastically—a system differing
from the classical hard-sphere fluid only in the inelasticity of the interaction—is char-
acterized by extraordinary properties such as clustering instability, hysteresis, phase
transitions, singularities in the collision rate and more.

Perhaps the most significant difference between a granular fluid and a regular one
is the inherent and generic inhomogeneity of the former under virtually any external
conditions. There is a tendency for granular fluids to form dense clusters of particles
of low internal kinetic energy within dilute ambients of energetic particles. These
clusters and other related 'inelastic microstructure' are ubiquitous in granular flows.
They have been observed in numerical studies of externally driven and unforced sys-
tems. Among the granular flows studied in this work is the free flow of inelastic disks,

i.e. a flow that is not subject to any external forcing. Such a flow, even if initially prepared in a homogeneous state with an isotropic velocity distribution and a vanishing mean velocity, develops readily into a highly inhomogeneous state consisting of meandering dense particle clusters as the energy is dissipated in inelastic collisions. The mechanism responsible for clustering is shown in Chapter 2 to be the interaction between long-wavelength hydrodynamic modes and local dissipative processes. Clusters also form in steady state flows such as highly inelastic simple shear flows ('Lees-Edwards' systems), in which dense anisotropic clusters with a preferred direction of alignment are created in a complex nonlinear process explained in Chapter 3. Another phenomenon peculiar to granular fluids is the presence of hysteresis leading to multiple steady states characterized by the same set of external parameters. This phenomenon is explored in Chapter 4. A accurate study of the single-particle distribution function, a long-sought quantity central to kinetic theories of granular flows (cf. Refs. [5, 6, 7, 8] and references therein), is presented in Chapter 5. This study shows that the distribution function is nonanalytic, highly anisotropic and thus markedly different from a Gaussian or generalized Gaussian distribution.

There is a multitude of interesting phenomena, in addition to the ones mentioned above, that are peculiar to granular systems. They include normal stress differences[9, 10], $1/f$ noise, nonlinear waves, convection rolls[1], inelastic collapse[11, 12, 13], sensitivity to boundary conditions, segregation[14], layering, heaping[15] and the formation of extended plugs[16]. Some of these phenomena are surveyed in this chapter. A discussion of the broader scientific and industrial context in which the main focus of this work, viz. rapid granular flows, lies is provided here as well.

1.1 The Rheology of Granular Materials

The 'simple pile of sand', after having been the subject of a scientific controversy involving a theory of self-organized criticality[17, 18], springs to mind as the archetype of a granular material. Although real sandpiles are largely static structures except for the surface flows that occur during an avalanche, they are already characterized by many properties that typify granular systems, including systems under rapid defor-

mation. A sandpile is stationary (i.e. no avalanche will occur) as long as its surface angle is less than the angle of repose, θ_c. The stationarity persists until the slope is increased beyond the 'maximum angle of stability', θ_m. However, because of hysteresis real sandpiles are characterized by a range of angles of repose[19] rather than a single angle. Their hysteretic behavior is due to the lack of 'thermalization' in the dynamics in the absence of energetic external perturbations. Thus a sandpile will retain a memory of its earlier configuration and its stationary states are history-dependent.

The existence of history-dependent steady states appear to be a common feature of granular systems. For example, two different flow states may exist in a chute flow for given values of the chute angle and flow rate[20]. These states correspond to an 'energetic' flow and a 'quiesent' flow. As shown in Ref. [20], the former is produced when the flow is initiated by dropping particles from a height into the chute and the latter by gating the entry of the particles into the chute. The flow state is strongly dependent on the manner in which it is initiated: the energetic flow is initiated by particles which are already energetic as they enter the chute, while the quiescent flow starts as an inert and dense slug of particles that moves slowly into the chute through a controlled entrance.

The bifurcation into two (or more) markedly different steady states is also observed in a simple shear flow. The character of the steady state in this case depends strongly on the initial condition and the application of transient forces. In particular, it depends on whether the initial flow configuration allows for continual thermalization. As discussed in Chapter 4, the transition from a thermalized state to a 'plugged' state with large but thermally unexcited clusters of particles occurs when the system is allowed to disengage itself from the source of its forcing or thermal excitation, viz. the shearing boundaries. If the system remains in contact with its thermalizing source, a 'gaseous' state with a highly time-dependent microstructure is obtained.

Returning to the subject of sandpiles, the fact that avalanches only occur when the slope, θ, of the sandpile exceeds θ_m—otherwise the sandpile is stationary—suggests that a generalized phase transition occurs at $\theta = \theta_m$. It turns out that the initiation of an avalanche resembles more a nucleation and growth process than a critical phenomenon, and thus the phase transition is probably of the first order[21]. A process

that resembles a first-order phase transition also occurs in the decay of a free granular gas. In this case, as mentioned above, a transition from an energetic homogeneous state to a highly inhomogeneous state consisting of clusters occurs as the energy is dissipated in inelastic collisions. The global statistical properties of the two states are well-defined. The transition is induced by fluctuations and a positive feedback mechanism involving the interplay of collisional 'cooling' and mass aggregation (cf. Chapter 2).

Other parallels between the properties of a sandpile and those of granular materials in general can also be drawn. An interesting example is the following: the free surface of a sandpile may respond in one of the two following ways to a noisy external pertubation (such as shaking). If the perturbation is of small amplitude, a collective reorganization or 'relaxation' (cf. [18]) of particles within a local group of particles may occur so that a configuration of lower potential energy is achieved. This reorganization leads to more efficient filling of voids and hence to a more stable configuration for the sandpile. If the perturbation is of large amplitude, particles are ejected individually from their groups(the so-called 'independent-particle relaxation' process, cf. Ref. [18]) and travel down the pile. It appears that collective relaxation may also occur in more complex flows in which particle motions are randomized to a greater or lesser extent by collisions. In Fig. 1.1, we show the particle configuration in a hopper in the process of being emptied[16]. A group of particles in a regular close-packed array can be seen near the exit amid more dilute ambients of energetic particles. In the chute flow shown in Fig. 1.2, regularly packed piles of particles can be seen moving along the chute floor[16]. The energetic ambient around a group of particles serves as the noisy external perturbation that brings about their collective relaxation to a regular close packing. It appears that regular packings are the norm rather than random packings, indicating that collective relaxation may be a very common phenomenon in granular systems.

Granular materials are of course hardly limited to sandpiles and in fact appear in an extremely wide range of natural and industrial settings. Most terrestrial granular materials are aggregates of macroscopic solid particles whose typical linear sizes range from microns for very fine powders to tens of meters for rocks and boulders. These
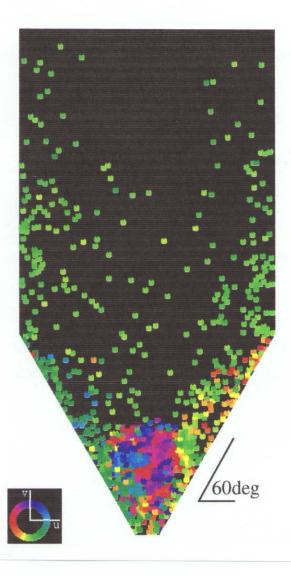
Figure 1.1: The particle configuration in a hopper which is being emptied. The flow is computed using a Runge-Kutta scheme involving an 'overlap' algorithm as described in [16, 22]. Frictional effects and normal restitution involving slight deformability are accounted for in the algorithm. The flow is driven by gravity pointing vertically downwards. The particles are colored according to the direction of their velocity as indicated in the inset. Notice the dense regular packing of particles near the exit.
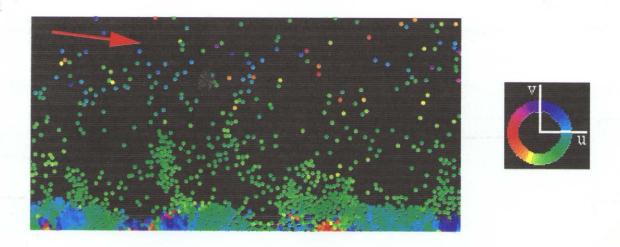
Figure 1.2: The particle configuration in a chute flow of slightly deformable frictional disks. The direction of the gravitational acceleration is indicated by the arrow in the upper left corner of the plot. The flow is computed in the same way as the flow shown in Fig. 1.1. Notice the mounds of regularly packed particles on the chute floor.

materials include fine and relatively uniform particulates, such as pills, grains and condiments, common in the pharmaceutical and food industries; they also include irregular bulk solids such as coal, soil and silicates used in the energy and construction industries. Granular flows also occur in many geological and environmental processes such as avalanches, pollutant dispersion and the movement of the arctic ice pack. They may also be relevant in extraterrestrial contexts such as the dynamics of asteriod belts[23] and interstellar dust, and the coagulation of planetesimal bodies to planets at the early stage of the development of the solar system.

A granular system would not respond to very weak shear stresses, since they cannot overcome the frictional 'bonds' among the grains. In this case, the system is elastic at small compressive deformations and is therefore solid-like. Under these conditions, effects such as arching and formation of stress chains and shear bands[1, 21] are observed. However, the system is not truly a solid since it disintegrates under tensile stresses and it is plastic at larger deformations. When slightly stronger stresses are applied, some 'weak' bonds in the system could be overcome and some

blocks of grains may move along slippage planes. Under even stronger stresses, more frictional bonds are broken and smaller blocks may be set in rapid motion. When the shear stresses are strong enough, all bonds are broken and the grains are no longer in permanent contact with each other. They interact mainly through instantaneous impulsive collisions and their dynamics resembles that of a molecular gas, the main difference being that the collisions are inelastic. As mentioned earlier, this difference turns out to be a source of a large number of phenomena distinguishing granular 'gases' from regular ones. Some of these phenomena are described in Section 1.2.

In general, a granular system may contain within itself a mixture of solid-like and fluid-like phases. The former phase is either quasistatic or in uniform bulk motion, and has low kinetic energy, while the latter phase is rapidly deforming and energetic. Most granular flows of practical interest are such that the rapidly flowing phase, which is relatively dilute, will border solid-like quasistatic domains which are dense. Flows of this kind are observed in silos, chute flows, avalanches, entrainment flows (pneumatic transport systems[24]), and rotating or Taylor-Couette flows (separation cyclones[25]). Completely fluidized granular materials exhibit a variety of complex and, in many cases, strongly time-dependent microstructures such as clusters, layers, heaps and plugs. They also exhibit multistable and hysteretic behavior under many conditions. In a nutshell, granular materials are generically inhomogeneous; they are characterized by complex microstructures; and both their statics and dynamics are strongly dependent on history, boundary conditions, and particle properties.

1.2   Rapid Granular Flows and Kinetic Theory

In this section, we focus on the granular systems in the rapid flow regime. We give a brief survey of some of the phenomena that have been observed in these systems, particularly model systems which are realized numerically in computer simulations. We have mentioned the tendency of an unforced system to undergo a transition to a highly heterogeneous state consisting of meandering dense clusters even when the initial state is statistically homogeneous. We also mentioned the formation of anisotropic domains of high density in very inelastic shear flows. In a chute flow that has become

sufficiently energetic after prolonged acceleration, a transition will occur between a state of uniform bulk motion and another state consisting of separated clusters moving independently of each other[26, 27]. If the inclination of the chute is small, the flow can be driven to saturation, i.e. to a state in which the rate of frictional loss of kinetic energy balances the rate of energy input (through gravitational acceleration) into the system. When this happens, the clusters may dominate the dynamics of the system by coalescing into a levitated plug in which most of the mass is concentrated. In a convection cell in which grains are bound between vertical walls and fluidized by a horizontal vibrating plate, coherent horizontal motion will develop within a falling and converging packing of grains near the plate where most of the vertical velocity has been dissipated in inelastic collisions. The grains near the plate move mostly horizontally and graze each other, and the horizontal motion arises because the inelasticity has the effect of aligning the velocities of particles undergoing grazing collisions. The motion may be coherent enough to cause a long horizontal stream of particles to move along the plate, and a cluster or heap of particles is formed when two such streams moving in opposite directions merge[15].

Cluster formation appears to be a generic feature not only in granular flows but also in many other particulate flows in which the effect of the interstitial fluid is not negligible. Examples of such flows include bidisperse particles sedimenting in a viscous fluid[28, 29], vertically conveyed suspensions[30], low-Reynolds number sheared suspensions[31], fluidized beds[32, 33, 34] and more[31]. In studies of vertical risers (cf. e.g. [33] and references therein), an analogy is drawn between the turbulent motion of the particles as they are conveyed by a rising gas column to the thermal motion of molecules. This leads to the concept of a 'granular temperature' for the system, i.e. the average fluctuating kinetic energy density associated with the motion of the particles. It is found that the particles tend to aggregate in regions of low granular temperature, a fact that is in accord, as we shall amply see in this work, with our observations of clustering in numerically simulated systems of inelastics disks and spheres. The clustering processes in colloidal systems also bear an interesting, and perhaps not entirely superficial, similarity to the those in granular flows. The insights gained from the study of the latter flows (which are at any rate more ac-

cessible to numerical simulation) may be useful for the study of the former. In a sedimenting bidisperse suspension, particles from the same species tend to coalesce in low-shear and high-velocity vertical streams that are surrounded by a highly sheared 'lubrication' layer of interstitial fluid[28]. These streams of particles separate into smaller streams as the relative velocity between the stream and the lubrication layer increases. This is reminiscent of the clustering process in a granular flow. A region in such a flow whose shear rate is lower will have a lower pressure and vice versa. The region whose shear rate is comparatively lower than the shear rate in an adjoining region will tend to become denser, and may thus eventually become a cluster, since particles are driven into it from the adjoining region whose pressure is higher. In the reverse process, a large cluster may also break up into smaller clusters due to differential shearing within its interior. The clustering process will be discussed in detail in Chapter 3.

Many rapid granular flows are found under different parametric conditions to be in one of two distinctly different states or 'phases'. These phases will be refered to as the 'quasihomogeneous phase' and the 'inhomogeneous phase'. The classification is based on the degree of inhomogeneity in the system. The phase in which the system is found depends on whether a characteristic intercluster distance can be accomodated in it. Note that we are speaking of different phases in a rapidly flowing system, i.e. one that is completely fluidized; clearly, a partially fluidized system may have more than two phases. The intercluster distance, L_0, is independent of the linear dimension of the system and is given by

$$L_0 \approx \frac{l}{\sqrt{1 - \tilde{e}^2}} \qquad (1.1)$$

where l is the mean free path for the corresponding homogeneous flow. A derivation and numerical verification of this relationship relevant to the case of an unforced granular system is given in Chapter 2. In a nearly elastic system or one with a small number of particles, L_0 is usually larger than the linear dimension of the system. Therefore no clusters can be accomodated in it and clustering effects are absent. However, the system is still inhomogeneous on the scale of its linear dimension and is therefore in the quasihomogeneous phase. In a very inelastic system or one with a large number of particles, dense interspersed clusters are created whose typical

separation is given by L_0. The system in this case is in the inhomogeneous phase. The bifurcation into these two phases therefore depends on whether the linear dimension of the system is larger than L_0. For a fixed system volume, this statement may also be cast in terms of the number of particles in the system as whether the number is larger than a given threshold. We will discuss this relationship in more detail in Chapter 2. We will also present numerical evidence in Chapter 3 to show that it applies to sheared systems as well.

The above-mentioned classification can be applied to unforced systems of rigid inelastic disks and spheres that are allowed to evolve from isotropic and homogeneous initial states. If the collisions are nearly elastic, a slightly inhomogeneous and persisting sheared configuration will develop after some time in which two thick layers of particles, which together span the linear dimension of the system, move in opposite directions. If the collisions are highly inelastic, a highly inhomogeneous state consisting of prominent clusters are formed. Both phases are found to be statistically well-defined, since they are characterized by global statistical properties, such as the flatness of the velocity distribution and the average energy decay rate, that are stationary in time. The bifurcation also parallels the behavior of a one-dimensional unforced system in which both stationary or oscillatory (i.e. 'pulsating') clusters of particles can be created depending on the inelasticity and the size of the system[11, 12, 13].

In addition to the phenomenon of clustering, an effect known as 'inelastic collapse', which is related to clustering, has also been observed in unforced systems whose collisions are instantaneous and characterized by a constant coefficient of restitution. This effect corresponds to a singularity in the dynamics of such systems. It occurs when a group of particles 'cools' so quickly as a result of the dissipative collisions that they are drawn together faster than the diffusive stresses could pull them apart. When this happens, an infinite number of collisions may occur in finite time. This singularity, or 'inelastic collapse', has been observed in numerically simulated one-dimensional unforced systems of rigid point particles [11, 12, 13] and two-dimensional unforced systems of disks[35]. A simple example of this singularity is that of a ball bouncing inelastically on a floor, for which one can easily show that the ball comes to rest after an infinite number of collisions in a time $2u/g(1 - \tilde{e})$, where u is the initial

velocity, g the acceleration due to gravity and $\tilde{e}$ the coefficient of restitution. Away from solid boundaries, inelastic collapse can occur, for example, when two particles converge on a third that is sandwiched between the two, and the sandwiched particle bounces back and forth between the two outer particles. The three of them eventually coalesce in finite time after an infinite number of collisions. In two-dimensional un-forced systems, contiguous particles embedded within a larger group of particles may organize themselves into straight chain-like structures in which the inelastic collapse occurs.

Many theories for rapid granular flows are substantially based on analogies with the dynamics of molecular fluids. In such a theory due to Haff[4], the equations of motion are derived phenomenologically and are similar to the Navier-Stokes equations except for the equation for the granular temperature, i.e. the fluctuating kinetic energy density. The latter equation is notably different because it contains an energy sink term that represents the rate of loss of kinetic energy due to inelastic collisions. Other theories for granular flows are based on continuum mechanical approaches[36], while still others involve the derivation of constitutive relations on the basis of the classical kinetic theory of gases. It is assumed in the latter theories that the pertinent field variables are the same as those in standard hydrodynamics. A typical output of these theories[2, 5, 6, 7, 8] (generically refered to as kinetic theories for granular flow) is a set of macroscopic equations of motion which, like in Haff's theory, closely resembles the Navier-Stokes equations except for the temperature equation. It is assumed in these kinetic theories that the single-particle distribution function is Gaussian with corrections due to gradients in the intensive variables similar to those obtained in the Chapman-Enskog expansion[37]. One disadvantage of these theories is that they predict a vanishing normal stress difference, in contrast with numerical and experimental results[22].

The normal stress difference, or the so-called 'anisotropic pressure', can be accounted for when the single-particle distribution function is assumed to be a generalized Gaussian, as is done in Refs. [38, 39]. The theories derived in Refs. [38, 39] involve an equation of motion for the second-order tensor of the fluctuating velocity correlations. This tensor may perhaps more descriptively be called the 'tensorial

granular temperature', and it is the equivalent of the Reynolds stress in hydrodynamics. The theories involving this quantity have been moderately successful in predicting results of numerical experiments. Nevertheless, deviations of the numerical results from theoretical predictions (e.g. deviations of the value of the stress tensor) have been observed[10], the deviations being particularly pronounced when strong microstructures are present. These microstructures have the effect of decreasing the values of the stresses with respect to the values that are expected in the absence of microstructures. The fact that the kinetic theories based on the generalized Gaussian distribution function are more successful than those which include only the standard hydrodynamic variables indicates that the set of macrovariables for which equations of motion are to be derived should be enlarged by including in it the tensorial granular temperature.

The deviation of the values of the usual macrovariables, such as the mass and momentum densities and the stress tensor, from their values predicted by the kinetic theories can be significant when the system is very large relative to L_0 given by (1.1). In this case, the system contains clusters and is highly inhomogeneous. The deviation is not surprising, since many kinetic theories assume that the system is void of internal structure and some of them assume that it is isotropic as well. The theory based on the generalized Gaussian distribution function does account for the anisotropy in the fluctuating velocity correlations but nonetheless assumes spatial homogeneity in the flow. The stresses predicted by this theory were compared in detail in a previous study[40] to those measured in computer simulations. In essence, the comparison indicates that for a given number of particles and a given average solid fraction (ratio of volume of particles to total volume), the stresses are weak, that is, they are much lower than the theoretical value, if the system is very inelastic; and conversely, they are strong, and closer to the theoretical value, if the system is nearly elastic. Since clusters are broken up by stresses whose magnitude decrease with increasing inelasticity, a very inelastic system will contain dense clusters while a nearly inelastic system will be cluster-free. We will show in Chapter 3 that this trend is anticipated by (1.1) which may be used to meaningfully organize the data published in Ref. [40].

From another perspective, the fact that the dynamics of granular systems are usually dominated by anisotropic particle clustering also implies that additional macrovariables which account for the anisotropy must be included in any successful kinetic theory of these systems. Indeed, our study presented in Chapter 5 of the single-particle distribution function for a two-dimensional granular shear flow shows that it has a highly anisotropic structure. This function has the form $\exp[b_0(\theta) + b_1(\theta)v + b_2(\theta)v^2]$, where v is the magnitude of the local fluctuating velocity, θ is the angle between the direction of the fluctuating velocity and the streamwise direction, and b_0, b_1, and b_2 are coefficients that depend strongly on θ. The presence of the linear term in v renders the distribution function non-analytic in the Cartesian components of the fluctuating velocity. It also renders the distribution unrepresentable as a Gaussian or generalized Gaussian. It has a much more complicated angular structure than those of the distribution functions that have been assumed in existing kinetic theories. Its strong angular dependence evidently necessitates the use of an extended set of macrovariables including not only the standard hydrodynamic variables but also other variables which account for the angular anisotropy in the flow.

The study of unforced one-dimensional granular systems presented in Ref. [13] shows that a proper hydrodynamic description of one-dimensional unforced systems already requires the addition of a hydrodynamic variable that measures the asymmetry of the single-particle distribution function. We note here that the anisotropy is present in three-dimensional shear flows as well[16]. In these flows, the dependence of the single-particle distribution function on the angle between the direction of the fluctuating velocity and the streamwise direction (i.e. the 'azimuthal angle' relative to the 'z-axis' which is taken to coincide with the streamwise direction) is found to be highly anisotropic, although the dependence on the angle between the fluctuating velocity and a reference direction normal to the streamwise direction (i.e. the 'polar angle') is found to be weak. The dependence on the 'azimuthal angle' appears to parallel the corresponding dependence on θ in the two-dimensional case. In particular, it is found that only even modes are present in both angular dependences due to the fact that the simple shear flow has a rotation by π symmetry. Given that particle clusters may have a profound effect on the distribution functions characterizing

granular flows, an understanding of the dynamics of these clusters will therefore bear directly on the derivation of kinetic theories for granular flows.

1.3 Molecular Dynamics Simulations: A Minimal-Model Approach

Unlike conventional fluid dynamics, a unified description of the flow of bulk materials is difficult to obtain and existing models are strongly dependent on particular material properties or flow geometries. Until recently, non-invasive experimental diagnostics are hard to obtain, though it is now possible to non-invasively measure the velocity and concentration in flows of certain classes of materials using magnetic resonance imaging techniques[41]. Recent efforts at understanding the fundamental behavior of granular systems have focused upon the macroscopic behavior of systems of identical rigid particles whose collisions are governed by simple models involving one or two coefficients of restitution. These efforts include the derivation of kinetic theories (which we have already discussed) and the study of the macroscopic properties of these systems realized computationally in large-scale computer simulations. The simulations are usually molecular dynamics (MD) simulations in which the entire set of coupled equations of motion for the particles are solved using a 'collision search and execute' algorithm. The advantages of large-scale MD simulations are, firstly, the ability to study the dynamics at a level of detail that cannot be achieved in physical experiments; secondly, the ease and flexibility with which parametric dependences may be studied; and thirdly, the minimal-model approach that eliminates reliance on a specific continuum description whose validity may be questionable. With sophisticated algorithms, it is possible to perform MD simulations of granular flows in complex geometries and at various levels from small systems of $\mathcal{O}(10^3)$ particles which are strongly influenced by boundary conditions to multimillion particle systems with complex internal dynamics.

It is well-known in statistical mechanics that the macroscopic properties of many-body systems depend only weakly on the particular nature of the microscopic interactions (assuming that the appropriate separation of scales exists in the system).

As an aside, the fact that the macrodynamical equations of motion do not depend on the microscopic dynamics is the basis for 'discrete fluid dynamics', i.e. numerical schemes for solving the Navier-Stokes equations such as the lattice-gas cellular automata and related methods which use a discrete and highly stylized underlying particle dynamics. The particle dynamics retains only enough relevant microscopic physics to reproduce the requisite macroscopic dynamics of the Navier-Stokes equations. Following these ideas, we have derived in Ref. [42] a lattice-gas method to solve macroscopic equations for granular flows. To return to the subject of granular flows, it is clear that even if the microscopic dynamics are not completely captured by the interaction model used in the computer simulations or the kinetic theories, we may still obtain qualitatively correct results on the macroscopic level. In fact, by studying macroscopic data as a function of microscopic parameters, we may tune the microscopic parameters to obtain desired macroscopic behavior that matches, say, the observations in a physical experiment. In this way, we may deduce the values of the microscopic parameters which are inaccessible to direct measurement in the experiment. It is also possible to extrapolate the results of the physical experiment to different set-ups using a 'properly tuned' numerical experiment.

The numerical method used in this work is the 'event-driven' method which has proved to be highly efficient in computing the collective dynamics of rigid particles. This method and its performance are discussed in detail in Appendix A.

1.4   The Rigid-Disk System

Here we define system which is simulated and the various macroscopic diagnostics that are used throughout this work.

1.4.1   The Model

The system consists of N identical smooth rigid disks of unit mass and diameter σ in a rectangular enclosure of size $L_x \times L_y$. This enclosure is periodically extended in both the x- and y-directions. The periodic boundary conditions are either applied in the static frame, in which case no external stresses are exerted on the system, or in the

Lagrangian frame (corresponding to a given average velocity profile) for shear flow, in which case the system is sheared by its periodic images. Both types of boundary conditions are explained in detail in Section 1.4.2. The only allowed interactions in the system are instantaneous collisions of pairs of disks. The collisions occur either between two disks lying within the enclosure or between one in the enclosure and another in a periodic image of the enclosure. The velocity of each disk is constant between collisions. The collision process is characterized by a constant coefficient of normal restitution, $\tilde{e}$, with $0 < \tilde{e} < 1$, which, when combined with the conservation of linear momentum, determines the outcome of the collision. Frictional interactions are ignored (simulations with frictional degrees of freedom are presented in Appendix C and Ref. [16]). Let $\mathbf{v}_1$ and $\mathbf{v}_2$ be the respective velocities of two disks prior to a collision and let $\mathbf{v}'_1$ and $\mathbf{v}'_2$ be the corresponding velocities immediately following the collision. A straightforward calculation yields:

$$
\begin{aligned}
\mathbf{v}'_1 &= \mathbf{v}_1 - \frac{(1+\tilde{e})}{2}(\mathbf{v}_{21} \cdot \hat{\mathbf{k}})\hat{\mathbf{k}} \\
\mathbf{v}'_2 &= \mathbf{v}_2 + \frac{(1+\tilde{e})}{2}(\mathbf{v}_{21} \cdot \hat{\mathbf{k}})\hat{\mathbf{k}}
\end{aligned}
\tag{1.2}
$$

where $\mathbf{v}_{21} \equiv \mathbf{v}_1 - \mathbf{v}_2$ and $\hat{\mathbf{k}}$ is the unit vector pointing from the center of disk '1' to the center of disk '2', at the time of contact (cf. Figure 1.3).

1.4.2 Initial and Boundary Conditions

As already mentioned, two types of boundary conditions are imposed in the simulations. The first corresponds to fully periodic boundary conditions at opposite sides of the rectangular enclosure, i.e. a particle about to leave one side will reappear at the other side at an equivalent position with the same velocity. The second type is the 'Lees-Edwards' boundary conditions[43] which were originally employed to study transport properties of simple fluids. They were also used before in simulations of granular systems[10, 22, 40, 44]. They lead to a state of simple (linear) shear without the need to formulate a wall boundary condition—formulating wall boundary conditions for granular flows is a nontrivial problem; see e.g. Ref. [45]. An algorithmic definition of these boundary conditions, useful for implementation on the computer,
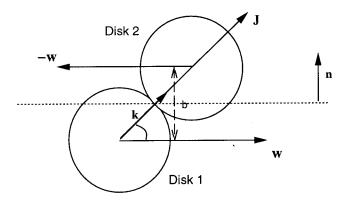
Figure 1.3: Collision model: $\mathbf{w} = (\mathbf{v}_1 - \mathbf{v}_2)/2$ is the relative velocity in the center-of-mass frame and $\mathbf{J} = \frac{(1+\tilde{e})}{2}(\mathbf{v}_{21} \cdot \mathbf{k})\mathbf{k}$ is the impulse imparted to disk 2 by disk 1. The impact parameter b, defined as $\sigma |\mathbf{k} \times \mathbf{v}_{21}|/|\mathbf{v}_{21}|$, is a property of the collision.

can be found in [10, 40]. They can also be defined analytically, since, as mentioned, they correspond to fully periodic boundary conditions applied in the Lagrangian frame for the shear flow[46].

The Lees-Edwards conditions can be stated as follows: the enclosure containing the disks is to be regarded as a fluid element sheared by adjacent periodic images at the top and at the bottom. The geometrical centers of these images move with speeds $\pm U$ in opposite directions parallel to the x-axis (see Fig. 1.4). Effectively, the upper and lower boundaries of the enclosure move with velocities equal to $U/2$ and $-U/2$ respectively. The value of U is given as a parameter of the simulation. The periodicity in the x-direction is imposed by requiring a particle incident on, say, the right side to reenter the left side at an equivalent position with the same velocity. In the y-direction, a particle incident on, say, the bottom boundary reenters the top boundary at a position that reflects the displacement of the top periodic image. Upon its reentry, the particle's horizontal velocity is increased by U, in accordance with the interpretation that the particle is entering the fluid element from an adjacent faster-moving element. An analogous protocol applies to particles leaving the top boundary.

The initial condition for the simple shear flow simulation is similar to the one used in Ref. [40]. It corresponds to the sheared configuration for an elastic hard-disk
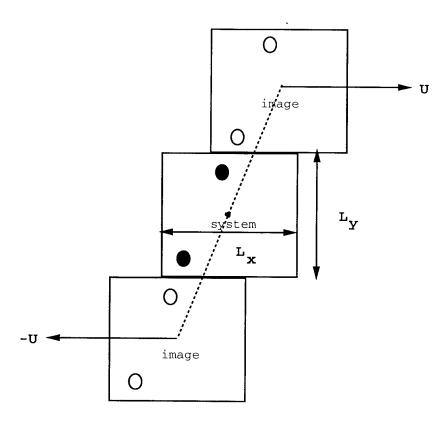
Figure 1.4: The Lees-Edwards boundary condition. The open and solid circles show the relative positions of the disks and their images respectively.

gas. To achieve this configuration, the disks are first uniformly distributed inside the enclosure with velocities drawn from a Gaussian distribution with zero mean and a variance that corresponds to the desired value of the initial temperature. To the (random) velocity assigned to each disk, a mean velocity corresponding to the location of the disk in the enclosure is then added. This mean velocity is taken to be a linear interpolation between the velocities at the horizontal boundaries, and as is shown in Chapter 3, the mean velocity profile persists throughout the simulation. This is a consequence of using the Lees-Edwards boundary condition and a sheared initial configuration. A mean velocity profile that is not linear can be obtained if other types of initial conditions are used (cf. Chapter 4). Since the velocities of the particles are assigned by a random number generator, the total momentum of the system need not vanish. To assure that the experiment is performed on a system with no net total momentum, the total initial momentum $\mathbf{P}$ of the N particles is computed and an amount $\mathbf{P}/N$ is subtracted from the momentum assigned to each particle. Next a simulation of the above system with elastic collisions is performed in order to achieve a state corresponding to that of a sheared molecular gas. After this is done, the initial configuration is ready and the inelastic simulation is started by applying the Lees-Edwards boundary condition together with (1.2) to all collisions following this configuration.

The initial condition for the periodic unforced system is obtained in a similar way except that a mean velocity is not added to the random velocities of the disks.

1.4.3 Definition of the Macrofields

Here we define the manner in which the most common macrofields are computed from data obtained from the simulations. Some other less common macrofields and diagnostics are also used in this work; they are defined as they occur. The density field, $\rho(\mathbf{r})$, is defined (in a rather usual way) by partitioning the flow domain into an array of identical rectangular cells and counting the number of particles in each cell (the particles are assumed to have unit mass). The position $\mathbf{r}$ is taken to be the position vector of the center of the cell. The macroscopic velocity field, $\mathbf{V}(\mathbf{r})$, is obtained by computing the ratio of the total momentum to the total mass in each

cell. The granular temperature in a cell is defined as

$$T(\mathbf{r}) \equiv \frac{1}{2}\langle (\mathbf{v} - \mathbf{V}(\mathbf{r}))^2 \rangle \tag{1.3}$$

where $\mathbf{v}$ denotes the velocity of a particle in the cell, and $\langle \cdots \rangle$ denotes an average over all particles in the cell.

Next, we define the stress tensor, $\tau(\mathbf{r})$, which is a sum of two contributions: a 'kinetic' contribution that accounts for the transport of momentum as the particles move, and a 'collisional' contribution that accounts for the transfer of momentum as the particles collide [40, 10, 9]. For a given configuration, the kinetic stress tensor is given by

$$\tau^{(k)}(\mathbf{r}) = \rho(\mathbf{r}) \begin{pmatrix} \langle v_x'^2 \rangle & \langle v_x' v_y' \rangle \\ \langle v_x' v_y' \rangle & \langle v_y'^2 \rangle \end{pmatrix} \tag{1.4}$$

where $v_x' \equiv v_x - V_x(\mathbf{r})$ and $v_y' \equiv v_y - V_y(\mathbf{r})$, and $\langle \cdots \rangle$ denotes, as before, an average over all the particles in a cell. A product like $\langle v_x' v_y' \rangle$, for example, is computed using the identity:

$$\langle v_x' v_y' \rangle = \langle v_x v_y \rangle - \langle v_x \rangle \langle v_y \rangle. \tag{1.5}$$

The collisional stress tensor is computed as follows (cf. Section 16.4 in Ref. [37]): A collision between two rigid disks involves an impulse, $\mathbf{J}$, which is tranfered from, say, disk 2 to disk 1 over a distance equal to the particle diameter, σ. The magnitude of $\mathbf{J}$ is equal to the magnitude of the change in the momentum of each of the colliding particles, and the direction of $\mathbf{J}$ is along $\mathbf{k}$ (see Fig. 1.3). Hence in a single collision an amount of momentum $\mathbf{J}(\mathbf{k} \cdot \mathbf{n})$ is transfered across a surface whose normal vector is $\mathbf{n}$ as shown in Fig. 1.3. Writing $\mathbf{J}(\mathbf{k} \cdot \mathbf{n}) = (\mathbf{Jk}) \cdot \mathbf{n}$, the collisional contribution, $\tau^{(c)}(\mathbf{r})$, is obtained by considering collisions occurring within a cell of volume V in a time interval t and averaging the dyadic product $\mathbf{Jk}$ over these collisions:

$$\tau_c = \frac{\sigma}{Vt} \sum_{\text{collisions}} \mathbf{Jk} \tag{1.6}$$

The total stress tensor is then given by

$$\tau(\mathbf{r}) \equiv \tau^{(k)}(\mathbf{r}) + \tau^{(c)}(\mathbf{r}). \tag{1.7}$$

The kinetic and collisional pressures are defined as one-half the traces of the corresponding stress tensors.

The global average granular temperature, $\overline{T}$, is defined as the average of $T(\mathbf{r})$ over all cells in the system. The variation of $\overline{T}$ can be used to gauge the convergence of the system to a steady state, since $\overline{T}$ approaches, and then fluctuates around, an equilibrium value when this occurs. Another useful diagnostic is the flatness (kurtosis), κ, of the distribution of fluctuating velocities, which is defined as

$$\kappa = \frac{\overline{v'^4}}{\overline{v'^2}^2} \tag{1.8}$$

where the overbar denotes an average over all particles in the system.

1.5 Goals of this Work

While it is clear that the behavior of a granular fluid can be markedly different from that of a Newtonian fluid, and that the expectations and intuition gained from the study of the latter may not apply to the former, the analogy between Newtonian and granular fluids has been exploited in many theories for granular flows. As mentioned in Section 1.2, many kinetic theories for granular flows produce macrodynamical equations of motion which include an equation for the granular temperature that accounts for the energy dissipated in inelastic collisions, in addition to the usual equations for the mass and momentum densities. In more sophisticated theories, an equation is derived for each component of the tensorial granular temperature (i.e. the second-order tensor moment of the fluctuating velocity). Although these theories are moderately successful in predicting some results of physical and numerical experiments, such as the value of the stresses observed in numerical simulations, they fall short in many respects, most of which have to do with the fact that the effect of inhomogeneities and microstructures (which occur generically in all granular flows) are not taken into account. For example, the inelastic microstructure that forms in a shear flow has a significant effect on the stresses in the flow, but this fact has not been considered in the above theories.

More fundamentally, the statistical mechanics of a granular fluid lacks the simplifying feature of detailed statistical balance, since its dynamics are not time-reversal invariant on the level of the grain-grain interaction (i.e. the 'microscopic' level). More-

over, the fundamental statistical behavior of even idealized granular systems, such as those consisting of identical disks or spheres whose collisions are characterized by one or two coefficients of restitution, in terms of the probability distribution functions of particle properties is still largely unknown. Consequently, all existing kinetic theories simply *postulated* forms for the single-particle and the two-particle distribution functions. The forms postulated for the single-particle distribution function include the usual Gaussian form (Maxwell-Boltzmann distribution), a generalized Gaussian (the exponential of a quadratic form in the velocity components), and a Gaussian with a polynomial multiplicative correction (moment expansion). The form for the two-particle distribution function typically involves a product of two single-particle distribution functions and a density-dependent correction factor. In severe contrast to these forms, the single-particle distribution function that we evaluated from simulations of shear flows is proportional to the exponential of a quadratic polynomial in the speed with strongly angle-dependent coefficients. This function is neither a Gaussian nor a generalized Gaussian. Our studies (presented in Chapter 5) also indicate that it depends in a non-trivial way on the various macrofields and their gradients.

In view of the rheological differences between granular and regular fluids, the use of a casual analogy between the two in deriving theories has to be viewed with some circumspection. Hence we will dispense with this analogy and focus on fundamental unbiased studies of granular fluids. The goals of our research may be stated as follows: (1) to inquire into the basic phenomenology of granular flows using an unbiased minimal-model approach as afforded by molecular dynamics simulations; (2) to accurately determine the fundamental quantities, such as the single-particle distribution function and multiple-particle statistical characteristics, lying at the foundation of any statistical theory of granular fluids; and (3) to lead, based on these phenomenological and statistical studies, towards a successful statistical theory of rapid granular flows in the dilute to moderately dense regimes. This thesis represents the first steps taken towards the achievement of these goals.

Chapter 2

Clustering Instability in a Free Granular Gas

In this chapter, we present detailed results of computer simulations of a monodisperse collection of inelastic rigid disks in a periodic square enclosure. The model for the collisions of the disks is given by (1.2), and no external force is applied to the system. The initial state is taken to have a Maxwell-Boltzmann distribution of the velocities and a uniform distribution of density. This is numerically achieved by performing a preliminary simulation in which the collisions are taken to be elastic for a sufficiently long time so that an equilibrium distribution is established. Then a coefficient of restitution which is smaller than unity is turned on. The simulations show that in the course of its energetic 'decay', the system undergoes a transition from its homogeneous initial state to a highly inhomogeneous state consisting of dense meandering clusters. For a given value of the coefficient of restitution, $\tilde{e}$, these clusters are separated by a typical scale $L_0 \approx l/\sqrt{1 - \tilde{e}^{\,2}}$, where l is the mean free path in the corresponding homogeneous system. Most of the fluctuating kinetic energy then resides in the relatively dilute regions which surround the clusters. A system whose linear dimension is less then L_0 does not give rise to clusters; nevertheless, it is inhomogeneous, the scale of the corresponding inhomogeneity being the longest wavelength allowed by the system's size. A theoretical model which explains the clustering phenomenon is derived, and various macroscopic and microscopic properties of freely decaying

systems are examined.

2.1   Global Characteristics of a Decaying Granular Gas

As the granular gas decays from its energetic and homogeneous initial state prepared as described above, a most striking phenomenon occurs which is the transition of the gas between two markedly different states, viz. an earlier one when the system is still homogeneous and a later one when it is dehomogenized by the onset of an instability. These two states are characterized by different though well-defined global properties such as the decay rate of the total energy and the flatness of the velocity distribution as well as different local properties. In this section we present some global features pertaining to two systems of 40000 particles each in a square enclosure. The first system is nearly elastic ($\tilde{e} = 0.98$) and the second is highly inelastic ($\tilde{e} = 0.6$). In both systems the area fraction of the particles is $\nu = 0.05$, and both systems are prepared in the same initial condition (with the same value of the initial granular temperature). We shall refer to the nearly elastic system as System **I** and to the other system as System **II**.

At a time corresponding to approximately 300 collisions per particle System **I** undergoes a transition, following which the statistically quiescent and homogeneous state (whose phase space information is shown in Fig. 2.1 is replaced by an inhomogeneous state composed essentially of layers moving in opposite directions as depicted in Fig. 2.2. The figure shows the coarsed-grained velocity field superposed on the particle configuration for the system at a time corresponding to 400 collisions per particle, i.e. at a time corresponding to approximately 100 collisions per particle after the point of transition. It shows evidence of a shearing motion while the particle configuration plot shows that the density is lower where the shear rate is higher and vice versa. The latter observation is in accord with the theoretical argument presented in Section 2.4. Following these considerations the granular temperature is expected to be higher where the rate of viscous heating (which is proportional to the square of the shear rate) is higher. Since the pressure increases as the granular temperature is raised, the

density must decrease due to the motion of particles from high pressure regions to low pressure regions. This dynamical picture is further corroborated by Figure 2.11 in which scatter-plots of various combinations of the coordinates and velocities of all the particles in the system are presented.

The inelastic System **II** undergoes a transition after about 10 collisions per particle following the initial state. This number much less than the corresponding number for System **I**. Following the transition, System **II** exhibits a meandering set of dense clusters of particles surrounded by a background of low density and relatively high granular temperature. Animated sequences of the dynamics reveal that the clusters are essentially coherent structures moving at well-defined velocities, sweeping and shedding trails of particles as they move. Their granular temperature is significantly lower than that of the surrounding regions. The coarse-grained velocity field for System **II** (shown superposed on the particle configuration plot) at a time corresponding to 100 collisions per particle is presented in Fig. 2.3. A corresponding temperature contour plot is presented in Fig. 2.4. Notice the prominence of the dense clusters.

The time evolution of several global properties will now be examined. Fig. 2.5(A) corresponding to System **I** depicts the accumulated number of collisions (from $t = 0$ up to a time t) per particle, c, versus $\ln(t)$. Following an initial transient, the average collision rate per particle, i.e. $\dot{c} = \partial c / \partial t$, is proportional to $1/t$ (as expected on the basis of the kinetic theory; cf. Section 2.4.2), with different proportionality constants before and after the transition. The decay of the average energy per particle (following the initial transient) is exponential in c and follows a power law in t (Figures 2.5(B) and 2.5(C)). The corresponding graphs for System **II** are shown in Figures 2.5(D), 2.5(E) and 2.5(F). It is shown in Section 2.4.2 that the local granular temperature T decays exponentially as a function of c. The slower decay rate of the energy following the transition is clearly due to the formation of 'cooler' regions of higher density which contain a large part of the total mass yet contribute only a small part to the global energy decay rate.

Since there is large-scale coherent motion in these systems, it is necessary to distinguish the hydrodynamic (or coarse-grained) velocity field from the local fluctu-
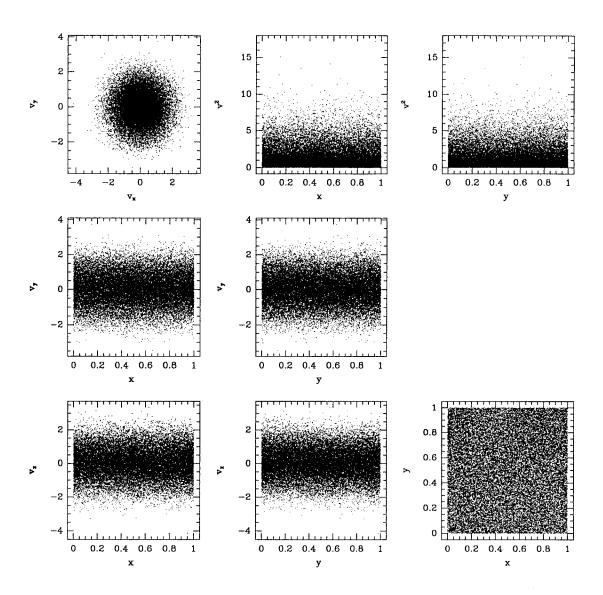
Figure 2.1: Scatter plots showing phase space information of System **I** following 50 collisions per particle. This corresponds to an early time, i.e. before the mass reorganization. Each point in the plots denotes the property of one particle.
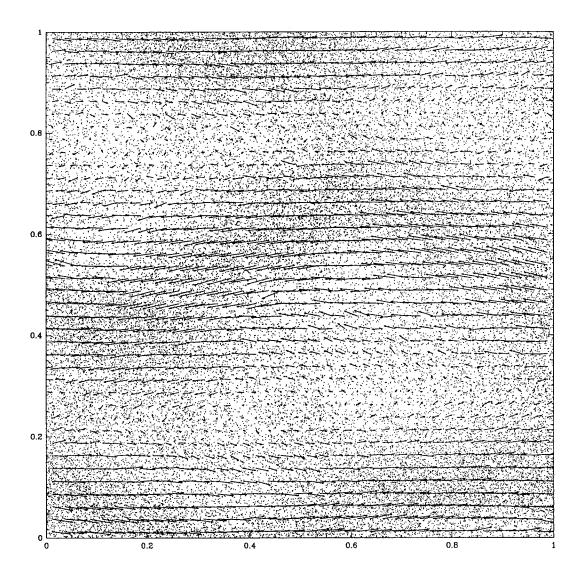
Figure 2.2: The particle configuration for System **I** following 400 collisions per particle on which a coarse-grained velocity field has been superposed. This figure depicts the system at a time corresponding to 100 collisions per particle after the transition, which occurred at approximately 300 collisions per particle.
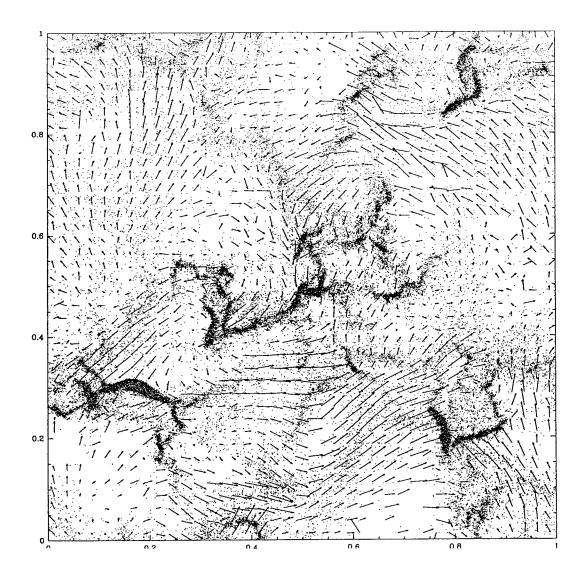
Figure 2.3: The particle configuration and a superimposed coarse-grained velocity field for System **II** following 100 collisions per particle. The box size is normalized to unity.
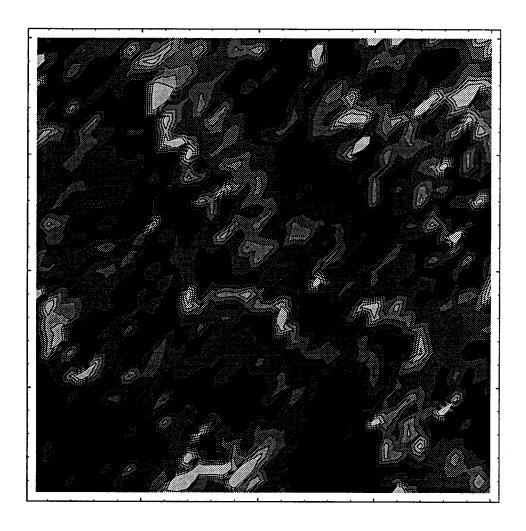
Figure 2.4: A shaded contour plot of the granular temperature field for System **II** following 100 collisions per particle. The shade code is: darker shades for low temperatures and lighter shades for high temperatures. It is clear from this plot and Fig. 2.15 that the clusters are much 'cooler' than their surroundings.
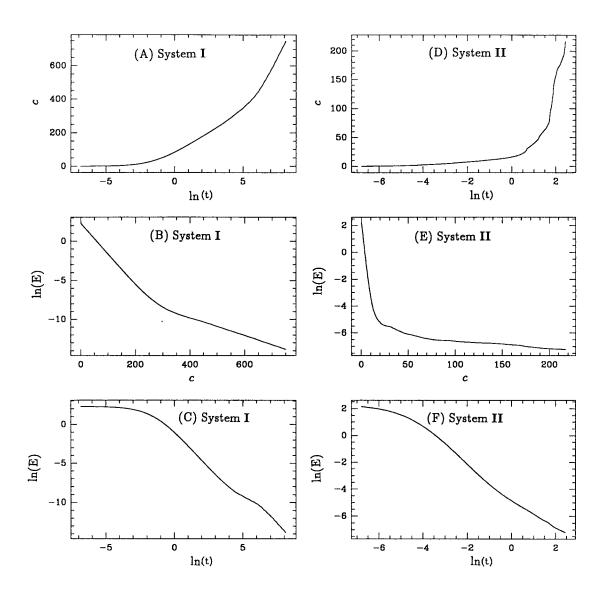
Figure 2.5: Global diagnostics: (A) accumulated number of collisions per particle, c, versus time, t, in System I (the graph is versus $\log(t)$); (B) the average kinetic energy per particle, E, versus the accumulated number of collisions per particle, c, in System I ; (C) the same quantity as in (B) versus time in System I. The diagnostics for System II are show in (D), (E), and (F) corresponding to (A), (B) and (C) respectively.
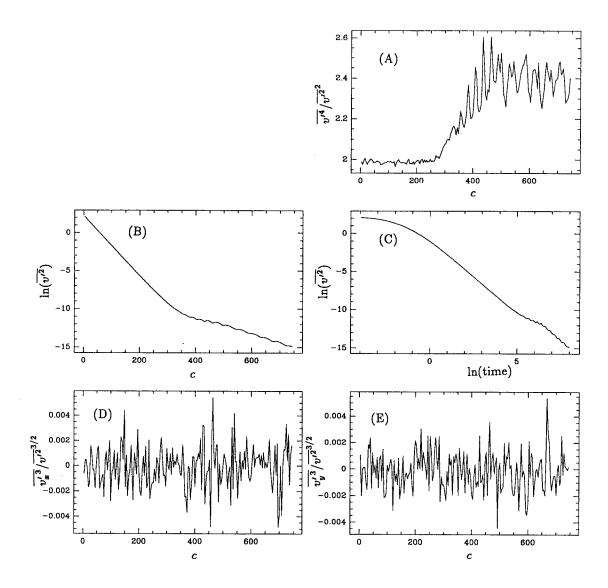
Figure 2.6: Further global diagnostics for System **I** : (A) the flatness of the fluctuating velocity distribution versus the accumulated number of collisions per particle, c. (B) the average fluctuation energy per particle versus c. (C) the same quantity as in (B) versus the true time. (D) and (E) show the time histories of two measures of the asymmetry in the fluctuating velocity distribution.

ating velocity. The average kinetic energy per particle, which is proportional to the mean square velocity, should be distinguished from the granular temperature, which is proportional to the mean square fluctuating velocity. The decay of the global average granular temperature, $\overline{T}$, which is defined following (1.7), for System **I** and System **II** is shown in Figures 2.6(C) and 2.7(C) respectively. While (following Figures 2.5(C) and 2.5(F)) the exponent in the power law in t for the average kinetic energy per particle as a function of t is smaller after the transition than before it, the exponent in the power law for $\overline{T}$ versus t remains the same. If there were no large-scale coherent motion in the system, the average kinetic energy per particle would be equivalent to the average granular temperature. However, coherent motion does occur in both Systems **I** and **II** after the transition (and to a smaller extent before the transition), and the slower decay of the kinetic energy may be attributed to the fact that more of the energy is now contained in the coherent part of the motion than before the transition.

Other global disgnostics shown in Figures 2.6 and 2.7 bear on the distribution of the fluctuating velocities in the system. The flatness (kurtosis) κ of the distribution shown in Figures 2.6 and 2.7 is defined in (1.8). Were the distribution of fluctuating velocities Gaussian one would have obtained $\kappa = 2$ (in two dimensions), as is indeed the flatness at $t = 0$ (the initial condition *is* Gaussian). The value of the flatness remains close to 2 until the transition, following which it appears to oscillate around a higher equilibrium value. It is therefore clear that a new distribution function, whose form is (at least approximately) fixed in time (in spite of the decaying granular temperature) characterizes the post-transition state. It is reasonable to assume that the distribution function (modified to correspond to a fixed temperature) is relevant to nondecaying systems such as sheared ones since spontaneous shear should not give rise to significantly different results than enforced shear.

Two measures of the asymmetry in the distribution are also provided. These are the global averages of the x- and y- components of the fluctuating velocity scaled by $\overline{v'^2}^{3/2}$.
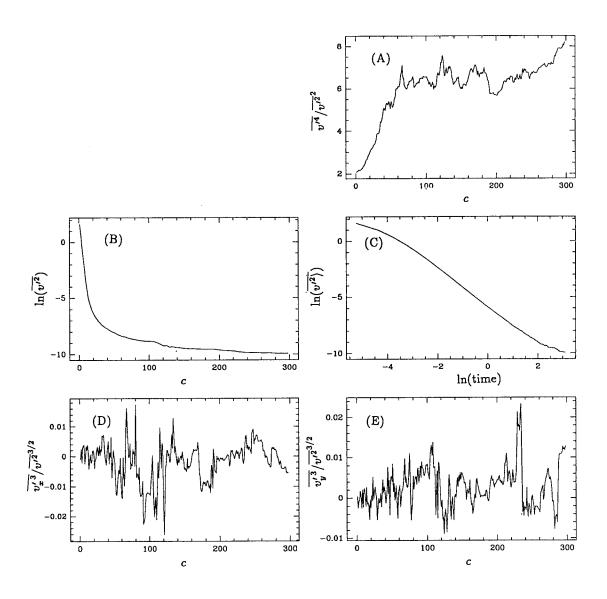
Figure 2.7: Further global diagnostics for System **II**. (A)-(E) correspond to (A)-(E) respectively in Fig. 2.6.

2.2 Spectral Analyses of the Macrofields

This section is devoted to the presentation of the Fourier spectra of the mass and momentum densities for both System **I** and System **II**. These spectra are extremely useful for the elucidation of the dominant scales that appear in systems with different values of $\tilde{e}$ (and of the other parameters), for the characterization of the microstructure that exists in inelastic systems as well as for an impartial judgement of cluster sizes. For the study of the instability mechanism, a series of spectra computed at successive times reveals the manner in which the dominant modes evolve and shows the interplay between the dynamics of the mass and momentum densities. An inspection of such a series indicates that while both the mass and momentum spectra (for the same system) show uniformly excited modes at $t = 0$, one or more low-wavenumber modes become dominant at $t > 0$ in the latter *before* the corresponding modes in the former become dominant. The dominant momentum modes, which correspond to shear fluctuations, arise earlier and they drive the motion of the mass, causing the subsequent growth of the mass modes. The above observation is in accord with the theoretical analysis presented in Section 2.4.2.

The mass and momentum densities can be represented as

$$\rho(\mathbf{x}) = \sum_{j=1}^{N} m\delta(\mathbf{x} - \mathbf{x}_j)$$

$$\mathbf{p}(\mathbf{x}) = \sum_{j=1}^{N} m\mathbf{v}_j\delta(\mathbf{x} - \mathbf{x}_j)$$

where $\mathbf{x}_j$ is the position vector of particle j in the system and $\delta(\mathbf{x} - \mathbf{x}_j)$ is the delta function. The corresponding Fourier transforms are:

$$\tilde{\rho}(k) \equiv \frac{1}{2\pi}m \sum_{j=1}^{N} \exp(i\mathbf{k} \cdot \mathbf{x}_j)$$

$$\tilde{\mathbf{p}}(k) \equiv \frac{1}{2\pi}m \sum_{j=1}^{N} \mathbf{v}_j \exp(i\mathbf{k} \cdot \mathbf{x}_j).$$

The wavevectors allowed by the periodic boundary conditions are $\mathbf{k} = (2p\pi/L_x, 2q\pi/L_y)$, where p and q are integers and L_x and L_y are the dimensions of the system. The figures in this section show the integrals of $|\tilde{\mathbf{p}}(\mathbf{k})|^2$ and $|\tilde{\rho}(\mathbf{k})|^2$ over a circle of radius

$|\mathbf{k}|$ in $\mathbf{k}$-space versus $k = |\mathbf{k}|$. In practice, these integrals are computed by summing the contributions from those allowed modes that lie in the annulus from k to $k + \Delta k$. Since the circumference of a circle whose radius is k is linear in k, one expects these integrals to be linear in k when equipartition holds.

Figures 2.8 and 2.9 show a series of the mass and momentum spectra for System **I** at different times corresponding to 50, 150, 400, and 550 collisions per particle. At 50 collisions per particle (corresponding to Figures 2.8(A) and 2.8(B)), the system is still homogeneous and equipartition exists. At 150 collisions per particle (corresponding to Figures 2.8(C) and 2.8(D)), a momentum mode at $k = 2\pi$ clearly becomes dominant but no mass mode has yet become dominant. By 400 collisions per particle (corresponding to Figures 2.9(A) and 2.9(B)), the momentum mode at $k = 2\pi$ has caused the growth of a corresponding mass mode at twice the wavenumber. This momentum mode reflects a shearing motion in the system, while the mass mode reflects the higher concentration of mass near the minima of the square of the shear rate. Since the mass will aggregate where the rate of viscous heating is minimum, the shear mode that drives the motion will always produce a mass mode at twice the wavenumber (the heating function is quadratic in the velocity field; cf. Section 2.4.2). These modes remain dominant up to the longest time checked by the simulation, i.e. 550 collisions per particle, showing that the system continues to remain in a sheared configuration. Experiments on nearly elastic systems whose aspect ratios are not equal to one (and which are not presented here in detail) show that the typical length scale for the (spontaneously) sheared configuration (i.e. the wavelength of the dominant shear mode), if it occurs, is always given by the longer dimension of the system. This fact is accounted for by the theory presented in Section 2.4.

The spectra for System **II** following 100 collisions per particle are shown in Fig. 2.10. This corresponds to a time that supercedes the transition. The existence of a multitude of scales, reflecting the increased complexity of the microscopic dynamics, in this case, is evident.
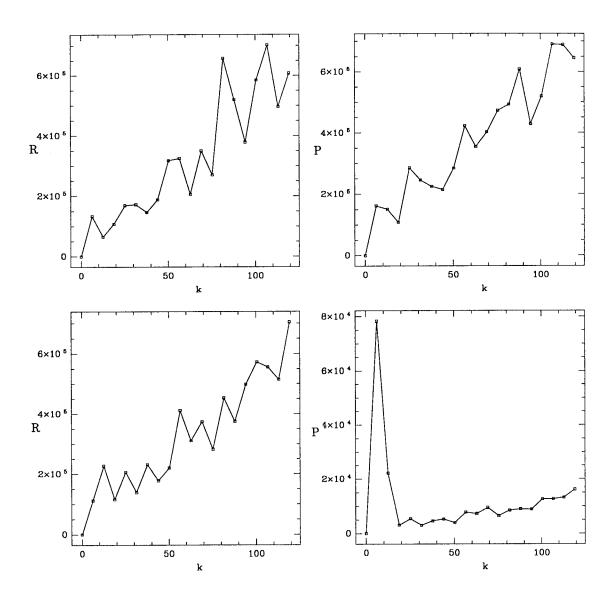
Figure 2.8: Spectra for System **I** : (A) and (B) show R and P, the integrals of $|\tilde{\rho}(\mathbf{k})|^2$ and $|\tilde{\mathbf{p}}(\mathbf{k})|^2$ over a circle in **k**-space (see text), versus k at a time corresponding to 50 collisions per particle. At this time the system is still homogeneous and equipartition is evident. (C) and (D) show the same quantities respectively following 150 collisions per particle. Notice here the appearance of a dominant mode in the momentum spectrum but not in the mass spectrum.
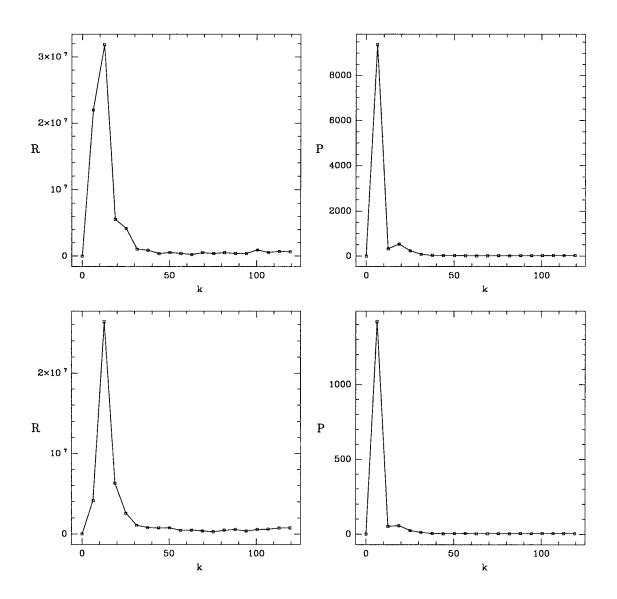
Figure 2.9: Spectra for System **I** : (A) and (B) show the mass and momentum spectra respectively at 400 collisions per particle. The dominant mode in the momentum spectrum has by now driven the growth of a mass mode at twice the wavenumber. (C) and (D) show the corresponding spectra at 550 collisions per particle. P and R are defined as in Fig. 2.8.
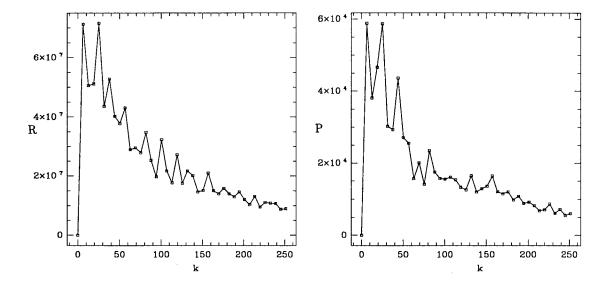
Figure 2.10: Spectra for System **II** : (A) and (B) show the mass and momentum spectra following 100 collisions per particle, corresponding to a post-transition state of the system. P and R are defined as in Fig. 2.8.

2.3 Microscopic Dynamics

The present section is concerned with some microscopic facets of the dynamics of granular systems as well as with various coarse-grained quantities such as the detailed density, velocity, temperature, and stress fields. The distributions of impact parameters for the collisions occurring in both systems are examined as well.

Scatter plots for System **I** , following 50 collisions per particle, which is an early stage before the organization of the mass were already presented in Figure 2.1. In Figure 2.11 we present similar plots for a time corresponding to 400 collisions per particle, which is after the shear layers have emerged. The particle configuration at the latter time is shown in Figure 2.2, on which the coarse-grained velocity field has been superposed. A corresponding mass density contour plot is shown in Figure 2.14. The organization of the mass into two shear layers is clearly noticeable. A shaded contour plot for the temperature field for System **I** following 400 collisions per particle is shown in Figure 2.12. A comparison of Figures 2.11, 2.14, and 2.12 reveals that regions of higher density have a lower granular temperature than regions of lower density.

Scatter plots corresponding to System **II** , beyond the transition at a time corresponding to 100 collisions per particle are presented in Figure 2.13. The coarse-grained velocity field superposed on the particle configuration for that system recorded at the same time is shown in Figure 2.3. A plot showing the contours of constant coarse-grained density for System **II** at 100 collisions per particle, which provides a notion of the cluster size, is provided in Fig. 2.14. The granular temperature field following the same number of collisions is shown in Fig. 2.4 as a shaded contour plot. Comparison of Fig. 2.4 and Fig. 2.14 shows that the highly prominent clusters have a much lower granular temperature than their surroundings.

The distribution of impact parameters (cf. Fig. 1.3) in System **I** following 400 collisions per particle is shown in Figure 2.16(A). This is obtained by recording the impact parameters for 40000 successive collisions occurring in the system (which amounts to recording for a time corresponding, on the average, to 1 collision per particle, i.e. to a 'short' time) and counting the number of values that lie in equal
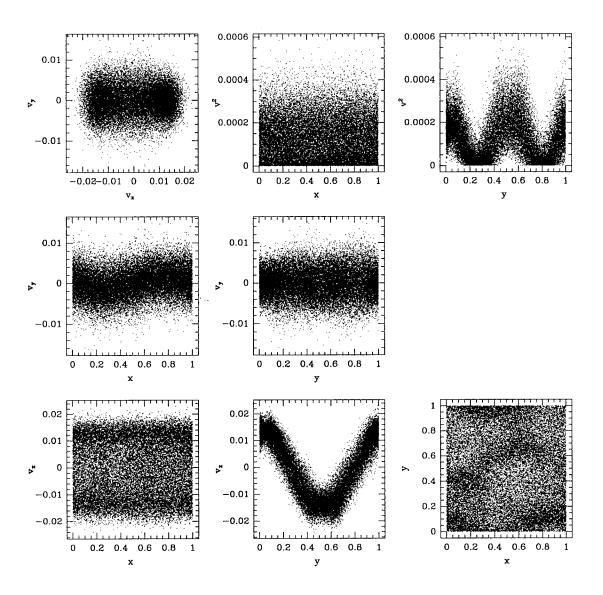
Figure 2.11: Scatter plots corresponding to System **I** following 400 collisions per particle. The organization of the mass into two shear layers is clearly noticeable.
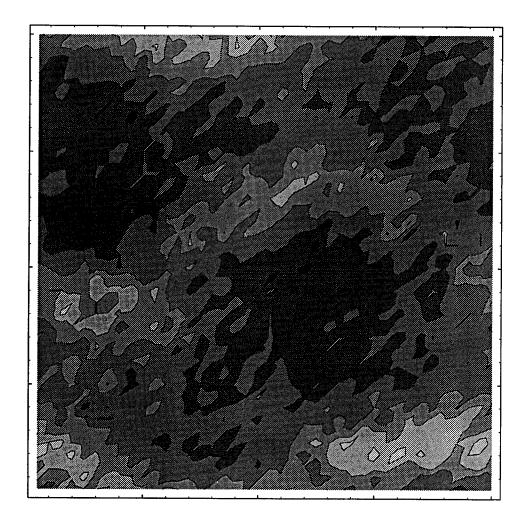
Figure 2.12: A shaded contour plot of the granular temperature field for System **I** following 400 collisions per particle. The shade code is: darker shades for low temperature regions and lighter shades for high temperature regions. Comparing this figure to Fig. 2.14, it is seen regions of lower density have higher granular temperature and vice versa.
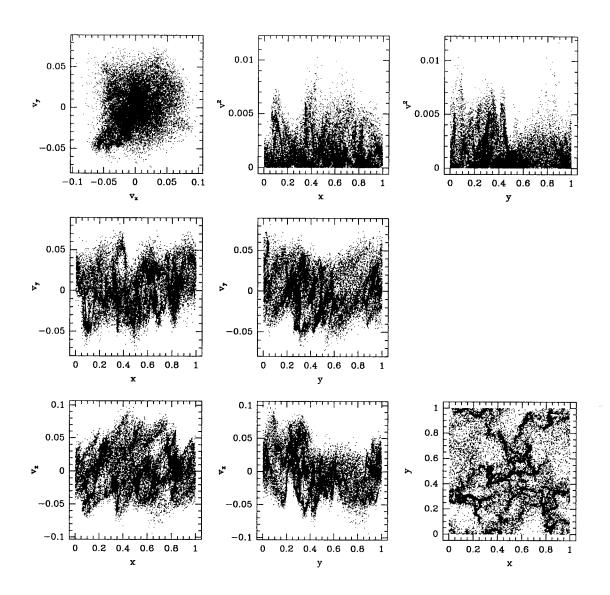
Figure 2.13: Scatter plots corresponding to System **II** following 100 collisions per particle.
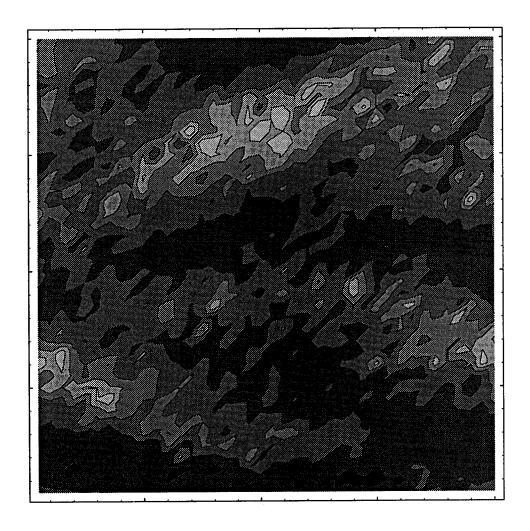
Figure 2.14: A shaded contour plot for the mass density for System **I** following 400 collisions per particle. The shade code is: darker shades for low density regions and lighter shades for high density regions.
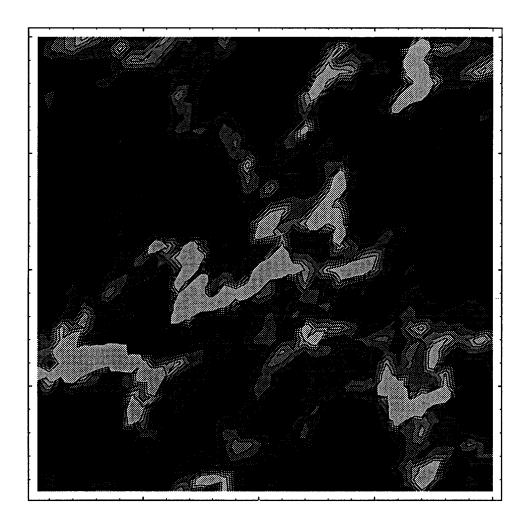
Figure 2.15: A shaded contour plot for the mass density for System **II** following 100 collisions per particle. The shade code is: darker shades for low density regions and lighter shades for high density regions.
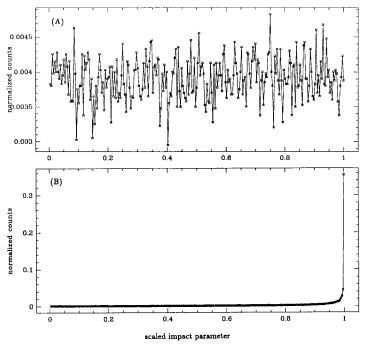
Figure 2.16: The distribution of impact parameters (A) in System **I** , following 400 collisions per particle, (B) in System **II** , following 100 collisions per particle. The horizontal axis represents the impact parameter scaled by the diameter of the disk.

intervals between 0 and σ, the diameter of the particle. The distribution expected for an elastic hard-disk gas in equilibrium is flat (up to noise) due to isotropy. The distribution for System **I** is essentially flat, implying that local equilibrium is maintained, to a large extent, in the system. The distribution for System **II** following 100 collisions per particle, obtained in the same way and shown in Figure 2.16(B), is sharply peaked at the maximally allowed value, σ, implying that the majority of collisions in the system are grazing collisions. This is clearly due to the coherent motion of the clusters whose constituent particles have approximately the same velocities.

Figure 2.17 shows a shaded contour plot of the trace, $\mathcal{P}$, of the total stress tensor τ defined in (1.7) for System **I** following 400 collisions per particle; while Figure 2.18 shows the same quantity for System **II** following 100 collisions per particle. When Figures 2.18 and 2.3 (both corresponding to System **II**) are examined together, it is seen that those regions with the largest values of $\mathcal{P}$ correspond to regions in which clusters are moving and sweeping into particles that lie in the surrounding dilute regions. In some cases, the cluster is seen even to be sweeping into particles moving in directions generally opposite to the direction of motion of the cluster itself. When

the kinetic and collisional contributions are compared, it is found that $\mathcal{P}$ in these regions is dominated by its collisional part, $\mathrm{Tr}(\tau^{(c)})$. This is clearly due to the large amount of momentum that is being exchanged in the collisions that occur during the influx of new particles into the cluster and during the outflux as the cluster sheds its particles behind it. The fact that the density of particles in the cluster is high implies an increased frequency of collisions, which also enhances the collisional contribution. Given that $\mathcal{P}$ is essentially the pressure, one may, from its definition (1.4), speak of a 'kinetic' and a 'collisional' pressure; and one finds that, owing to the dynamics of cluster motion, the clusters can be low temperature—and thus low 'kinetic' pressure—objects, and yet at the same time be high 'collisional' pressure objects.

2.4   The Clustering Mechanism

2.4.1   Qualitative Description of the Mechanism

The only difference between a regular gas and a 'granular' one, on the microscopic level, is the fact that in the latter case the collision process is inelastic. It is thus clear that the fact that the homogeneous state of a granular gas is unstable should be attributed to the inelastic nature of the collisions. In the present section, we propose a mechanism which, we believe, underlies the instability of the homogeneous granular state.

Consider a homogeneous granular gas composed of identical particles which is not subject to any external forces. Assume that the macroscopic velocity field vanishes and that the microscopic velocity is isotropic. Naive intuition may suggest that such a system will stay in a homogeneous state of vanishing macroscopic velocity. The energy, or granular temperature, of the system will decay due to the inelasticity of the collisions and the only qualitative change expected with time is a possible nontrivial evolution of the velocity probability distribution function (shrinking to a δ-function as time goes to infinity). If this picture were correct, the dynamics of a granular gas would be highly uninteresting. However, as in any gas, one expects statistical fluctuations of practically every physical quantity. In particular, since
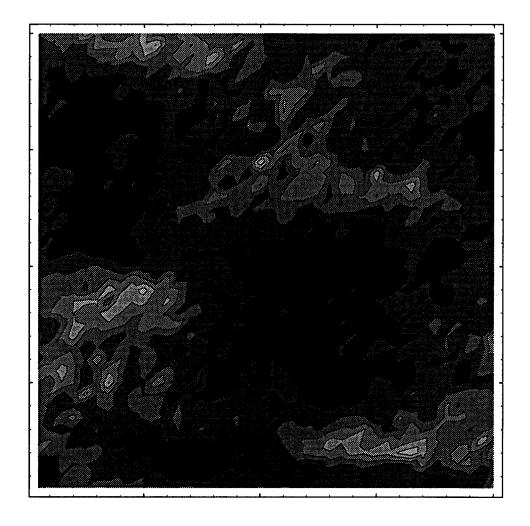
Figure 2.17: A shaded contour plot of $\mathcal{P} = \text{Tr}(\tau)$, where τ is the stress tensor, for System **I** following 400 collisions per particle. The shade code is: darker shades for regions of low $\mathcal{P}$ and lighter shades for those of high $\mathcal{P}$.
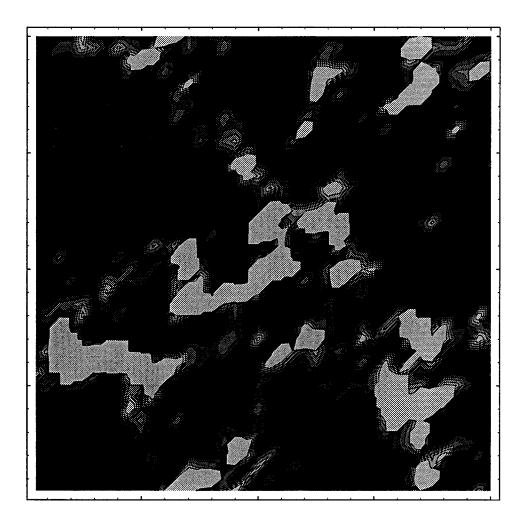
Figure 2.18: A shaded contour plot of $\mathcal{P} = \mathrm{Tr}(\tau)$, where τ is the stress tensor, for System **II** following 100 collisions per particle. The shade code is: darker shades for regions of low $\mathcal{P}$ and lighter shades for those of high $\mathcal{P}$.

mass and momentum are conserved, the (mass) density and momentum density fields are hydrodynamic variables. As a result, one expects long wavelength fluctuations of these quantities to be 'slow'; in particular, they can be slow with respect to the rate of energy decay since the latter proceeds at a pace which depends primarily on the local density and the local energy density (which determines the rate of collisions) whereas the former can be as slow as wished, provided the wavelength is long enough. Thus, once a hydrodynamic fluctuation of a sufficiently large characteristic length is created, it will eventually dominate the dynamics of the system, and the relatively fast variable, the temperature, will have to be enslaved to its dynamics. In particular, when one considers a shear mode, regions in which the shear rate is relatively high will have a higher temperature than other regions due to viscous heating. As a consequence, the pressure in such regions will be relatively high as well. This elevated pressure will drive particles out of high shear regions into lower shear regions, thus increasing the density in the low shear regions. The frequency of collisions in the lower shear, higher density regions will be larger than in the low density regions (the rate of collision is proportional to the square of the density) and since the collisions are inelastic, the particles in the dense regions will lose their kinetic energy at a faster rate than those in the low density regions, i.e. the granular temperature will decay faster in high density regions. This will lead to a further decrease in pressure in the high density regions (whose pressure was relatively low even before the mass migration) hence to an increased pressure gradient driving more particles into the high density region. Clearly this process is self-perpetuating, ending in a cluster at the location of the low shear region. The final size of the cluster is determined by the flux of particles out of the cluster due to collisions with ('hot') particles in the dilute regions. The cluster creation process can occur only if the rate of cooling in high density regions is fast enough to prevent the establishment of a high pressure and if diffusion effects, which tend to oppose such an agglomeration are slower than the clustering process. It turns out that these conditions imply a certain length scale of intercluster distances. This length scale is basically the linear dimension of a region most of whose mass collapses into a single cluster, i.e. the region that contained a single temperature minimum which the shear mode establishes before the mass migration started.

In describing the above proposed mechanism, we have concentrated chiefly on a shear fluctuation in an unforced system. Clearly, the self-perpertuating mechanism leading to the creation of a cluster can start with a density or temperature fluctuation as well. A higher density in a given region will lead to a relatively rapid cooling of that region and to an eventual collapse. A similar argument clearly applies to the case of a temperature fluctuation. In the case of a permanently forced system, the granular temperature does not decay to an asymptotic zero value, but local temperature fluctuations are depressed by the inelastic nature of the collisions on a relatively rapid time scale, which depends on local properties, whereas hydrodynamic fluctuations may be long lived and thus the same mechanism described above is also relevant to forced systems, as we shall see in Chapters 3 and 4.

2.4.2 Linear Stability Analysis of the Jenkins-Richman Equations

The ideas proposed in the previous subsection can be easily demonstrated using a kinetic theoretic model. This is done in the present subsection for the three-dimensional case. An example of model equations which are based on kinetic theory, and which have enjoyed a considerable degree of success is the set of equations derived by Jenkins and Richman[47]. These equations read:

$$\frac{3}{2}\rho\frac{\mathrm{D}T}{\mathrm{D}t} = \sigma\rho_s\nabla\cdot(T^{\frac{1}{2}}c\nabla T) - a\rho T\mathrm{div}\mathbf{v} + b\sigma\rho_s T^{\frac{1}{2}}\mathrm{Tr}\hat{D}_{ij}^2 - \frac{d\rho_s}{\sigma}T^{\frac{3}{2}} \qquad (2.1)$$

$$\rho\frac{\mathrm{D}\mathbf{v}}{\mathrm{D}t} = -\nabla(a\rho T) + b\sigma\rho_s T^{\frac{1}{2}}(\frac{1}{2}\mathbf{\Delta}\mathbf{v} + \frac{1}{6}\nabla\mathrm{div}\mathbf{v})$$

$$+ \frac{1}{2}\nabla(b\sigma\rho_s T^{\frac{1}{2}})\cdot\nabla\mathbf{v} + \frac{1}{2}\partial_j(b\sigma\rho_s T^{\frac{1}{2}})\nabla v_j$$

$$- \frac{1}{3}\mathrm{div}\mathbf{v}\nabla(b\sigma\rho_s T^{\frac{1}{2}}) \qquad (2.2)$$

$$\dot{\rho} = -\mathrm{div}(\rho\mathbf{v}) \qquad (2.3)$$

where T is the granular temperature field, ρ is the density, $\mathbf{v}$ the velocity field, ρ_s the mass density of a solid particle, σ the diameter of a solid particle (it is assumed in the derivation of these equations that grains are spherical and identical), $\frac{\mathrm{D}}{\mathrm{D}t}$ is the material derivative and a, b, c and d are functions of the solid volume fraction, ν.

The low density values of a, b, c and d are given by:

$$a = 1 \tag{2.4}$$

$$b = \frac{5\sqrt{\pi}}{48} \tag{2.5}$$

$$c = \frac{25\sqrt{\pi}}{128} \tag{2.6}$$

$$d = \frac{24}{\sqrt{\pi}}\epsilon\nu^2 \tag{2.7}$$

where $\epsilon = 1 - \tilde{e}^{\,2}$, $\tilde{e}$ being the coefficient of normal restitution. (The definition presented in [47] is $\epsilon = 1 - \tilde{e}$; since energy dissipation is proportional to $(1 - \tilde{e}^{\,2})$, we prefer the present definition). The tensor $\hat{D}_{ij}$ is the deviatoric part of the symmetrized velocity gradient tensor and $\mathrm{Tr}\hat{D}_{ij}^2$ is the viscous heating function:

$$\mathrm{Tr}\hat{D}_{ij}^2 = \frac{1}{2}(\partial_i v_j)^2 + \frac{1}{2}(\partial_j v_i)^2 - \frac{1}{3}(\mathrm{div}\mathbf{v})^2 \tag{2.8}$$

where $\partial_i = \frac{\partial}{\partial x_i}$ and the Einstein summation convention is assumed.

We consider only the dilute limit, $\nu \rightarrow 0$, of the Jenkins-Richman equations. The similarity of these equations to the Navier-Stokes equations of hydrodynamics is evident. The major difference is the term $-\frac{d\rho_s}{\sigma}T^{3/2}$ in the temperature equation, which accounts for the energy losses due to inelastic collisions. This term can be easily understood in terms of a simple kinetic model.

The homogeneous solution of equations (2.1-2.3) is $\mathbf{v} = 0$ and $\rho = \rho_0$ (i.e. the initial uniform density). The temperature satisfies, in this case, the equation:

$$\frac{3}{2}\rho_0\dot{T}_0 = -\frac{d\rho_s}{\sigma}T_0^{3/2} \tag{2.9}$$

where T_0 denotes the homogeneous temperature. The solution of equation (2.9) is:

$$T(t) = \frac{T_0(0)}{(1 + \frac{t}{t_0})^2} \tag{2.10}$$

where:

$$t_0 = \frac{3\rho_0\sigma}{d\rho_s T_0^{1/2}(0)} \tag{2.11}$$

i.e. it decays as $1/t^2$ for $t \gg t_0$. Using equation (2.7) and the fact that $\rho = \rho_s\nu$, one obtains from equation (2.11):

$$t_0 = \frac{\sqrt{\pi}}{8}\frac{\sigma}{\nu}\frac{1}{\epsilon T_0^{1/2}(0)} \tag{2.12}$$

Next define an effective mean free path:

$$l_0 = \frac{\sqrt{\pi}}{8} \frac{\sigma}{\nu} \tag{2.13}$$

Following equations (2.12) and (2.13):

$$t_0 = \frac{l_0}{\epsilon T_0^{1/2}(0)} \tag{2.14}$$

Note that if one defines the mean free path $l = 1/\sigma_T n$, where $\sigma_T = \pi\sigma^2$ (in three dimensions) and n is the number density, then

$$l_0 = \frac{3}{4}\sqrt{\pi}l \tag{2.15}$$

The linearization of the Jenkins-Richman equations around T_0, ρ_0 yields (following a subsitution of the dilute limit values of a, b, c and d (cf. equations (2.4)-(2.7)))

$$\rho_0\dot{\mathbf{v}} = -\rho_0\nabla\delta T - T_0\nabla\delta\rho + \frac{5\sqrt{\pi}}{48}\sigma\rho_s T_0^{1/2}(\frac{1}{2}\boldsymbol{\Delta}\mathbf{v} + \frac{1}{6}\nabla\mathrm{div}\mathbf{v}) \tag{2.16}$$

$$\frac{3}{2}\rho_0\dot{\delta T} = \frac{25\sqrt{\pi}}{128}\sigma\rho_s T_0^{1/2}\boldsymbol{\Delta}\delta T - \rho_0 T_0\mathrm{div}g\mathbf{v}$$

$$- \frac{36}{\sqrt{\pi}}\frac{\epsilon\nu^2\rho_s}{\sigma}T_0^{1/2}\delta T - \frac{48}{\sqrt{\pi}}\frac{\epsilon\nu}{\sigma}T_0^{3/2}\delta\rho - \frac{3}{2}\delta\rho\dot{T_0} \tag{2.17}$$

$$\dot{\delta\rho} = -\rho_0\mathrm{div}\mathbf{v} \tag{2.18}$$

where $\delta\rho$ and δT are the density and temperature perturbations respectively.

It is convenient to perform the following transformations. Define:

$$s \equiv \frac{1}{\epsilon}\ln(1 + \frac{t}{t_0}) \tag{2.19}$$

$$q \equiv \frac{T_0(t)}{\rho_0 T_0(0)}\delta\rho \tag{2.20}$$

$$\mathbf{u} \equiv \frac{\sqrt{T_0(t)}}{T_0(0)}\mathbf{v} \tag{2.21}$$

$$h \equiv \frac{\delta T}{T_0(0)} \tag{2.22}$$

Notice that s, q, $\mathbf{u}$ and h are dimensionless. Let $\mathbf{r'} \equiv \mathbf{r}/l_0$ be dimensionless coordinate vectors. Upon substitution of the variables defined in equations (2.19)-(2.22) and

rescaling the lengths by l_0, one obtains from equations (2.16)-(2.18):

$$\mathbf{u}_s = -\epsilon \mathbf{u} - \nabla h - \nabla q + \frac{5}{6}(\frac{1}{2}\Delta \mathbf{u} + \frac{1}{6}\nabla \text{div} \mathbf{u}) \tag{2.23}$$

$$h_s = \frac{25}{24}\Delta h - \frac{2}{3}\text{div}\mathbf{u} - 3\epsilon h - 2\epsilon q \tag{2.24}$$

$$q_s = -2\epsilon q - \text{div}\mathbf{u} \tag{2.25}$$

In equations (2.23)-(2.25), ∇ means $\frac{\partial}{\partial \mathbf{r}'}$, i.e. $l_0\frac{\partial}{\partial \mathbf{r}}$. Notice that unlike equations (2.16)-(2.18), which have time-dependent (through $T_0(t)$) coefficients, equations (2.23)-(2.25) have constant coefficients. Let $\Omega = \nabla \times \mathbf{v}$. Following equation (2.23)

$$\frac{\partial \Omega}{\partial s} = -\epsilon \Omega + \frac{5}{12}\Delta \Omega \tag{2.26}$$

and defining $\xi \equiv \text{div}\mathbf{v}$, it follows from equation (2.23) that:

$$\xi_s = -\epsilon \xi - \Delta h - \Delta q + \frac{5}{9}\Delta \xi \tag{2.27}$$

Assuming an eigenmode of the form $\exp(i\mathbf{K}\cdot\mathbf{r}')$, and an eigenvalue λ, one thus obtains from equations (2.24)-(2.25) and (2.27):

$$\lambda \begin{pmatrix} \xi \\ q \\ h \end{pmatrix} = \begin{pmatrix} -\epsilon - \frac{5}{9}K^2 & K^2 & K^2 \\ -1 & -2\epsilon & 0 \\ -\frac{2}{3} & -2\epsilon & -\frac{25}{24}K^2 - 3\epsilon \end{pmatrix} \begin{pmatrix} \xi \\ q \\ h \end{pmatrix} \tag{2.28}$$

The corresponding characteristic polynomial is:

$$(\lambda + \epsilon + \frac{5}{9}K^2)(\lambda + 2\epsilon)(\lambda + 3\epsilon + \frac{24}{25}K^2) + \frac{5}{3}K^2(\lambda + \frac{7}{5}\epsilon + \frac{5}{8}K^2) = 0 \tag{2.29}$$

It is straightforward to find from equation (2.29) that the spectrum corresponding to equation (2.29) is given by:

$$\lambda_1 = -\epsilon - \frac{1}{3}\frac{K^2}{\epsilon} + \mathcal{O}(K^2) \tag{2.30}$$

$$\lambda_2 = -2\epsilon - \frac{1}{3}\frac{K^2}{\epsilon} + \mathcal{O}(K^2) \tag{2.31}$$

$$\lambda_3 = -3\epsilon + \frac{4}{3}\frac{K^2}{\epsilon} + \mathcal{O}(K^2) \tag{2.32}$$

for $K^2 \ll \epsilon^2$ and:

$$\lambda_1 = -\frac{7}{5}\epsilon - \frac{5}{8}K^2 + \mathcal{O}(K^4) \tag{2.33}$$

$$\lambda_{2,3} = \pm i\sqrt{\frac{5}{3}}K - \frac{35}{72}K^2 - \frac{23}{10}\epsilon + \mathcal{O}(K^4) \tag{2.34}$$

for $K^2 \gg \epsilon^2$. When $K^2 \approx \mathcal{O}(\epsilon^2)$ there is a transitional behavior, which we shall not elaborate upon. Notice that for $K^2 \gg \epsilon^2$ one observes, as in the case of Navier-Stokes, two sound modes ($\lambda_{2,3}$) and a heat mode. On the linear level, the shear mode equation is decoupled from the other equations. Following equation (2.26), the eigenvalue corresponding to the shear mode is:

$$\lambda_\Omega = -\epsilon - \frac{5}{12}K^2 \tag{2.35}$$

for all values of K.

Following equation (2.10) and definition (2.19) the temperature in the homogeneous case decays as follows: $T(s) = T(s = 0)\exp(-2\epsilon s)$, i.e. it decays faster than the shear mode for $K^2 < \frac{12}{5}\epsilon$, faster than the heat mode (i.e. $2\epsilon > \lambda_1$) for $K^2 \leq \mathcal{O}(\epsilon)$. Thus, in conformity with the physical picture presented in Section 2.4.1, the fluctuations become dominant in time; in particular, the shear mode and the heat mode decay slower than the temperature does for large enough wavelengths. Since modes whose wavenumbers are far less than ϵ^2 will be shown below to be irrelevant to the clustering process, we shall consider only the case $K^2 \gg \epsilon^2$. At this point notice that we implicitly assume that $\epsilon \ll 1$. Indeed the Jenkins-Richman equations seem to be valid in the limit of almost elastic collisions; when $\epsilon \sim \mathcal{O}(1)$ these equations may have to be modified.

Transforming back from the s-variable to the time variable (using equation (2.19)) and noting that the wavenumber K in the rescaled space translates to kl_0 in the physical space, one obtains (using equations (2.20)-(2.22)) the following results for the various fields (the leading eigenvalue, λ_1, is used for all modes except for the decoupled shear mode):

$$\frac{\delta\rho(t)}{\delta\rho(0)} \sim \begin{cases} (1 + \frac{t}{t_0})^{1 - \frac{1}{3}\frac{k^2 l_0^2}{\epsilon^2}} & k^2 l^2 \ll \epsilon^2 \\ (1 + \frac{t}{t_0})^{\frac{3}{5} - \frac{5}{8}\frac{k^2 l_0^2}{\epsilon}} & k^2 l^2 \gg \epsilon^2 \end{cases} \tag{2.36}$$

$$\text{div}\mathbf{v}(t) \simeq \text{div}\mathbf{v}(0) \cdot \begin{cases} (1 + \frac{t}{t_0})^{-\frac{1}{3}\frac{k^2 l_0^2}{\epsilon^2}} & k^2 l^2 \ll \epsilon^2 \\ (1 + \frac{t}{t_0})^{-\frac{2}{5} - \frac{5}{8}\frac{k^2 l_0^2}{\epsilon}} & k^2 l^2 \gg \epsilon^2 \end{cases} \qquad (2.37)$$

$$\delta T(t) \simeq \delta T(0) \cdot \begin{cases} (1 + \frac{t}{t_0})^{-1-\frac{1}{3}\frac{k^2 l_0^2}{\epsilon^2}} & k^2 l^2 \ll \epsilon^2 \\ (1 + \frac{t}{t_0})^{-\frac{7}{5} - \frac{5}{8}\frac{k^2 l_0^2}{\epsilon^2}} & k^2 l^2 \gg \epsilon^2 \end{cases} \qquad (2.38)$$

$$\text{curl}\mathbf{v} = \text{curl}\mathbf{v}(0) \cdot (1 + \frac{t}{t_0})^{-\frac{5}{12}\frac{k^2 l_0^2}{\epsilon}} \qquad (2.39)$$

The approximate equality in equations (2.36)-(2.38) represents the fact that the density (or div$\mathbf{v}$ or δT) is a mixture of eigenmodes, which we assume to be dominated by the fastest growing eigenmode. In equations (2.36)-(2.39) it is assumed that all wavenumbers are hydrodynamic, i.e. $k l_0 \ll 1$; else the decay rate is much faster than in the hydrodynamic domain. It is worthwhile noticing (cf. equation (2.36)) that density perturbations are unstable, i.e. they actually grow. Thus, linear stability analysis reveals that the homogeneous state is unstable to density fluctuations. Moreover, the other (decaying) modes have a slower rate of decay than the homogeneous temperature does for $k l_0 < \mathcal{O}(\sqrt{\epsilon})$, hence they too can be considered to be unstable, since they may dominate in the long time limit. It is easy to check that as $\epsilon \to 0$, all modes whose wavenumbers are nonzero decay in the way predicted by the Navier-Stokes equation.

2.4.3 Nonlinear Analysis

The present section does not present a full nonlinear stability analysis of the Jenkins-Richman equations. Instead, we shall use these equations to argue that they imply clustering and that the typical scale characterizing intercluster distances is $\mathcal{O}(\frac{l}{\sqrt{\epsilon}})$, l being the mean free path. Curiously, the dominating mode in the nonlinear analysis is not the fastest growing linear mode, i.e. the density fluctuation. This is so because the nonlinear instability sets in much before the linear modes have a chance to significantly change in amplitude. Consider the (nonlinear) temperature equation (2.1). Assume the existence of an initial incompressible (div$\mathbf{v}$ = 0) fluctuation (this assumption is made for the sake of technical simplicity, the analysis below is easily generalized to include compressible fluctuations) characterized by a long enough spatial scale,

k^{-1}, such as to render the heat diffusion term as well as the heat convection term negligible (an approximation to be tested *a posteriori*). In this case, equation (2.1) can be approximated by:

$$\frac{3}{2}\rho\dot{T} = b\sigma\rho_s T^{\frac{1}{2}}\mathrm{Tr}\hat{D}_{ij}^2 - \frac{d\rho_s}{\sigma}T^{\frac{3}{2}} \tag{2.40}$$

Assuming further that the density can be considered to be fixed in equation (2.40), one obtains (using equations (2.4)-(2.7) and (2.13)):

$$\dot{T} = \frac{5}{9}l_0\mathrm{Tr}\hat{D}_{ij}^2 T^{\frac{1}{2}} - \frac{2\epsilon}{l_0}T^{\frac{3}{2}} \tag{2.41}$$

Define $Q \equiv T^{\frac{1}{2}}$. It then follows from equation (2.41) that

$$\dot{Q} = \frac{5}{18}l_0\mathrm{Tr}\hat{D}_{ij}^2 - \frac{\epsilon}{l_0}Q^2 \tag{2.42}$$

Next, let $Q = \frac{l_0}{\epsilon}\frac{\dot{H}}{H}$. Then H satisfies the equation:

$$\ddot{H} = \frac{5}{18}\epsilon\mathrm{Tr}\hat{D}_{ij}^2 H \tag{2.43}$$

Assuming at this point that $\mathrm{Tr}\hat{D}_{ij}^2$ is constant, one easily obtains the solution of equation (2.43), and hence of equation (2.41) to be:

$$T(t) = \frac{5l_0^2\mathrm{Tr}\hat{D}_{ij}^2}{18\epsilon}\left(\frac{1 - A\exp(-t\sqrt{\frac{10}{9}\epsilon\mathrm{Tr}\hat{D}_{ij}^2})}{1 + A\exp(-t\sqrt{\frac{10}{9}\epsilon\mathrm{Tr}\hat{D}_{ij}^2})}\right)^2 \tag{2.44}$$

where A depends on the initial value $T(0)$ in an obvious way. Under the assumption specified in the above, the temperature changes from its initial value to the value dictated by the viscous heating function $\mathrm{Tr}\hat{D}_{ij}^2$ on a time scale, t_1, given by

$$t_1 = \left(\frac{10}{9}\epsilon\mathrm{Tr}\hat{D}_{ij}^2\right)^{-\frac{1}{2}} \tag{2.45}$$

Thus the idea that the temperature is enslaved to the slow, hydrodynamic, modes is established once the validity of the assumptions leading to equation (2.44) is verified. To this end, and noting that $\mathrm{Tr}\hat{D}_{ij}^2$ is composed of squares of the derivatives of the velocity, define: $\mathrm{Tr}\hat{D}_{ij}^2 = k^2u^2$, where k^{-1} is a typical scale of the fluctuation. The variable u is a typical amplitude of the velocity. Since $\mathrm{div}v = 0$ by assumption, the

velocity field is a shear fluctuation. Following the linear stability analysis, it decays as $(1 + \frac{t}{t_0})^{-\frac{5}{12} \frac{k^2 l_0^2}{\epsilon}}$ (cf. equation (2.39). It is easy to check that the condition that the amplitude of the shear mode hardly changes on the time scale of t_1 is: $k l_0 < \frac{u}{\sqrt{T(0)}} \sqrt{\epsilon}$ where $t = 0$ is taken to be the initial time for the nonlinear stage. This condition is easily met since the temperature field decays faster than the velocity field on the linear level and $\epsilon \ll 1$ by assumption. The condition that the amplitude of the shear mode hardly changes even as the final stages of saturation of the temperature are approached, i.e. in the linear equation for the shear, $\rho \frac{\partial}{\partial t} \text{curl} \mathbf{v} = \frac{b}{2} \sigma \rho_s T^{\frac{1}{2}} \Delta \text{curl} \mathbf{v}$, one may replace T by its saturation value, is that the typical decay time for the decay of the shear mode exceeds $(\frac{10}{9} k^2 u^2 \epsilon)^{-\frac{1}{2}}$. This condition implies:

$$k^2 l_0^2 < \frac{48}{5\sqrt{2}} \epsilon \qquad (2.46)$$

or, using equation (2.15):

$$k^2 l^2 < \frac{256}{15\sqrt{2\pi}} \epsilon \qquad (2.47)$$

Since the r.h.s. of equation (2.47) is larger than ϵ, the condition $k^2 l^2 < \epsilon$ is sufficient. The neglect of the heat conduction term in deriving equation (2.40), with respect to, say, $\frac{dp_s}{\sigma} T^{3/2}$, is justified provided: $k^2 l_0^2 < \epsilon \frac{48}{25}$. Assuming that the velocity in the convective term $\mathbf{v} \cdot \nabla T$ is $\mathcal{O}(u)$, one finds that the neglect of the convective term (with respect to the $\frac{dp_s}{\sigma} T^{3/2}$ term) is justified provided $k l_0 < \frac{2\sqrt{T(0)}}{u} \epsilon$, a condition that was explained in the above. Finally, it follows from equation (2.36) that the density can be considered fixed for a time t_1 if either $k l_0 > \frac{T(0)^{1/2}}{u} \sqrt{\epsilon}$, or, $k l_0 > \sqrt{\frac{24}{25}} \sqrt{\epsilon}$. This first of these two conditions is easily met, as explained in the above. Actually, the second condition is met as well for the mode responsible for clustering because we show below that this mode satisfies $k l \sim \sqrt{\epsilon}$. The result so far is that the temperature rapidly saturates to a value dictated by the velocity field and thus a temperature gradient in the system is formed. Since the pressure, p_h, in the dilute limit is given by $p_h = \rho T$, one finds:

$$p_h = \frac{5}{18} \frac{\rho l_0^2 h}{\epsilon} \qquad (2.48)$$

Substituting the value of l_0 from equation (2.14) and using $\rho = \rho_s \nu$, one obtains:

$$p_h = \frac{5\pi \sigma^2 \rho_s}{18 \cdot 64} \frac{\text{Tr} \hat{D}_{ij}^2}{\epsilon \rho} \qquad (2.49)$$

i.e. the pressure established is inversely proportional to the density. This result is clearly in conformity with our qualitative analysis which argues that the larger the density, the lower the pressure.

The pressure gradient induced by the mechanism considered above induces a migration of particles into the low temperature regions. We shall not present here a full analysis of this motion. Instead we shall find the appropriate time scale as follows. Consider the part of the equation for the momentum density, $\mathbf{P}$, which contains the pressure induced forces alone

$$\dot{\mathbf{P}} = -\nabla p_h \tag{2.50}$$

in conjunction with the equation of continuity: $\dot{\rho} = -\mathrm{div}\mathbf{P}$. It follows that:

$$\ddot{\rho} = \Delta p_h \tag{2.51}$$

Clearly the time scale characterizing equation (2.51), when the typical length scale is k^{-1} is: $t_2 = \frac{1}{k}\sqrt{\frac{\rho}{p_h}}$. Substituting equation (2.48) into the formula for t_2 one obtains:

$$t_2 = \sqrt{\frac{18}{5}}\frac{\sqrt{\epsilon}}{kl_0\sqrt{h}} \tag{2.52}$$

Thus t_2 is shorter the larger k (it takes less time for the mass to move a distance $\frac{2\pi}{k}$, the shorter the distance). Thus the fastest and dominant cluster formation mechanism occurs at the largest allowed value of k. Since following (2.47): $kl \leq \sqrt{\epsilon}$, it follows that the process of clustering occurs on a scale determined by $kl \sim \sqrt{\epsilon}$.

When $kl > \sqrt{\epsilon}$ the clustering mechanism is not possible. On the other hand the linear modes still decay slower than the homogeneous temperature field. Consequently when $kl > \sqrt{\epsilon}$ one expects the system to be in a non-uniform state. The slowest decaying hydrodynamic modes, i.e. those with the lowest possible values of k allowed by the geometry of the system, will then dominate in the long run. These results are borne out by the simulations presented in this work.

2.5 Summary

The inelastic nature of the collisions occurring in a granular gas renders its dynamical properties radically different from those of a regular one. In particular, the

homogeneous state of a granular gas is unstable to inhomogeneous fluctuations. The instability is demonstrated in the present paper in two simulated unforced systems of rigid disks, one of whose collisions are nearly elastic and the other highly inelastic. It is found that as the gas evolves from a homogeneous and isotropic initial state, it undergoes a transition to a state which is highly inhomogeneous. The two regimes are characterized by well-defined global statistical properties such as the flatness of the fluctuating velocity distribution and the decay rate of the average granular temperature. The post-transition regime is characterized, in the nearly elastic case, by a persistent organization of the mass and velocity field into two shearing layers; and in the highly inelastic case, by the formation of dense and highly pronounced wandering clusters of particles. A linear stability analysis of the Richman-Jenkins equations of motion in the dilute limit shows that the homogeneous state, corresponding to the initial condition prescribed in the simulations, is indeed unstable to density fluctuations. Moreover, it is also shown that although the other fluctuations decay, they do so at a slower rate than the homogeneous temperature does when the wavenumber satisfies the condition $kl_0 < \mathcal{O}(\sqrt{\epsilon})$. Hence these fluctuations can also be considered to be unstable, since they may dominate the dynamics of the temperature in the long time limit.

A spectral analysis of the mass and momentum densities of the decaying granular gas at successive times reveals that one or more momentum modes grow to dominate all others in the momentum spectrum before the growth of the corresponding modes in the mass spectrum. Thus the picture of a momentum fluctuation (which is of a wavelength sufficiently long to outlive the decay of the initial temperature) arising to dominate the dynamics of the system, and thereby dictating the dynamics of the temperature (after the effect of its initial value has decayed away), is used in the nonlinear analysis presented in Section 2.4.3. There we have shown that a shear fluctuation give rise to a temperature inhomogeneity which in turn gives rise to a pressure gradient. The latter then causes motion of mass which leads to cluster formation. For the clustering process to be possible, the diffusive processes which tend to oppose the inhomogeneity due to the clustering must be slower than the mass motion. This implies a lower bound on the length scale of variation of the

inhomogeneity. However, it takes lesser time for the mass to move when this length scale is shorter. Hence the fastest (and therefore dominant) clustering process must correspond to the shortest length scale consistent with the diffusive lower bound. This length scale, given by $L_0 \sim l_0/\sqrt{\epsilon}$, has been verified in our numerical simulations.

The fact that typical granular systems are inhomogeneous is to be taken into account in any coarse-graining procedure designed to produce effective homogeneous equations of motion and corresponding boundary conditions. Even when the dimensions of the system are too small to give rise to clustering, the density distribution and the stress distribution will be strongly influenced by the aforementioned inhomogeneities. It follows that the inherent instability of homogeneous granular systems is of direct consequence to engineering applications.

Chapter 3

Cluster Dynamics in Granular Shear Flows

In this chapter, microstructural properties of dilute simple shear flows ('Lees-Edwards' systems) of rigid inelastic disks are studied using numerical simulations. One of the possible states of the flow when it is statistically stationary consists of dense strips aligned along the extensional axis of the shear (i.e. at 45 degrees to the streamwise direction). These strips are interspersed among relatively dilute strips of a similar orientation and size. Depending on the inelasticity, the dense strips may have an inner structure consisting of dense clusters elongated along the strip in which they lie. These clusters are spontaneously created by the dynamics of the system, whose initial condition is a state of uniform density and granular temperature, and uniform shear. Once created, the clusters are not stationary, since they are rapidly rotated and stretched by the shear. Nevertheless, the spatial orientations of the clusters remain mostly along the extensional axis. This orientation is maintained by a highly time-dependent and strongly nonlinear mechanism by which a cluster that has rotated away from the extensional axis scatters into an adjacent cluster, leading to the dispersion of the particles in both clusters. The dispersed particles subsequently reorganize into new clusters aligned along the extensional axis. By maintaining the orientation of the clusters, the scattering mechanism stablizes the type of 'stripwise clustering' microstructure that is observed. We examine here the scattering process as well

61
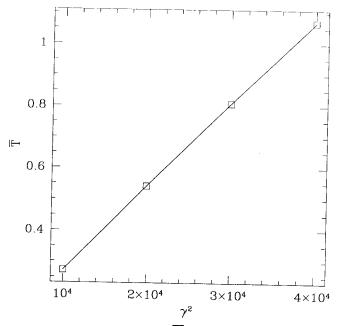
Figure 3.1: **The average temperature, $\overline{T}$, versus the square of the shear rate, γ^2.** The data are obtained from systems whose parameters other than γ are given by $\tilde{e} = 0.8, N = 200000, L_x = L_y = 1$ and $\bar{\nu} = 0.05$. The solid line through the data points is drawn to guide the eye.

as the physical mechanism responsible for the emergence of clusters. We show by means of spectral analyses of the various field variables that for a given value of the coefficient of restitution $\tilde{e}$ the dominant spatial scale L_0 in the microstructure corresponding to the separation between clusters is given by (1.1). We also examine other microscopic aspects of the flow such as the stress distribution and distributions of impact parameters and free paths.

3.1   Microstructure and Cluster Dynamics

3.1.1   Global Characteristics

An elastic system subject to the Lees-Edwards boundary conditions will heat up monotonically while remaining in a state whose temperature, density and macroscopic velocity gradient are spatially uniform. The inelastic system, on the other hand, has an internal energy sink due to the inelastic collisions. Hence it will, when

subject to the same boundary conditions, reach a state with a steady average granular temperature that is determined by the balance between the rate of shear heating and the rate of inelastic dissipation. In the simulation, a state of the system is considered to be steady if there is no drift in the values of the average granular temperature and the flatness of the fluctuating velocity distribution (cf. (1.8)); that is, these quantities attain (up to statistical fluctuations) constant 'equilibrium' values. The steady global average granular temperature, $\overline{T}$, defined following (1.7), obeys the following empirical relation

$$\overline{T} = A\frac{\gamma^2\sigma^2}{\overline{\nu}^2}\left(\frac{1}{1-\tilde{e}^2} + B\right). \tag{3.1}$$

which we have found to closely fit the numerical data. Here $A \simeq 0.080$ and $B \simeq -0.54$ are dimensionless constants. The ratio $\sigma/\overline{\nu}$ is proportional to the mean free path in a homogeneous system of solid fraction $\overline{\nu}$. Figures 3.1, 3.2 and 3.3 illustrate this relationship by comparing the values of $\overline{T}$ in systems characterized by different values of $\tilde{e}$, γ and $\sigma^2/\overline{\nu}^2$. The straight line through the data points in Fig. 3.2 is the dilute limit relationship between $\overline{T}$ and $\tilde{e}$ as derived by Jenkins and Richman in Ref. [39]. Following equations (70) and (71) in Ref. [39], this relationship is:

$$\overline{T} = \frac{\pi}{(1+\tilde{e})^2(7-3\tilde{e})^2}\frac{\gamma^2\sigma^2}{\overline{\nu}^2}\left(\frac{1}{1-\tilde{e}} - \frac{7}{16}\right). \tag{3.2}$$

It is easy to check that (3.1) and (3.2) yield close results as $\tilde{e}$ approaches unity. It should be noted that the theory in Ref. [39] is derived for a spatially uniform and time-independent shear flow, whereas the actual flow has a highly non-uniform and highly time-dependent microstructure. It is therefore somewhat surprising that (3.2) agrees so well with numerical results. It would be interesting to discover which average quantities are unaffected by the existence of microstructures and the reasons for their being unaffected.

The external parameters relevant to shear flow are the coefficient of restitution, $\tilde{e}$, the total number of particles, N, the value of the velocity at the horizontal boundaries $\pm U/2$, the horizontal and vertical dimensions of the enclosure, L_x and L_y, respectively, and the diameter, σ, of the disk. Although some appropriate dimensionless quantities can be constructed from the above parameters, we find it instructive to leave some quantities in dimensional form which we will use to characterize the flow. One useful
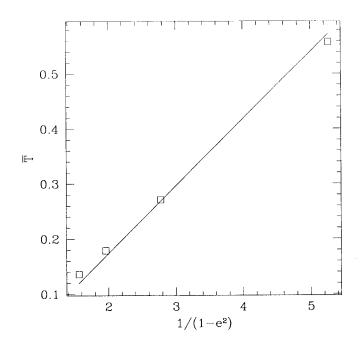
Figure 3.2: The average temperature, $\overline{T}$, versus $\tilde{e}$. The data are obtained from systems whose parameters other than $\tilde{e}$ are given by $N = 200000, U = 100, L_x = L_y = 1$ and $\bar{\nu} = 0.05$. The solid line through the data points is the prediction of the generalized Gaussian theory of Jenkins and Richman (cf. Section 5.3).
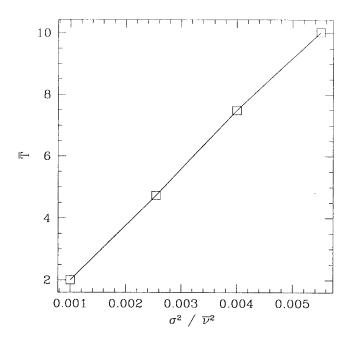
Figure 3.3: The **average** temperature, $\overline{T}$, versus $\sigma/\overline{\nu}$. The data **are** obtained from systems whose parameters other than $\overline{\nu}$ are given by $N = 10000, U = 100, L_x = L_y = 1$ and $\tilde{e} = 0.8$ (note that the value of N here is smaller than the value for Fig. 3.1 and Fig. 3.2). The solid line through the data points is drawn to guide the eye.

dimensionless combination is the system's average solid fraction, $\bar{\nu} \equiv \pi N \sigma^2 / 4 L_x L_y$; and one useful dimensional combination is the average shear rate, $\gamma \equiv U/L_y$. Notice that the values of N, $\bar{\nu}$, L_x and L_y determine σ. Also, the value of γ merely sets the numerical value of the average granular temperature in the system (if the values of the other parameters are held fixed); and since the value of the temperature merely determines a time scale but has no further dynamical importance (it does not affect, for example, the order of collisions in the system), different systems with all the same parameters except for γ will be identical up to a trivial scaling in the time variable. We have indeed numerically verified that changing the value of γ while keeping the other parameters fixed has no effect on the shape, size or orientation of microstructures in the flow.

We also note that, as we shall see in Chapter 4, the value of the initial temperature plays a significant dynamical role in determining the final steady state of the system. We found that, in order for the system to converge to a state that exhibits the 'stripwise clustering' microstructure, the values to be used for the initial temperature should be 'close' to the temperature of the steady state (the precise meaning of 'close' will be made clear in Chapter 4). When these values are used, the steady state is independent of the precise value of the initial temperature. The average temperature of the steady state is then determined by γ and the other external parameters alone. In the rest of this chapter, we shall consider only steady shear flows of this kind and shall use γ, $\bar{\nu}$, as well as $\tilde{e}$, to characterize them.

3.1.2 Microstructural Features

Here we describe the microstructural features of two specific sheared systems which we will refer to as System **III** and System **IV**. The parameters of System **III** are given by: $\tilde{e} = 0.9, N = 20000, U = 100, L_x = L_y = 1$ and $\bar{\nu} = 0.05$; while the parameters of System **IV** are given by: $\tilde{e} = 0.6, N = 200000, U = 100, L_x = L_y = 1$ and $\bar{\nu} = 0.05$. These parameters determine the particle diameter σ and mean free path l, which are given, for System **III**, by $\sigma = 0.00178$ and $l \simeq 1/71$, and for System **IV**, by $\sigma = 0.000564$ and $l \simeq 1/226$ (the mean free path in a two-dimensional system is defined as $l = L_x L_y / 2N\sigma$). Both systems are dilute but System **III** is nearly

elastic while System **IV** is highly inelastic. The reason the number of particles in System **III** is made much smaller than that in System **IV** is that we wish to demonstrate the bifurcation between quasihomogeneous and highly inhomogeneous states determined by whether the intercluster distance, L_0, given by (1.1), can be accomodated in the system. The parameters for System **III** are chosen so that the value of L_0 for the system is of the order of its linear dimension, L_x, whereas the parameters for System **IV** are chosen so that the value of L_0 is much smaller than its linear dimension. We will see that the properties of a quasihomogeneous system (which is also a 'small' system since the condition of whether the system size is larger than L_0 is equivalent, in the case of a fixed system volume, to whether the number of particles in the system is larger than a given threshold) is qualitatively different from an inhomogeneous (or 'large') system. In particular, clusters are created only in the 'large' system but not in the 'small' system, and the values of the stresses in the 'small' system are closer to the values predicted by kinetic theories of granular flows than those in the 'large' system.

We will now present some of the properties of System **III** and System **IV** such as their streamwise-averaged flow properties and the various macrofields of density, granular temperature, kinetic and collisional stresses. A plot of the particle configuration for System **III** at a time corresponding to the lapse of 200 collisions per particle following the initial condition is shown in Fig. 3.4. A vector plot of the velocity field is superposed on this plot. A plot of the density field for System **III** at the same time is shown in Fig. 3.5 as a shaded contour plot. The values of $\overline{T}$ and the flatness, κ, are statistically stationary at this time (see Fig. 3.6). The density contour plot shows that weak flow-scale inhomogeneities in the form of thick strips aligned along the extensional axis of the shear and spanning the system exist in the flow. The arrangement of these strips is such that the slightly denser strips are interspersed among slightly less dense strips of a similar size and orientation. The internal structure of these strips, though still weakly inhomogeneous, does not contain the elongated dense clusters that exist in highly inelastic sheared systems. The temperature, collisional and kinetic pressure fields in System **III** at the same time as that corresponding to the density field shown in Fig. 3.5 are shown in Fig. 3.7, Fig. 3.8 and Fig. 3.9
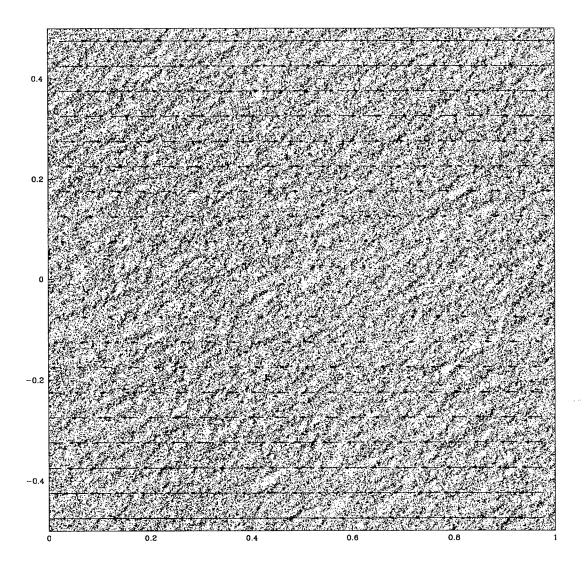
Figure 3.4: The particle configuration for System **III** on which a vector plot of the velocity field is superposed. The time here corresponds to 200 collisions per particle following the initial condition.

respectively. One may observe by comparing Fig. 3.7 and Fig. 3.5 that regions of higher densities correspond to regions of lower temperatures and vice versa. A study of Fig. 3.8 and Fig. 3.5 also shows that regions of high collisional pressure correspond to regions of high density and vice versa. The qualitative relationship between the kinetic pressure and the density is similar to that between the temperature and the density. The collisional pressure is, on the average, one order of magnitude smaller than the kinetic pressure. This is reasonable since the system is relatively dilute. The spatial structure of the kinetic and collisional pressure fields are similar to that of the density field, that is, they consist of diagonal and weakly inhomogeneous strips that span the linear dimension of the flow. This quasi-homogeneous microstructure is to be contrasted with the highly inhomogeneous structure in System **IV**, which we shall examine next.

A particle configuration plot for System **IV** at a time corresponding to the lapse of 100 collisions per particle following the initial condition is shown in Fig. 3.10. A vector plot of the macroscopic velocity field is superposed on the particle configuration plot. The corresponding density field is shown in Fig. 3.11 as a shaded contour plot. These plots shows that dense and anisotropic local agglomerations of particles occur throughout the flow field in the form of elongated clusters that are oriented mostly along the extensional axis of the shear. Other orientations for these clusters are also observed—they range between 0 and 45 degrees measured counterclockwise from the streamwise direction. The reason for the angles of orientation to lie exclusively in this range will be explained in Section 3.1.4. The stripwise organization of the clusters can still be discerned in these plots, though the strips in this case are 'pinched' and 'bent' in several places along their lengths and do rarely span the system, in contrast to those found in System **III**, which were more definitely formed and of a larger spatial scale. Just as the dense strips in System **III** are interspersed among dilute strips of a similar orientation and size, the clusters in System **IV** are also interspersed among relatively dilute regions of a similar shape, orientation and size. The symmetry of the dense and dilute regions can be appreciated if one imagines that the gray-scale shading is reversed in Fig. 3.11, i.e. that the lighter shaded regions correspond to more dilute regions instead of denser regions. Then it is evident that the dilute regions have the
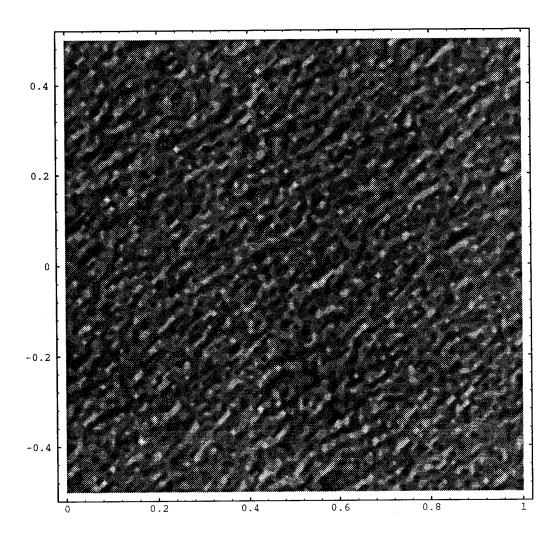
Figure 3.5: The density field for System **III** at a time corresponding to 200 collisions per particle following the initial condition. The shade code is: lighter gray for higher densities and darker for lower densities.

Figure 3.6: Flatness and average temperature as function of time in System **III**.
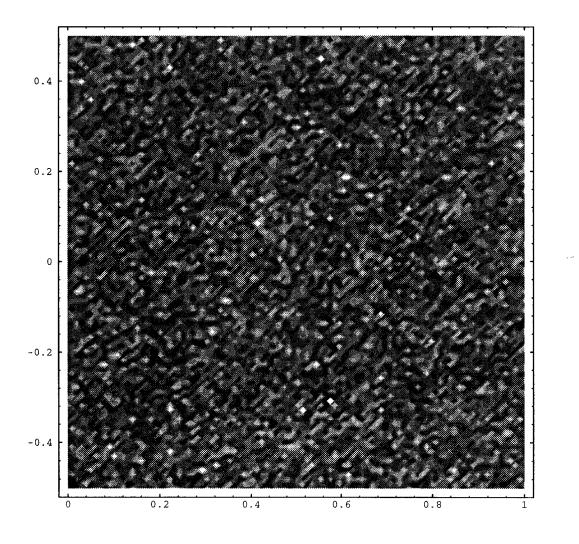
Figure 3.7: The granular temperature field for System **III** at a time corresponding to 200 collisions per particle following the initial condition. The shade code is: lighter gray for higher temperatures and darker for lower temperatures. A comparison with Fig. 3.5 shows that regions of higher temperature correspond to regions of lower density and vice versa.

Figure 3.8: The collisional pressure field for System **III** at a time corresponding to 200 collisions per particle following the initial condition. The shade code is: lighter gray for higher pressures and darker for lower pressures. A comparison with Fig. 3.5 shows that regions of higher pressure correspond to regions of higher density as well.

Figure 3.9: The kinetic pressure field for System **III** at a time corresponding to 200 collisions per particle following the initial condition. The shade code is: lighter gray for higher pressures and darker for lower pressures. A comparison with Fig. 3.5 shows that regions of higher kinetic pressure correspond to regions of lower density.

same spatial structure as the dense regions. The stripwise organization of the clusters in System **IV** will be refered to as the 'stripwise clustering microstructure'.

The temperature, collisional and kinetic pressure fields for System **IV** at the same time as that corresponding to the density field shown in Fig. 3.11 are shown in Fig. 3.12, Fig. 3.13 and Fig. 3.14 respectively. The qualitative relationships of these macrofields to each other are the same as those for the corresponding macrofields of System **III**.

3.1.3   Qualitative Relationships between the Macrofields

The qualitative relationships between the values of the macrofields as brought forth by comparing Figures 3.5–3.9 for System **III** and Figures 3.11–3.14 for System **IV** can be understood on the basis of the fact that the rate of collisions in a denser region is typically higher than that in a less dense region (if the temperatures of the two regions are comparable), since this rate is proportional to the square of the density. The higher rates of collisions in denser regions are responsible for the higher rates of loss of kinetic energy in these regions relative to the rates in the more dilute regions. As a result, the temperature in dense regions decreases, causing the pressure in these regions to decrease as well. The difference in the pressures in the dilute and dense domains will cause a mass migration from the former into the latter, the overall effect being a further increase in the density in regions that were denser to start with. The temperature may yet be reduced further since the influx of mass increases the rate of collision and therefore also the rate of energy dissipation. However, the kinetic energy in the flow is being continually replenished by a pumping mechanism, which in this case is the heating due to the shear. This heating causes the temperature to rise and thus restores a high density region to a lower density. Clearly, for the temperature of a dense domain to be lower than that of a dilute region and for it to persist at the lower value, or conversely for the temperature of a dilute region to persist at its higher value (with similar statements to be made for the persistence of the other macrofields at their different magnitudes), a nonlinear process involving relatively long-time dynamics of the flow must be involved. This process involves the interplay of long-lived long-wavelength density fluctuations and local inelastic
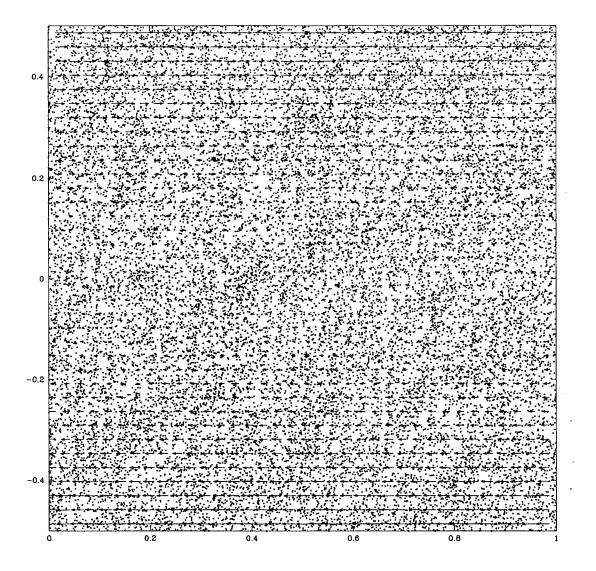
Figure 3.10: The particle configuration for System **IV** on which a vector plot of the velocity field is superposed. The time here corresponds to 100 collisions per particle following the initial condition.
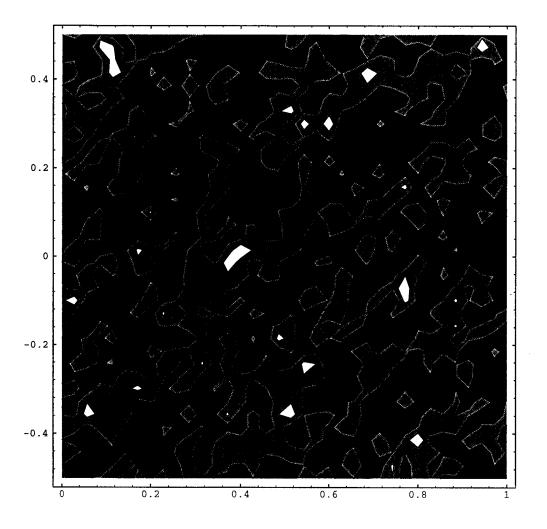
Figure 3.11: The density field for System **IV** at a time corresponding to 100 collisions per particle following the initial condition. The shade code is: lighter gray for higher densities and darker for lower densities.

Figure 3.12: The granular temperature field for System **IV** at a time corresponding to 100 collisions per particle following the initial condition. The shade code is: lighter gray for higher temperatures and darker for lower temperatures. A comparison with Fig. 3.11 shows that regions of higher temperature correspond to regions of lower density and vice versa.
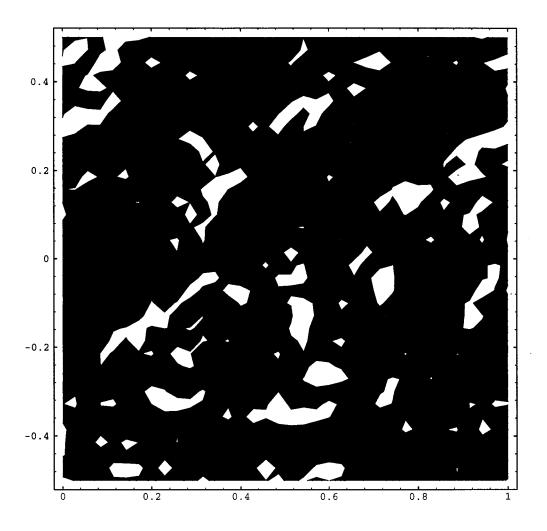
Figure 3.13: The collisional pressure field for System **IV** at a time corresponding to 100 collisions per particle following the initial condition. The shade code is: lighter gray for higher pressur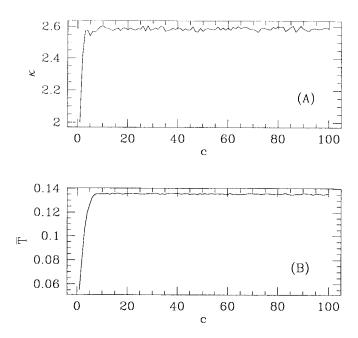es and darker for lower pressures. A comparison with Fig. 3.11 shows that regions of higher pressure correspond to regions of higher density as well.
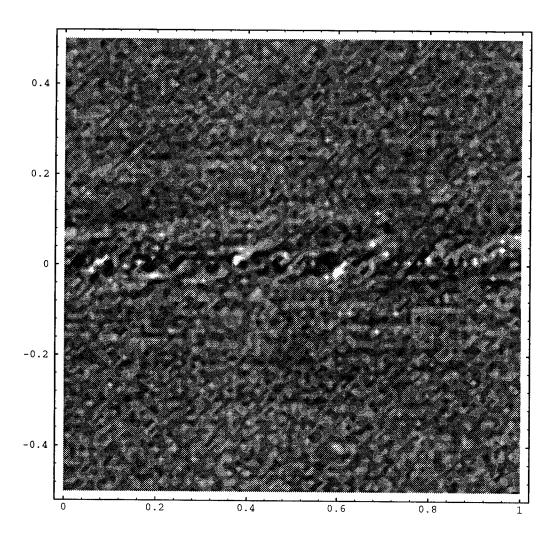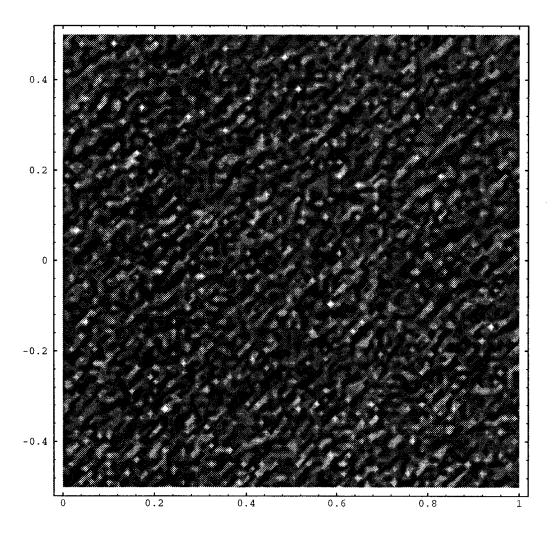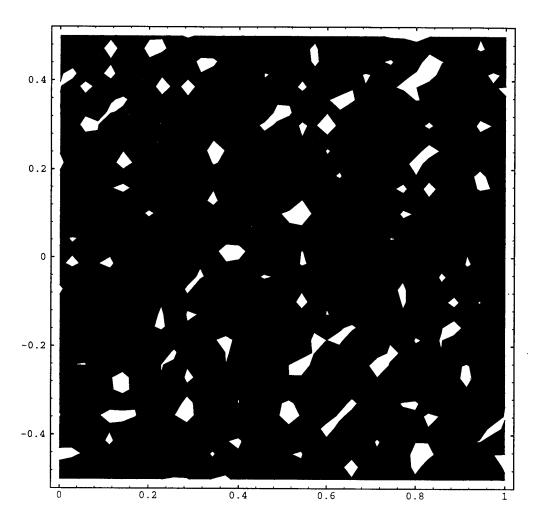
Figure 3.14: The kinetic pressure field for System **IV** at a time corresponding to 100 collisions per particle following the initial condition. The shade code is: lighter gray for higher pressures and darker for lower pressures. A comparison with Fig. 3.11 shows that regions of higher kinetic pressure correspond to regions of lower density.

dissipation, which is described next.

Since the granular system has a large number of degrees of freedom, one expects statistical fluctuations of almost every macroscopic physical quantity to occur in it. Now consider the mass density field, which is a hydrodynamical variable whose long-wavelength fluctuations evolve slowly in time (since their time scales are *diffusive*, i.e. proportional to the squares of the corresponding wavelengths). We see that the rate decay of a fluctuation in the density field can be slow with respect to, for example, the rate of energy dissipation. This is because the latter depends on the local density and temperature, while the former can be as slow as its wavelength is long. Hence once a hydrodynamic density fluctuation of a sufficiently long characteristic length is created, it will eventually dominate the dynamics of the system, slaving the relatively fast variable, the temperature, to it. Thus, when one considers a density fluctuation, the regions in which the density is higher will 'cool' faster and thus have a lower temperature and pressure than the regions in which the density is lower. The higher density regions will therefore tend to draw more mass into themselves. Note that the lowering of the temperature and the subsequent mass migration are possible because these processes are fast relative to the diffusive decay of the density fluctuation. The drawing of mass into the higher density regions decreases the temperature of these regions even further, thus causing even more mass to be drawn into them. The granular system therefore has *positive feedback*, that is, a small departure from a state of uniform density will generate an internal field (which is due to the pressure difference) that amplifies the departure, leading finally to the creation of high density 'mass attractors' in the flow.

The influx of mass into a 'mass attractor' does not continue unabated, since the system is continually being heated by the shear. The mass influx will correspond to an energy influx, which tends to increase the temperature, and also the pressure, and thereby oppose further influx of mass. In addition, the presence of a density gradient will cause mass to diffuse out of the higher density regions. Hence, the creation of nontransient regions of higher density—i.e. the clustering of particles—is possible only if the rate of lowering of the temperature in these regions is fast enough to prevent the build-up of a high pressure and if the diffusion of particles out of these regions is

slower their influx. When these conditions are met, we obtain a flow in which clusters are created and are separated by a characteristic length scale determined by these conditions. This length scale is discussed further in Section 3.2.1.

3.1.4 Cluster-Cluster Interaction

The stripwise clustering microstructure described in Section 3.1.2 has been studied before both theoretically[48, 49] and in computer simulations[40]. The origin of this type of microstructure may be described as follows. A short-time instability, i.e. a mode that grows transiently but decays on asymptotically long time scales, first gives rise to a periodic density fluctuation whose typical wavevector is aligned approximately along the compressional axis of the shear (i.e. at 135 degrees from the streamwise direction). Such a wavevector corresponds to structures which lie at 45 degrees to the streamwise direction. Using linear stability analysis[48, 49, 50], one can show that these transiently growing modes arise in the (initially uniform) density field of a uniform shear flow governed by the equations for granular flow derived by Jenkins and Richman[5, 51] and also by the equations derived by Lun *et al*[52]. These stability analyses show that the wavevectors that correspond to the most unstable modes lie approximately along the extensional axis of the shear. The stability analysis presented in Ref. [50] of the two-dimensional equations derived in Ref.[51] shows that the wavevectors corresponding to the most unstable mode lie *exactly* along this axis. Note also it is straightforward to show (see for example the appendix of Ref. [53]) that after long times, all infinitesimal fluctuations eventually decay and thus granular shear flow is linearly stable. The density fluctuation, while in its transient growth stage, initiates within the diagonal strips the clustering process described in Section 3.1.3 which leads to the creation of dense clusters within the strips. Now, these clusters are by no means static structures, since they are being continually convected by the flow. Morever, they scatter into each other as they are being convected, thus producing a very complex dynamics that involves rapid dispersion and reorganization of mass in the flow. Nevertheless, the stripwise clustering microstructure persists. We believe that it is by means of the cluster-cluster interactions, hand-in-hand with the nonlinear clustering process, that this type of microstructure is maintained in the

flow. We will now examine cluster interactions in the shear flow.

Since clusters are convected as coherent structures until they are modified by interactions with each other, we will first make a few remarks on the effect of the velocity field on structures in the flow. It turns out that the velocity fields in both System **III** and System **IV** correspond to an extremely uniform linear shear field. This is the case despite the rapid temporal variations in the spatial structures of both systems. It can be seen in Fig. 3.15 and Fig. 3.16 that the profiles of the streamwise-averaged velocity fields respectively of System **III** and System **IV** are linear across their domains. In fact, the streamwise-averaged velocity fields for both systems remain linear at all times. By computing the corresponding vorticity fields, we have verified that the velocity fields in both systems correspond everywhere to a very uniform shear field. Some other streamwise-averaged properties for System **III** and System **IV**, such as their temperature and number density profiles, are shown in Fig. 3.15 and Fig. 3.16 respectively as well. These profiles show variations with typifiable length scales on an essentially flat background.

It is easy to see that a two-dimensional uniform shear field, $\mathbf{V}(x, y)$, with shear rate γ can be written as

$$\mathbf{V}(x, y) = \frac{\gamma}{2} \left[(y, x) + (y, -x) \right]. \tag{3.3}$$

Equation (3.3) is written so that the velocity field is decomposed into two parts, one of which is irrotational and the other solenoidal (i.e. divergence-free); it also results from writing the strain rate tensor (i.e. the velocity gradient tensor) as a sum of symmetric and anti-symmetric parts. The velocity field corresponding to the first term in the square brackets in (3.3) is an irrotational stretching field (cf. Fig. 3.17(A)) which tends to compress a flow structure along the 135-degrees direction and stretches it along the 45-degrees directions (all angles here are measured relative to the streamwise direction); these directions are parallel to respectively the compressional and extensional axes of the shear. The velocity field corresponding to the second term in the square brackets in (3.3) (cf. Fig. 3.17(B)) is just a clockwise solid body rotation of the system. Thus all structures in the shear flow are permanently and simultaneously compressed, stretched and rotated by the flow.
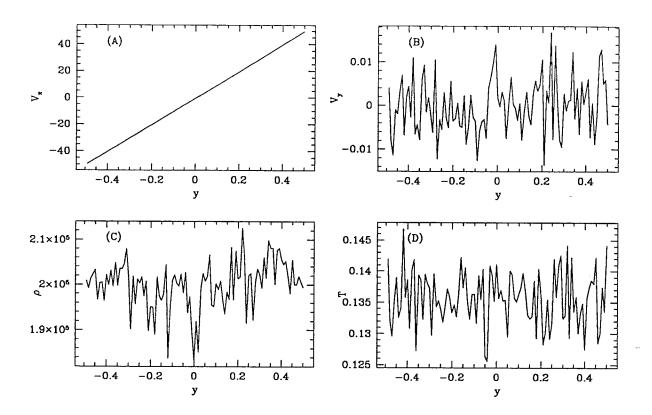
Figure 3.15: Streamwise-averaged flow properties for System **III** : (A) V_x; (B) V_y;
(C) density, ρ; (D) temperature, T. Notice that all profiles are essentially uniform,
the relative fluctuations being very small.
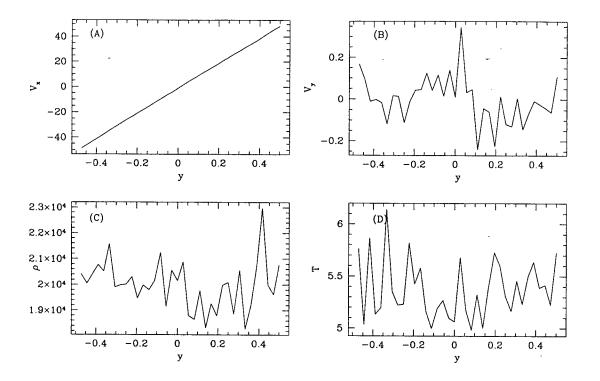
Figure 3.16: Streamwise-averaged flow properties for System **IV** : (A) V_x; (B) V_y; (C) density, ρ; (D) temperature, T. Notice that all profiles are essentially uniform, the relative fluctuations being very small.
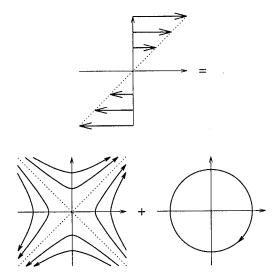
Figure 3.17: The decomposition of the velocity field into a sum of a irrotational stretching/compressing field and a pure rotation.

It seems then that there should, at any instant of time, be clusters aligned at angles of inclination that are not equal to 45 degrees. However, since the cluster starts off at 45 degrees and is rotated clockwise, and since the longer the cluster is rotated, the more likely it is to collide with adjacent clusters and be dispersed by the collision, a distribution of angles of inclination for the clusters emerges. This distribution is weighted towards angles close to 45 degress and tails off as the angle becomes smaller. In fact, as we shall see in Section 3.2.1, the fourier spectra of the density field show that its power is concentrated in peaks that correspond to spatial structures that are aligned at angles approximately between 0 and 45 degrees. The peaks corresponding to structures aligned at close to 45 degrees are stronger than those corresponding to structures aligned at much less than 45 degrees. These peaks are weaker for smaller angles of alignment. Very little power appears in the spectrum outside the range that correspond to angles between 0 and 45 degrees and thus very few spatial structures are aligned at angles beyond this range.

The kinematics of cluster interaction can be described with the help of a sequence of closely cropped contour plots that show the density field around two neighboring clusters at successive instants of time. Fig. 3.18 shows a sequence of contour plots of
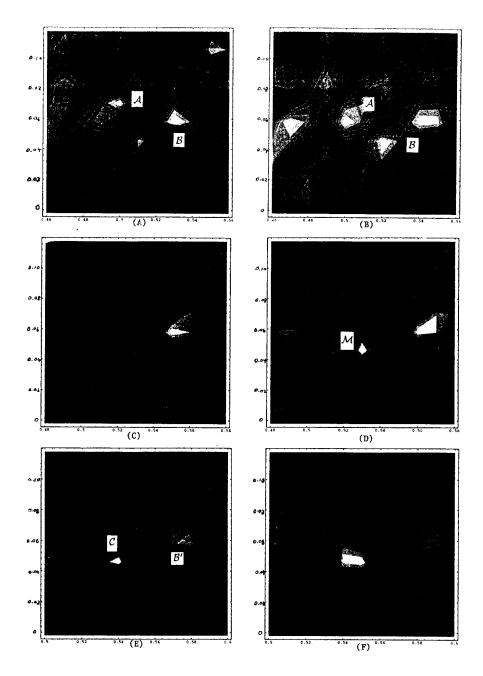
Figure 3.18: A close view of the density field at successive instants of time around two clusters interacting with each other. The shade code for the contour plots is: lighter greys for higher density and darker for lower densities. The detailed explanation of the plots are provided in the text.

the density field in a small window that is just large enough to show a few clusters lying within two adjacent dense strips. These plots are produced from snapshots of System **IV** at successive instants of time which were separated by an interval that corresponds to the lapse, on the average, of 0.25 collisions per particle in the system (this means that a total of $N/4$ collisions, where N is the number of particles in the system, have occurred between one plot and the next). Fig. 3.18(A) shows two clusters that were oriented approximately along the extensional axis of the shear with the cluster labeled $\mathcal{A}$ in the figure lying above and to the left of the cluster labeled $\mathcal{B}$. In Fig. 3.18(B), which shows the density field 0.25 collisions per particle later, we see that both clusters $\mathcal{A}$ and $\mathcal{B}$ have rotated slightly away from the extensional axis and they are now closer to each other. Both clusters have also been stretched slightly along the extensional axis by the flow. We believe the fact that the clusters appear to have now been 'drawn' closer to each other is *not* a dynamical effect. That is, it is not due to the presence of an attractive internal field between the clusters; but rather it is a purely kinematic effect that is due entirely to convection. This conclusion follows from the fact that the motion of each cluster as a whole is found to closely match the motion dictated by the velocity field.

It is clear that since the velocity field (3.3) is linear, a local frame of reference moving at the local value of the velocity given by (3.3) will have a (relative) velocity field in it that has the same structure as (3.3). That is, the velocity field, $\tilde{v}$, in the local frame is given by $\tilde{v} = (\gamma/2)[(\tilde{y}, \tilde{x}) + (\tilde{y}, -\tilde{x})]$, where $\tilde{x}, \tilde{y}$ are coordinates in the local frame. This means that clusters in the local frame will appear to rotate about the origin of the frame, and two clusters that are close enough together whose geometric centers lie approximately along the same horizontal line will certainly collide into each other as they are being rotated. This is roughly the situation with the two clusters shown in Fig. 3.18. The collision that occurs between them is depicted in Fig. 3.18(C) and Fig. 3.18(D): in the former figure, the bottom half of cluster $\mathcal{B}$ is seen to have begun to scatter into cluster $\mathcal{A}$, creating an expanded region of dispersed particles (though still of moderately high density). Then, in the latter figure, a 'mass attractor', labeled $\mathcal{M}$, forms out of this region while the top half of cluster $\mathcal{B}$ breaks away from what is now the amalgamation of its lower half with cluster $\mathcal{A}$. This amalgamation

is then compressed in the 135 degrees direction and stretched in 45 degrees direction by the shear, causing a new cluster elongated along the latter direction to take shape. This cluster becomes more fully formed in Fig. 3.18(E) and is labeled C. It can also be seen in Fig. 3.18(E) that the top half of cluster C is about to scatter into the bottom half of cluster B' (which is the broken-off descendant of cluster B in Fig. 3.18(C)). The outcome of this scattering is again a dilated region of dispersed particles as shown in Fig. 3.18(F), and the cycle of formation of a new cluster through the appearance of a mass attractor in this region then repeats. The fact that the scattering produces a dilated region is evidently due to the fact that part of the kinetic energy of the colliding clusters is converted into 'heat', i.e. the kinetic energy of random motion of the particles, which causes the temperature, and hence the pressure, of the region to increase, thus dispersing the particles in it.

The paradigm of this process of cluster convection and cluster scattering followed by dilation and mass reorganization applies throughout the system. Hence, even though the spatial orientations of the clusters in the system appear to remain mostly along the extensional axis, what actually happens is that new clusters are being continually created in this direction. The structure of the other field variables, such as the temperature, kinetic and collisional stress tensors, follow this time-dependent paradigm. That is, a local organized inhomogeneity is first created along the extensional axis and is convected and then dispersed or modified by cluster interactions before a new inhomogeneity is reorganized in its place. Since a region of average density in the flow is always (nonlinearly) unstable with respect to the creation of clusters, the mass reorganization stage that follows the dilation stage is due to the same nonlinear clustering mechanism that is responsible for the creation of diagonally aligned clusters from the initial uniform density field. Thus, in short, the stripwise clustering microstructure in simple granular shear flows is stabilized through the combined effect of a nonlinear clustering instability, cluster convection and a complex process of cluster interaction and mass reorganization.
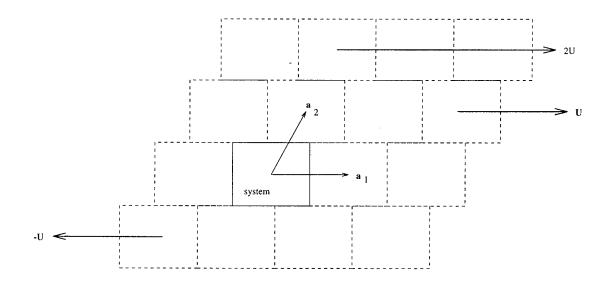
Figure 3.19: The Lees-Edwards system and its periodic images

3.2 Spectral Analyses and Microscopic Dynamics

In this section, we will present the Fourier spectra of the density and momentum fields of System **III** and System **IV** as well as some results of spectral analyses of other sheared systems characterized by various combinations of the external parameters. We will show that the typical length scale in the density fields of systems with different values of the coefficient of restitution, $\tilde{e}$, follow the relationship given in (1.1). In addition, we will examine some microscopic features of the dynamics such as the impact parameter distribution and the distribution of free paths before collision. We will show that the latter distribution is highly anisotropic and that it deviates, in the regime of short free paths, from a strict exponential decay distribution that is usually assumed for a dilute gas.

3.2.1 Fourier Spectra

The Fourier spectra of the field variables are extremely useful because they serve to identify dominant scales in the microstructure that forms in the shear flow. The formulas for the Fourier transforms are the same as the ones used in Section 2.2 but

are listed here again for ease of reference. The Fourier transforms of the mass and momentum densities are:

$$\tilde{\rho}(\mathbf{k}) \equiv \frac{1}{2\pi} m \sum_{j=1}^{N} \exp(i\mathbf{k} \cdot \mathbf{r}_j) \tag{3.4}$$

$$\tilde{\mathbf{p}}(\mathbf{k}) \equiv \frac{1}{2\pi} m \sum_{j=1}^{N} \mathbf{v}_j \exp(i\mathbf{k} \cdot \mathbf{r}_j). \tag{3.5}$$

where $\mathbf{r}_j$ is the position vector of particle j in the system. In a periodic domain, the allowed wavevectors are $\mathbf{k} = (2p\pi/L_x, 2q\pi/L_y)$, where p and q are integers and L_x and L_y are the dimensions of the system. However, the Lees-Edwards boundary conditions are periodic in the Lagrangian frame for shear flow—i.e. they are periodic only after a local Galilean transformation that depends on the local mean velocity has been applied to the coordinate system—and they are not periodic in a static sense. We may obtain the wavevectors allowed by the Lees-Edwards boundary conitions as follows: let $\mathbf{a}_1$ and $\mathbf{a}_2$ be the 'basis vectors' for the lattice consisting of the system and its periodic images as shown in Fig. 3.19. These vectors are time-dependent since the periodic images move with time. Let $\tilde{p}$ be an integer such that $0 < L_y\gamma t - \tilde{p}L_x < L_x$, and define $[\gamma t] = \gamma t - \tilde{p}L_x/L_y$. Then we have $0 < [\gamma t] < L_x/L_y$ and the basis vectors can be written as

$$\mathbf{a}_1 = (L_x, 0) \tag{3.6}$$

$$\mathbf{a}_2 = ([\gamma t]L_y, Ly) \tag{3.7}$$

The lattice is invariant to translations $\mathbf{T} = \tilde{i}\mathbf{a}_1 + \tilde{j}\mathbf{a}_2$ of the origin, where $\tilde{i}$ and $\tilde{j}$ are integers. Thus any field variable $\psi(\mathbf{r}, t)$ at a given time t will satisfy

$$\psi(\mathbf{r}, t) = \psi(\mathbf{r} + \mathbf{T}, t) \tag{3.8}$$

If $\psi(\mathbf{r}, t)$ is expanded in a fourier series,

$$\psi(\mathbf{r}, t) = \sum_{\mathbf{k}} \psi_{\mathbf{k}}(t) \exp(i\mathbf{k} \cdot \mathbf{r}) \tag{3.9}$$

we have $\sum_{\mathbf{k}} \psi_{\mathbf{k}}(t) \exp(i\mathbf{k} \cdot \mathbf{r}) = \sum_{\mathbf{k}} \psi_{\mathbf{k}}(t) \exp(i\mathbf{k} \cdot \mathbf{r} + i\mathbf{k} \cdot \mathbf{T})$. The condition to be satisfied by the allowed wavevectors is therefore $\mathbf{k} \cdot \mathbf{T} = 2\pi M$, where M is an integer. It is easy to check that $\mathbf{k}$ is given by

$$\mathbf{k} = \tilde{l}\mathbf{k}_1 + \tilde{m}\mathbf{k}_2 \tag{3.10}$$
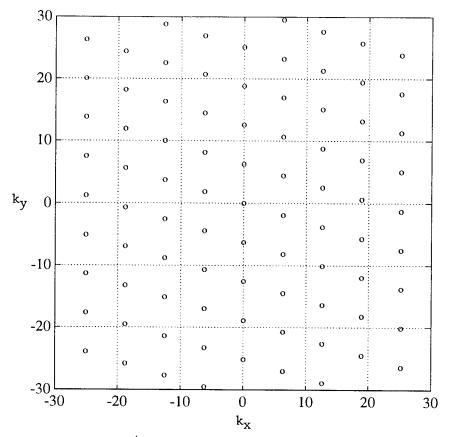
Figure 3.20: Sampling points in **k**-space at given instant corresponding to Lees-Edwards boundary conditions.

where $\tilde{l}$ and $\tilde{m}$ are integers, and $\mathbf{k}_1$ and $\mathbf{k}_2$ are the basis vectors for the 'reciprocal lattice' given by

$$\mathbf{k}_1 = \left(\frac{2\pi}{L_x}, -\frac{2\pi[\gamma t]}{L_x}\right) \tag{3.11}$$

$$\mathbf{k}_2 = \left(0, \frac{2\pi}{L_y}\right). \tag{3.12}$$

If $L_x = L_y$, then the horizontal and vertical intervals between the sampling points in **k**-space remains as those in the static case. However, the sampling points are no longer arranged on a square lattice but are arranged on a 'rhomboid' lattice whose tilt is time-dependent. A typical configuration of the sampling points in **k**-space at some given time is shown in Fig. 3.20. Although the Fourier decomposition of a field variable in this case consists of modes that are continuously being turned by the shear flow and are dependent on the time at which the field variable is given, the
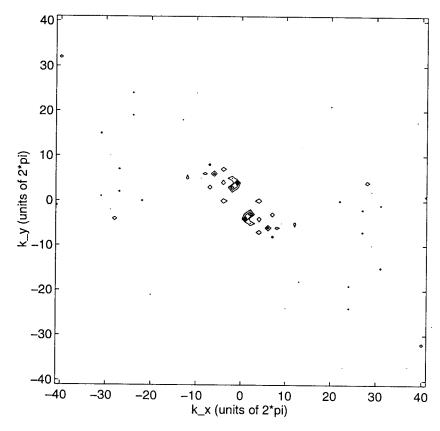
Figure 3.21: Power spectrum of the density field of System **IV** shown in Fig. 3.11.

interpretation of the spectrum remains unchanged. The spectrum is merely sampled at a different set of points which are shifted with respect to the ones corresponding to static periodic boundary conditions. The power in the spectrum along the 135 degrees direction (relative to the positive k_x axis) in k-space corresponds, just as in the static case, to spatial structures aligned at 45 degrees to the positive x-axis.

Fig. 3.21 shows a contour plot of the Fourier (power) spectrum of the density field for System **IV** shown in Fig. 3.11. The power spectrum, $R(\mathbf{k})$ is defined as

$$R(\mathbf{k}) \equiv \tilde{\rho}(\mathbf{k})\tilde{\rho}(\mathbf{k})^* \qquad (3.13)$$

where $\tilde{\rho}(\mathbf{k})$ is given by (3.4) and the superscript $*$ denotes complex conjugation. The wavevectors $\mathbf{k}$ for which $\tilde{\rho}(\mathbf{k})$ is computed are those given by (3.10). The plot in Fig. 3.21 is drawn with contours of constant $R(\mathbf{k})$. The contours correspond to equally spaced values of $R(\mathbf{k})$ between the minimum and maximum values in the spectrum. Fig. 3.21 shows that the dominant wavevectors are aligned at angles
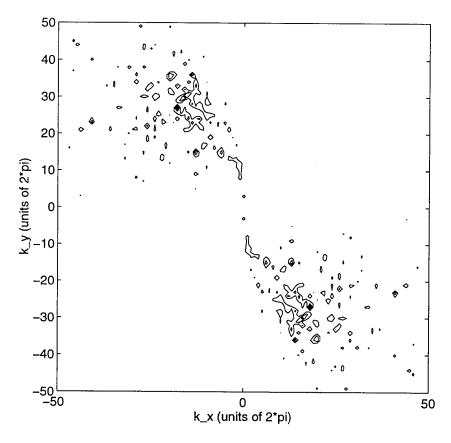
Figure 3.22: The power spectrum of the density field of System **III** shown in Fig. 3.5.

between 90° and 135° with respect to the positive k_x axis. This implies that spatial structures in the density field are aligned at angles between 0° and 45° (all angles are being measured with respect to the streamwise direction). The alignment of these structures can clearly be seen in the particle configuration shown in Fig. 3.10 and in the contour plot of the density field shown in Fig. 3.11. The corresponding spectrum for System **III** is shown in Fig. 3.22. The dominant wavevectors are again aligned between 90° and 135°, though their magnitudes are larger than those of the dominant wavevectors in System **IV**, indicating that the spatial scales in the density field in System **III** are smaller. Since the mean free paths in the two systems are different, we cannot directly compare their spatial scales. However, the comparison can be made if these scales are expressed in units of the mean free path of the corresponding system; if this is done, we find that the scales in System **III** are still smaller than those in System **IV**.

The power spectrum $\mathbf{P}(\mathbf{k})$ of the momentum field has two components correspond-ing respectively to the x- and the y-components of the momentum field. They are defined as

$$P_x = \tilde{p}_x(\mathbf{k})\tilde{p}_x(\mathbf{k})^* \tag{3.14}$$

$$P_y = \tilde{p}_y(\mathbf{k})\tilde{p}_y(\mathbf{k})^*. \tag{3.15}$$

where $\tilde{p}_x$ and $\tilde{p}_y$ are given by (3.5). If the sampling points are chosen to be those given by (3.10), it can be shown that the part of the momentum field due to the linear shear profile does not affect the power in the spectrum except at points on the k_y axis. Let the macroscopic momentum field, $\mathbf{p}(\mathbf{r})$ be written as $\mathbf{p}(\mathbf{r}) = \rho(\mathbf{r})\gamma y\hat{\mathbf{x}} + \mathbf{p}'(\mathbf{r})$, where $\hat{\mathbf{x}}$ is the unit vector along the x-axis and $\mathbf{p}'$ denotes the deviation of the field from the one due to the linear velocity profile alone. To assess the effect of the linear profile on the spectrum, we consider the Fourier transform of $\rho(\mathbf{r})\gamma y\hat{\mathbf{x}}$, assuming for simplicity that $\rho(\mathbf{r})$ is constant:

$$\int_0^1 dx \int_{-1/2}^{1/2} dy\, \rho(\mathbf{r})\gamma y \exp(ik_x x + ik_y y) = \rho\gamma \left(\frac{\exp(ik_x) - 1}{k_x}\right) \left(\frac{\sin\frac{k_y}{2} - \frac{k_y}{2}\cos\frac{k_y}{2}}{\frac{k_y^2}{4}}\right). \tag{3.16}$$

It is seen that the transform is zero when $k_x = 2n\pi$, where n is an integer not equal to zero. When $k_x = 0$, which corresponds to setting $\tilde{l} = 0$ in (3.10), the sampling points are $\mathbf{k} = \tilde{m}\mathbf{k}_1$, where $\tilde{m}$ is any integer, and the transform in (3.16) is no longer zero. Thus the transform is non-zero only when the sampling points lie on the k_y axis.

If instead of computing the Fourier transform of $\mathbf{p}(\mathbf{r})$ as given by (3.5), we compute the Fourier transform of $\mathbf{p}'(\mathbf{r})$, i.e. the following quantity,

$$\tilde{\mathbf{p}}'(\mathbf{k}) = m\sum_{j=1}^N (\mathbf{v}_j - \gamma y_j\hat{\mathbf{x}})\exp(i\mathbf{k}\cdot\mathbf{r}_j) \tag{3.17}$$

where y_j is the y-coordinate of the jth particle in the system, we would eliminate most of the power at the points on the k_y axis. However, the power is not completely eliminated, since a global trend (i.e. a variation whose length scale is of the order of the linear dimension of the system) exists in $\mathbf{p}'$ that is due to the fact that the total momentum of the system fluctuates around zero and may not be equal to zero at any given time. This fluctuation appears to be thermal in nature and its magnitude

is $\mathcal{O}(N^{-1/2})$ times the magnitude of the total momentum in, say, the top half (i.e.
$0 < y < L_y$) of the system. As a result of this fluctuation, the magnitude of the
total momentum in the top half of the system will be different from that of the total
momentum in the bottom half. It is found that the value of $\tilde{\mathbf{p}}'(\mathbf{k})$ at the points $\mathbf{k}$
on the y-axis are still about one order of magnitude larger than the power of the
(possibly more interesting) off-axis structures in the spectrum. Hence we have chosen
to ignore the power on the k_y axis in the $\tilde{p}'_x$ spectrum. Although a global trend may
also exist in $\tilde{p}'_y$, its magnitude is very small compared to the trend in $\tilde{p}'_x$ (since the
mean y-component of the momentum is zero) and it does not pose a problem to the
interpretation of the spectrum. Since we have ignored the power on the k_y axis in
the $\tilde{p}'_x$ spectrum, we have also ignored possible horizontal layering structures in the
velocity field. However, we have checked that the power at large values of k_y on the k_y
axis (at which the power due to the global trend in $\tilde{p}'_x$ is negligible) is small, and thus
there is no horizontal layering in the velocity field beyong the scales corresponding to
the global trend in $\tilde{p}'_x$.

The spectra P_x and P_y of the momentum field for System **III** are shown in Fig.
3.23 and Fig. 3.24 respectively. The corresponding spectra for System **IV** are shown
in Fig. 3.26 and Fig. 3.27. Fig. 3.23 shows that most of the peaks in P_x lie
between 90 degrees and 135 degrees with respect to the positive x direction, with
the stronger peaks lying at angles closer to 135 degrees. Thus, the structure of the
x-component of the momentum field, much like the structure in the density field,
consists of differentiated strips aligned mostly along the extensional axis of the shear.
This structure can be understood as follows: Consider the x-component of the mean
velocity along a line parallel to the x-axis which cuts the alternatingly dense and
dilute strips as shown schematically in the top portion of Fig. 3.25. This velocity
will in general not be equal to the value that is obtained by interpolating between
the values of the velocities at the top and bottom boundaries, but will fluctuate
around the interpolated value. The deviation from the interpolated value will be
smallest at points that correspond to the center of each dense and dilute strip and
will correspondingly be largest at the edges of each strip. The variation of the x
component of the velocity as a function of x is shown schematically in the bottom
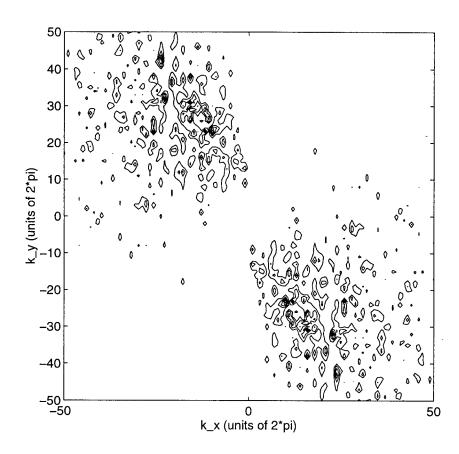
Figure 3.23: The power spectrum, P_x, of the x-component of the momentum field of System **III**.
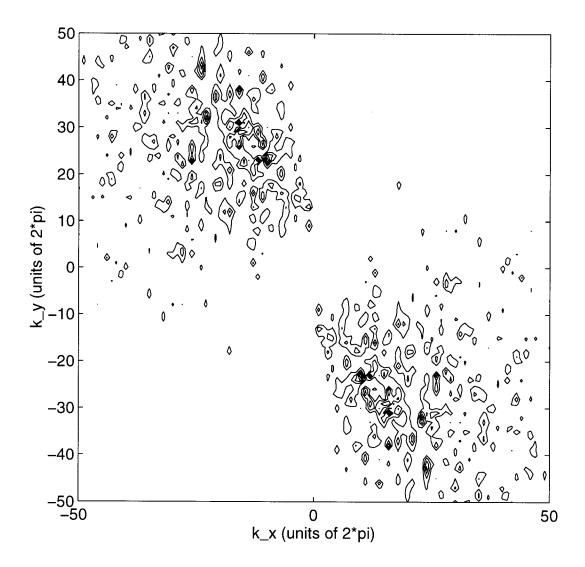
Figure 3.24: The power spectrum, P_y, of the y-component of the momentum field of System **III**.
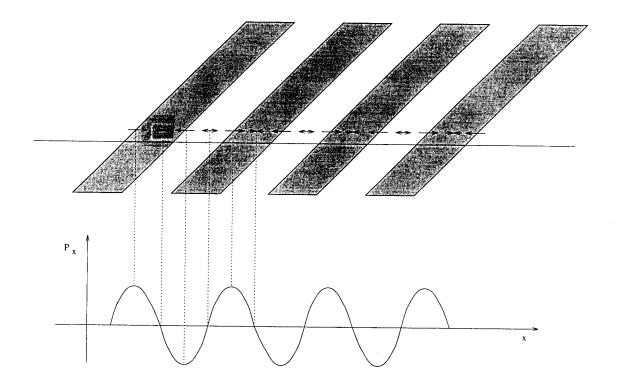
Figure 3.25: The structure of the x component of the velocity field and its relation to the stripwise organization of inhomogeneities in the density field.

portion of Fig. 3.25. This variation corresponds to the alternation of regions into which particles are converging, i.e. the denser strips, with regions from which particles are diverging, i.e. the more dilute strips, with the converging or diverging flows being strongest at the edges but 'stagnant' at the center of each strip. The structure in the y-component of the momentum field can also be explained in a similar way.

The question arises as to whether the aspect ratio of the flow domain plays a role in determining the alignment of the microstructure. We have performed other simulations of shear flows in domains whose aspect ratios are not equal to unity and have found in all cases that were checked that the alignment of the microstructures in the system is the same as that in System **III** and System **IV**. This alignment is therefore not due to the geometry of the flow domain but is rather a dynamical effect
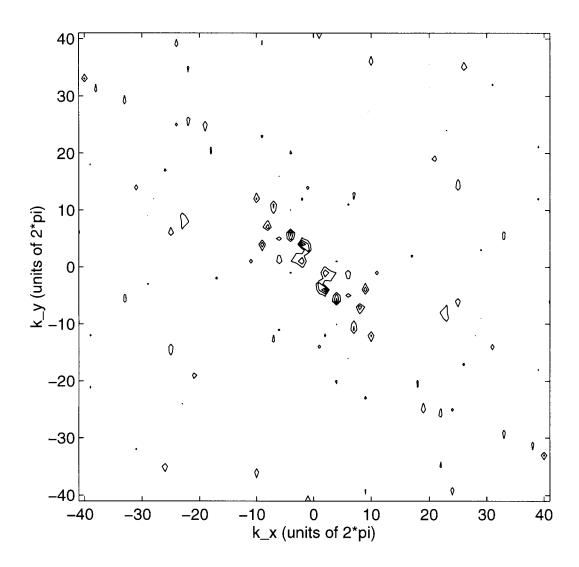
Figure 3.26: The power spectrum, P_x, of the x-component of the momentum field of System **IV**.
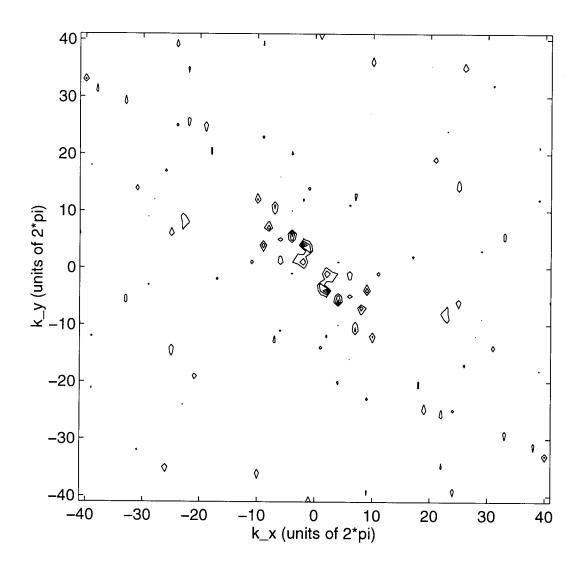
Figure 3.27: The power spectrum, P_y, of the y-component of the momentum field of System **IV**.
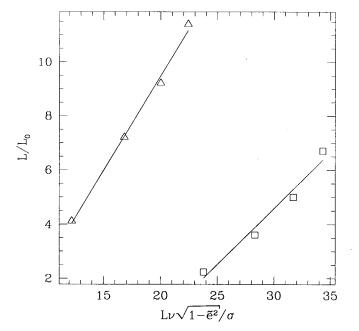
Figure 3.28: The dominant length scale L_0/L (where L is the linear dimension of the system) in the density field as a function of $L\bar{\nu}\sqrt{1 - \tilde{e}^2}/\sigma$ at fixed $\nu = 0.05$ (corresponding to $\triangle$) and $\nu = 0.1$ (corresponding to $\square$). The number of particles in the system is 20000.

due to the compressive and stretching effects of the shear.

We found in Chapter 2 that for a given value of $\tilde{e}$, an unforced system forms clusters of typical separation L_0 given by

$$L_0 \approx \frac{l}{\sqrt{1 - \tilde{e}^2}} \qquad (3.18)$$

where l is the mean free path in the corresponding homogeneous system. Our shear flow simulations indicate that this basic length scale is also relevant to sheared systems as well. We find that the reciprocal of the magnitude of the dominant wavevector, proportional to the typical separation between diagonal layers, varies as prescribed by (3.18) (provided that the system remains relatively dilute). Fig. 3.28 shows the results of a series of simulations with different $\tilde{e}$ values and two values of the homogeneous solid fraction, $\bar{\nu}$, equal to 0.05 and 0.10, the other parameters being held fixed. It is seen that for a given value of $\bar{\nu}$, which is equivalent to a given value of l, the dominant scale as determined from the spectral analysis varies linearly with L_0. A different slope is obtained when $\bar{\nu}$ changes. Fig. 3.29 plots the data from two-
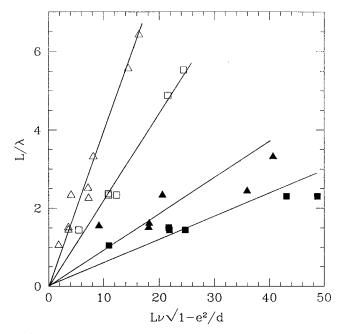
Figure 3.29: Results of two-dimensional simple shear flow simulations presented originally in Ref. [40] but organized here using (3.18). Here L is the linear dimension of the flow; d is the particle diameter and λ is the dominant length scale observed in the density field. The data points $\triangle$, $\square$, $\triangle$, and $\square$ correspond respectively to $\nu = 0.1, 0.3, 0.5, 0.6$. The straight lines are drawn through the data points to guide the eye.

dimensional simulations of simple shear flows obtained by Hopkins and Louge[40]. The data were originally organized in terms of the nondimensional length λ/d, where d is the particle diameter (notation used in Ref. [40]) and λ is the dominant scale obtained by Fourier analyzing the density field. In Fig. 3.29 we have used the new parameter combinations L/λ and $L\nu\sqrt{1 - \tilde{e}^{\,2}}/d$ as ordinate and abscissa respectively (where L is the linear dimension of the system) to organize the data from Ref. [40]. Thus it is seen that the dominant scales observed numerically by Hopkins and Louge indeed depend on $\tilde{e}$ and ν as prescribed by (3.18). Hence we believe that while some of the details are different for a sheared system, the basic mechanism responsible for clustering in freely decaying flows as expounded in Chapter 2 applies to shear flows as well.

3.2.2 The Distribution of Impact Parameters

The impact parameter, b, is a property of the collision between two particles and is defined as

$$b \equiv \sigma \frac{|\mathbf{k} \times \mathbf{v}_{12}|}{|\mathbf{v}_{21}|} \tag{3.19}$$

where $\mathbf{k}$ and $\mathbf{v}_{12}$ are defined following (1.2). The distribution of impact parameters is an important two-particle statistical characteristic, since it reveals, among other things, the degree of anisotropy in the microsopic dynamics. It may also be relevant to the construction of an accurate approximation to the two-particle distribution function[16]. We have seen in Section 2.3 that the statistics of the impact parameters in a highly inelastic unforced system indicated that particles within a cluster undergo mostly grazing collisions as a result of their coordinated collective motion. For simple shear flows, we assume that the impact parameter distribution, $\beta(b; \rho(\mathbf{r}))$, depends on $\mathbf{r}$ only through the density $\rho(\mathbf{r})$. Thus we collect statistics in cells whose density lie in a small window around ρ. Fig. 3.30 shows that $\beta(b; \rho)$ as a function of b at fixed ρ is essentially uniform for all values of b. This uniformity is observed over a large range of density values and values of $\tilde{e}$. We believe the uniformity follows from the fact that in a sheared system the energy replenishing mechanism, i.e. the heating due to the shear, causes sufficient disorder on the scale of the particle's size to render $\beta(b; \rho)$ quite homogeneous.

We note that $\beta(b; \rho)$ for a fixed ρ, though largely uniform, is by no means entirely devoid of structure. Since it is difficult to discern this structure in Fig. 3.30, we use a cumulative sampling technique similar in spirit to the one used in Chapter 5 for the single-particle distribution function to accurately measure $\beta(b; \rho)$. This technique involves accumulating the distribution and then fitting the result to a smooth function. Assuming that $\beta(b; \rho)$ is normalized in the usual way, i.e.

$$\int_{b=0}^{\sigma} \beta(b; \rho) \mathrm{d}b = 1 \tag{3.20}$$

and that the cumulative distribution $\mathcal{B}(b; \rho)$ is defined as

$$\mathcal{B}(b; \rho) \equiv \int_{b'=0}^{b'=b} \beta(b'; \rho) \mathrm{d}b' \tag{3.21}$$
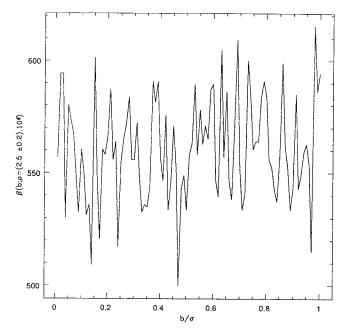
Figure 3.30: The distribution of impact parameters $\beta(b; \rho)$ for a given density window in System **III**.

then the fit in this case is simply a straight line passing through the origin with slope equal to $1/\sigma$. Subtracting this straight-line fit from $\mathcal{B}(b; \rho)$, we obtain the result shown in Fig. 3.31. The graph shown corresponds to a density window that lies above the average density in the system. From Fig. 3.31, it can be deduced that there is a small surplus of collisions whose impact parameters are close to σ (corresponding to near-grazing collisions) and a deficit of collisions whose impact parameters are close to 0 (corresponding to head-on collisions). This trend appears to persist over a large range of density values. The size of the surplus or deficit in all cases is less than 1% of the average value of the probability density.

The largely uniform impact parameter distribution in a simply sheared system contrasts sharply with the impact parameter distribution in an unforced system (cf. Fig. 2.16). The latter distribution contains a sharp peak at the maximally allowed value, viz. the diameter of the disk, indicating that the majority of collisions in the system are grazing collisions. This fact is clearly due to the coherent motion of the clusters whose constituent particles have approximately the same velocities. Since a grazing collision dissipates the least energy (as opposed to a head-on collision, which dissipates the most energy) it is evident that the absence of an energy replenishing
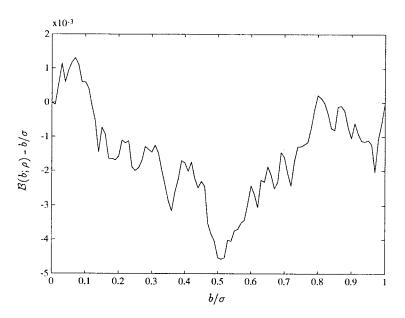
Figure 3.31: The difference between the cumulative distribution of impact parameters $\mathcal{B}(b; \rho)$ and b/σ as a function of b/σ. The data are taken from System **III** from a given density window.

mechanism causes the system to organize in a way that minimizes dissipation. In the sheared system, the tendency for more grazing collisions to occur still remains, but the forcing creates sufficient disorder to almost completely mask this effect.

3.2.3 The Distribution of Free Paths before Collision

The probability distribution of free paths before collision, $P(\mathbf{l}, v; \mathbf{r})$, is defined as the probability density of finding a particle, prior to its collision at the point $\mathbf{r}$ with another particle, to have traveled along the path $\mathbf{l}$ with speed $v = |\mathbf{v}|$ from the point of its previous collision. We make the simplifying assumption that the free path distribution depends on $\mathbf{r}$ only through the density, $\rho(\mathbf{r})$. We define the following function:

$$\tilde{P}(l, \alpha; v, \rho_0) \equiv \frac{1}{\Omega_{\rho_0}} \int_{\rho = \rho_0} P(l, \alpha; v, \rho(\mathbf{r})) \mathrm{d}\mathbf{r}. \tag{3.22}$$

where we have used polar coordinates (l, α) for $\mathbf{l}$; the integration is taken over all cells in the system whose density is ρ_0, and Ω_{ρ_0} is the total area (volume) of these cells.
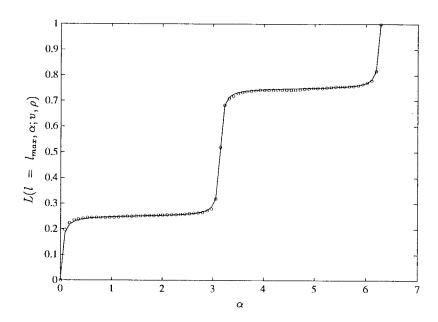
Figure 3.32: The graph of the angular part of $L(l, \alpha; v, \rho)$, corresponding to the function $L(l = l_{max}, \alpha; v, \rho)$, as a function of α. The data are obtained from System **III** from a given density window, and the solid curve through the data points is a fit with an optimal value of α_0 that minimizes that the error in the fit.

We further define a cumulative distribution based on (3.22):

$$L(l, \alpha; v, \rho) \equiv \int_{l' < l} \int_{\alpha' < \alpha} \tilde{P}(l', \alpha'; v, \rho) dl' d\alpha'. \tag{3.23}$$

Using a sampling technique similar to that used for determining the impact parameter distribution, we found from our simulations that the cumulative distribution has the following form:

$$L(l, \alpha; v, \rho) \simeq \left\{ \frac{1}{2\pi} \left[\tan^{-1} \left(\frac{\alpha}{\alpha_0} \right) + \tan^{-1} \left(\frac{\alpha - \pi}{\alpha_0} \right) + \tan^{-1} \left(\frac{\alpha - 2\pi}{\alpha_0} \right) \right] \right\}$$
$$\times \quad \mathrm{erf} \left(\sqrt{\frac{l}{\bar{l}(v, \alpha)}} \right). \tag{3.24}$$

where erf is the error function; α_0 is a constant independent of both l and v, and the factor $1/2\pi$ normalizes the distribution so that $L(l = l_{max}, \alpha = 2\pi; v, \rho) = 1$ (where l_{max} is the length of the longest free path in the domain). A plot of the angular part of $L(l, \alpha; v, \rho)$, corresponding to the function enclosed in braces in (3.24), is shown in Fig. 3.32. This plot may be understood as follows: granular systems are highly compressible and are characterized by high Mach numbers, i.e. the 'thermal' or fluctuating velocities in the system are much smaller than the typical macroscopic velocities. Since the mean (i.e. non-fluctuating) component of the particle's y velocity is zero, the displacement along the y direction between collisions will be small compared to the corresponding displacement along the x direction, which is determined by an externally imposed shear with relatively large characteristic velocities. Hence the free paths are mostly parallel to the streamwise direction, i.e. they are concentrated around angles of 0 and π relative to this direction. A plot of $L(l, \alpha; v, \rho)$ as a function of l for a fixed value of α is shown in Fig. 3.33. It is found that $\bar{l}(v, \alpha)$ appearing in the argument of the error function in (3.24) depends only weakly on α and v. This dependence can be dropped without affecting the accuracy of the fit. Hence we find to a good degree of approximation that

$$\tilde{P}(l, \alpha; v, \rho_0) = \frac{1}{2\alpha_0\sqrt{\pi}} \left[\frac{1}{1 + \left(\frac{\alpha}{\alpha_0} \right)^2} + \frac{1}{1 + \left(\frac{\alpha-\pi}{\alpha_0} \right)^2} + \frac{1}{1 + \left(\frac{\alpha-2\pi}{\alpha_0} \right)^2} \right]$$
$$\times \quad \sqrt{\frac{l_0}{l}} \exp \left(\frac{l}{l_0} \right) \tag{3.25}$$

where l_0 is a characteristic cross-over length independent of l, v and α whose meaning will be made clear below. If we focus on the distribution, $\mathcal{P}(l)$ of the magnitude l of the free path without regard to angle, we find that

$$\begin{aligned}
\mathcal{P}(l) &= \int_{\alpha'=0}^{2\pi} \tilde{P}(l, \alpha'; v, \rho) d\alpha' \\
&= \sqrt{\frac{\pi l_0}{l}} \exp\left(\frac{l}{l_0}\right)
\end{aligned} \tag{3.26}$$

This distribution is different in the low l limit from the distribution that is derived from the (conventional) assumption that the probability of a particle colliding after traveling freely for a distance l is independent of l. This assumption implies that $\mathcal{P}(l)$ should decay exponentially in l for all l. Heuristically, the explanation for (3.26) is that for short l, the particle samples a small volume whose typical density may be very large (larger than the average density) because of density fluctuations. Hence the probability of the particle colliding in such a small volume, or, equivalently, the probability for short l, is larger than the value given by the exponential. Our numerical simulations of dilute *elastic* gases indicate that (3.26) *holds for these gases as well.*

To derive (3.26), we first note that the average solid fraction, $\bar{\nu}$, is given by

$$\bar{\nu} \sim \bar{n}\sigma^2 \tag{3.27}$$

where $\bar{n} \equiv N/A$ is the average number density for N disks in a system of total area A, and σ is the linear dimension of a disk. The probability of finding a particle in a box of size σ is the ratio of the number of particles to the number of boxes, i.e. $N/(A/\sigma^2) \approx \bar{\nu}$. Thus the probability of finding no particle in a rectangle of length l and width σ is $(1-\bar{\nu})^{l/\sigma}$. When the rectangle is small, the fluctuations in the number of particles in it are large. If $\bar{m}$ is the number of particles in such a rectangle, then

$$\bar{m} = \bar{n}l\sigma = \bar{\nu}\frac{l}{\sigma} \tag{3.28}$$

and a typical fluctuation in $\bar{m}$ is

$$\delta m_t \sim \sqrt{\bar{m}} = \sqrt{\bar{\nu}\frac{l}{\sigma}}. \tag{3.29}$$
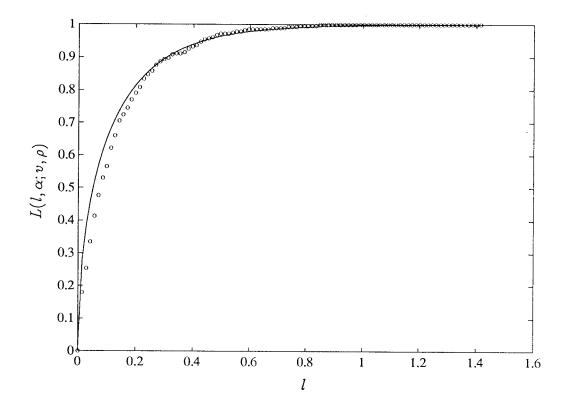
Figure 3.33: The graph of $L(l, \alpha; v, \rho)$ as a function of l at a fixed value of α. The data are obtained from System **III** from a given density window, and the solid curve through the data points is the function $\text{erf}(\sqrt{l/\bar{l}})$ with an optimal value of $\bar{l}$ that minimizes the error in the fit.

Since $\delta m_t \gg \bar{m}$ when $\bar{\nu} l/\sigma \ll 1$, the typical solid fraction that the particle samples when l is small is

$$\nu_t \sim \frac{\delta m_t \sigma^2}{l\sigma} = \sqrt{\frac{\bar{\nu}\sigma}{l}} \qquad (3.30)$$

The condition $\bar{\nu} l/\sigma \ll 1$ can also be cast as $l \ll l_0$, where $l_0 \equiv \sigma/\bar{\nu}$ is the mean free path. Under this condition, the probability of finding no particles in a box of length l is

$$(1 - \nu_t)^{l/\sigma} = \left(1 - \sqrt{\frac{\bar{\nu}\sigma}{l}}\right)^{l/\sigma} \approx \exp\left(-\sqrt{\frac{l}{l_0}}\right) \qquad (3.31)$$

Hence the probability that the free path is larger than l is

$$\mathcal{P}(\text{free path} > l) \sim \exp\left(-\sqrt{\frac{l}{l_0}}\right) \qquad l \ll l_0 \qquad (3.32)$$

and the corresponding probability density for l is

$$P(\text{free path} = l) = \frac{\partial}{\partial l}[1 - \mathcal{P}(\text{free path} > l)]$$
$$\sim \frac{1}{\sqrt{l_0 l}} \qquad l \ll l_0 \qquad (3.33)$$

When $l \gg l_0$, the fluctuations in density are negligible, and hence $\nu \approx \bar{\nu}$, in which case,

$$\mathcal{P}(\text{free path} > l) \sim (1 - \bar{\nu})^{l/\sigma} \approx \exp\left(-\frac{l}{l_0}\right) \qquad l \gg l_0 \qquad (3.34)$$

and the corresponding probability density for l is

$$P(\text{free path} = l) \sim \frac{1}{l_0} \exp\left(-\frac{l}{l_0}\right) \qquad l \gg l_0. \qquad (3.35)$$

Notice that (3.33) and (3.35) matches at $l = l_0$. Hence the asymptotically matched expression for the probability density over the entire range for l is given, up to normalization, by

$$P(\text{free path} = l) \sim \frac{1}{\sqrt{l}} \exp\left(-\frac{l}{l_0}\right) \qquad (3.36)$$

in agreement with (3.25).

3.3 Summary

The numerical simulations of simple shear flows presented in this chapter show that a stripwise clustering microstructure may arise when the mean flow is non-transient. This microstructure, which is only one of the several types of microstructures observed in simple shear flows, consists of elongated clusters organized into strips with a prefered orientation along the extensional axis of the shear. It is created by means of a transient linear instability and two nonlinear processes, viz. a clustering instability and a strongly nonlinear cluster scattering process. The scattering of clusters into each other is driven by convection due to the shear, while the clustering instability causes particles temporarily dispersed by the scattering to reaggregate to form new clusters. Thus clusters are continually destroyed and recreated in the flow, leading to a highly time-dependent microstructure. The stability properties of simple shear flows relevant to clustering are examined in more detail in Chapter 4. A spectral analysis shows that for a given value of the coefficient of restitution, $\tilde{e}$, the dominant spatial scale, L_0, corresponding to the separation between clusters, is given by (1.1), in accord with the results of Chapter 2 for free systems. This result, together with numerical observations presented in this chapter, provides the basis for our belief that the underlying clustering mechanism for both free and sheared systems are the same.

Chapter 4

Instability and Multistability in Granular Shear Flows

In this chapter we show that the time scale for the clustering process in a sheared system is inversely proportional to the average granular temperature in the system. The degree of clustering (as measured by, say, the amount of inhomogeneity in the flow) depends significantly on the rate of this process relative to those of competing processes such as diffusion and convection. Consequently, a sheared system in which the granular temperature is relatively high (e.g. one prepared in an initial state whose average granular temperature is much higher than that in the statistically steady state to which the system evolves eventually) exhibits a markedly different dynamics from one in which the temperature is low, all other externally imposed parameters for the two systems being the same. This is one of the sources of hysteretic behavior in granular systems. It leads to the existence of multiple steady states which correspond to the same external parameters but which are characterized by very different microstructures. To explain the hysteretic behavior, we first perform a linear stability analysis of simple shear flows which shows that such flows are transiently unstable. Then we show that the transiently growing modes initiate nonlinear growth that leads to clustering. We examine the various time scales characterizing the dynamics of fluctuations, paying particular attention to the dependence of these scales on the initial condition and also to the way they determine the ultimate, long-time fate of

113

the system. The results of numerical simulations are then used to demonstrate the variance of the steady state with respect to the initial conditions and the application of transient forces. Finally, other possible mechanisms for multistability are briefly discussed.

4.1 Transient Linear Instability of Shear Flows

We have seen in earlier chapters that the continuum equations for granular flows derived using kinetic theory have been moderately successful in explaining results of numerical simulations, although they fall short in respects having to do with the fact that microstructures (i.e. strong inhomogeneities) were not taken into account in their derivation. It seems that these equations can nonetheless by used successfully for the analysis of the dynamics of microstuctures in nearly elastic and nearly homogeneous systems. A stability analysis of these equations for the case of an unforced system presented in Chapter 2 reveals that homogeneous solutions exist but are are unstable to infinitesimal inhomogeneous perturbations. The analysis also shows that a nonlinear instability is responsible for the clustering process. Shear flows in both two- and three-dimensions, unlike unforced flows, are linearly stable, though some eigenmodes may grow for a finite time before reverting to temporal decay. This transient instability was found to exist in homogeneous states in which the velocity profile is linear[48, 49, 50], and it is expected that a similar phenomenon exists in more complex setups as well. The stability analyses show that the orientation of the wavevector that correspond to the (transiently) most unstable mode coincides approximately with the extensional axis of the shear. This mode corresponds to disturbances in real space that are parallel to the compressional axis of the shear, ie. at 135 degrees from the streamwise direction. Note that the microstructure in the *nontransient* state has a prefered orientation in real space along the 45 degrees direction, contrary to what one may expect from the transient stability analysis. It turns out that the next transiently most unstable mode corresponds to disturbances in real space that lie along the 45 degrees direction. At early times, disturbances grow in both directions until the nonlinear instability takes over, accenting the growth along

the 45 degrees direction and and suppressing the growth in the 135 degrees direction. Our analysis and numerical results to be presented in this chapter corroborate this picture of the dynamics.

A plot of the particle configuration in a typical simple shear flow is shown in Fig. 4.5. The flow is statistically stationary and contains a stripwise clustering microstructure whose features have been studied in detail in Chapter 3. The mechanism responsible for the emergence of clusters in this system can be elucidated by considering the linear stability of the equations derived using kinetic theory in [51] for two-dimensional flows of monodisperse inelastic disks. In the low-density limit, which is the regime we are considering, these equations read:

$$
\nu \left(\dot{T} + v_i \partial_i T \right) = \frac{\sqrt{\pi}}{2} \sigma \partial_i \left(\sqrt{T} \partial_i T \right) - \nu T \partial_i v_i
$$
$$
+ \frac{\sqrt{\pi}}{16} \sigma \sqrt{T} \, \mathrm{Tr} \hat{D}_{ij}^2 - \frac{8}{\sqrt{\pi}} \frac{\nu^2}{\sigma} \epsilon T^{3/2} \tag{4.1}
$$
$$
\nu \left(\dot{v}_j + v_i \partial_i v_j \right) = -\partial_j \left(\nu T \right)
$$
$$
+ \frac{\sqrt{\pi}}{8} \sigma \left(\partial_i \sqrt{T} \right) \left(\partial_i v_j + \partial_j v_i - \delta_{ij} \partial_l v_l \right)
$$
$$
+ \frac{\sqrt{\pi}}{8} \sigma \sqrt{T} \Delta v_j \tag{4.2}
$$
$$
\dot{\nu} = -\partial_i \left(\nu v_i \right) \tag{4.3}
$$

where T is the granular temperature and ν is the volume (area) fraction of the particles (i.e. reduced density) which equals ρ/ρ_s where ρ is the density and ρ_s is the mass density of a solid particle; σ is the diameter of a particle and ∂_i denotes $\partial/\partial r_i$, where $i = 1, 2$ indicates the Cartesian components of the position vector $\mathbf{r}$. The summation convention for repeated indices is assumed. The coefficient of restitution, $\tilde{e}$, appears in $\epsilon \equiv 1 - \tilde{e}^2$, and $\mathrm{Tr} \hat{D}_{ij}^2$ is the viscous heating function given by

$$
\mathrm{Tr} \hat{D}_{ij}^2 = 2 \left[(\partial_j v_i)(\partial_i v_j) + (\partial_j v_i)^2 - (\partial_l v_l)^2 \right]. \tag{4.4}
$$

Equations (4.1)-(4.3) admit a basic solution with constant volume fraction ν_0, constant temperature T_0 and a velocity field $\mathbf{v} = (\gamma y, 0)$. The value of T_0 is determined by the balance between the rate of input of energy through viscous heating and the rate of loss of energy through inelastic collisions. This balance is between the third

and fourth terms on the r.h.s of (4.1), and it yields

$$T_0 = \frac{l^2 \gamma^2}{\pi \epsilon} \tag{4.5}$$

where $l \equiv \pi \sigma / 8 \nu_0$ is the mean free path in the basic state.

The linear stability of shear flows governed by equations derived from kinetic theory, which are similar to (4.1)-(4.3), has been investigated before[48, 49, 50]. In Refs. [49, 50], the linearized equations are analyzed by first transforming them to coordinates which travel with the local mean flow and then by performing a Fourier transform of the resulting equations. This procedure eliminates the coordinate-dependent convective terms in the original linearized equations, at the price of defining modes in terms of time-dependent wavevectors which are continually rotated by the mean shear. The resulting equations are not self-adjoint. Disturbances evolving from $t = 0$ are found to grow for short times (the growth rates depending on the nature of the variables used in the analysis, a point discussed in [53]) and then decay. An elaborate analysis presented in [48] shows rigorously that simple shear flow is asymptotically linearly stable, though there can be transient growth of infinitesimal disturbances. Here we consider the transient evolution of infinitesimal disturbances of the basic state for times which are short enough for the effect of convection to be negligible. It is easy to see that the typical convective time scale is

$$\tau_c \sim 1/\gamma. \tag{4.6}$$

For times much shorter than τ_c, fluid elements in the system may be considered to be unaffected by the mean flow and hence the convective terms in the equations may be dropped to a good degree of approximation.

In the following, it is convenient to nondimensionalize (4.1)-(4.3) by defining

$$\tilde{\mathbf{r}} = \frac{\mathbf{r}}{L} \tag{4.7}$$

$$\tilde{t} = \gamma t \tag{4.8}$$

$$\tilde{T} = \frac{T}{T_0} \tag{4.9}$$

$$\tilde{\mathbf{v}} = \frac{\mathbf{v}}{U} \tag{4.10}$$

$$\tilde{\nu} = \frac{\nu}{\nu_0}. \tag{4.11}$$

It is also convenient to introduce the dimensionless quantity

$$\delta^* \equiv \frac{l}{L\sqrt{\epsilon}} \tag{4.12}$$

which, as shown below, corresponds to the ratio of the typical separation between clusters to the linear dimension of the system. The infinitesimal disturbances $\delta\tilde{T}$, $\delta\tilde{\nu}$, $\delta\tilde{\mathbf{v}}$ of the basic state are defined by

$$\tilde{T} = 1 + \delta\tilde{T} \tag{4.13}$$

$$\tilde{\nu} = 1 + \delta\tilde{\nu} \tag{4.14}$$

$$\tilde{\mathbf{v}} = \tilde{y}\hat{\mathbf{x}} + \delta\tilde{\mathbf{v}}. \tag{4.15}$$

Linearizing (4.1)-(4.3) in the disturbances and dropping the convective terms, we obtain

$$\dot{\delta T} = -\text{div}\delta\mathbf{v} - 2\sqrt{\epsilon}\delta\nu - \sqrt{\epsilon}\delta T + 2\sqrt{\epsilon}(\partial_1\delta v_2 + \partial_2\delta v_1) + \frac{4\sqrt{\epsilon}\delta^{*2}}{\pi}\Delta\delta T \tag{4.16}$$

$$\dot{\delta v_j} = -\delta^{*2}(\partial_j\delta\nu + \partial_j\delta T) + \frac{\sqrt{\epsilon}\delta^{*2}}{2\pi}(\delta_{j1}\partial_2\delta T + \delta_{j2}\partial_1\delta T) + \frac{\sqrt{\epsilon}}{\pi}\delta^{*2}\Delta\delta v_j \tag{4.17}$$

$$\dot{\delta\nu} = \text{div}\delta\mathbf{v} \tag{4.18}$$

where δ_{j1} and δ_{j2} are Kronecker deltas, and the tildes on the disturbances have been dropped for notational convenience. Assuming eigenmodes of the form $\exp(i\mathbf{k}\cdot\tilde{\mathbf{r}} + s\tilde{t})$ where $\mathbf{k} = (k\cos\theta, k\sin\theta)$, and substituting (4.8)-(4.15) in (4.16)-(4.18), one obtains:

$$s\begin{pmatrix} \delta v_1 \\ \delta v_2 \\ \delta\nu \\ \delta T \end{pmatrix} = \begin{pmatrix} -\frac{\sqrt{\epsilon}}{\pi}\delta^{*2}k^2 & 0 \\ 0 & -\frac{\sqrt{\epsilon}}{\pi}\delta^{*2}k^2 \\ -ik\cos\theta & -ik\sin\theta \\ ik(2\sqrt{\epsilon}\sin\theta - \cos\theta) & ik(2\sqrt{\epsilon}\cos\theta - \sin\theta) \end{pmatrix}$$

$$\begin{pmatrix} -i\delta^{*2}k\cos\theta & ik\left(\frac{\sqrt{\epsilon}\delta^{*2}\sin\theta}{2\pi} - \delta^{*2}\cos\theta\right) \\ -i\delta^{*2}k\sin\theta & ik\left(\frac{\sqrt{\epsilon}\delta^{*2}\cos\theta}{2\pi} - \delta^{*2}\sin\theta\right) \\ 0 & 0 \\ -2\sqrt{\epsilon} & -\sqrt{\epsilon} - \frac{4}{\pi}\sqrt{\epsilon}\delta^{*2}k^2 \end{pmatrix}\begin{pmatrix} \delta v_1 \\ \delta v_2 \\ \delta\nu \\ \delta T \end{pmatrix}. \tag{4.19}$$

Let $\bar{\delta} \equiv \delta^*k$, which in dimensional units is equal to $(2\pi nl/L\sqrt{\epsilon})$ for the nth mode in **k**-space, and consider the limit $\bar{\delta} < 1$. In practice, this is usually the limit

of interest, since the dominant wavelengths L/n for relatively inelastic systems are found in the numerical simulations to be such that $\bar{\delta} < 1$. The characteristic equation corresponding to (4.19) is

$$
s^4 + \left(\sqrt{\epsilon} + \frac{6}{\pi} \bar{\delta}^2 \sqrt{\epsilon} \right) s^3 + \left\{ \bar{\delta}^2 \left[2 - \sqrt{\epsilon} \left(2 + \frac{1}{2\pi} \right) \sin 2\theta + \frac{3}{\pi} \epsilon \right] + \frac{9 \bar{\delta}^4 \epsilon}{\pi^2} \right\} s^2 +
$$
$$
\left\{ \bar{\delta}^2 \left[\frac{\epsilon \sin 2\theta}{\pi} - \sqrt{\epsilon} \right] + \bar{\delta}^4 \left[\frac{2\epsilon^{3/2}}{\pi^2} + \frac{6\sqrt{\epsilon}}{\pi} - \left(\frac{\epsilon}{2\pi^2} + \frac{\epsilon}{\pi} \right) \sin 2\theta \right] + \frac{4\epsilon^{3/2}}{\pi^3} \bar{\delta}^6 \right\} s +
$$
$$
\bar{\delta}^4 \left[\frac{2\epsilon^{3/2}}{\pi^2} \cos\theta \sin\theta + \frac{\bar{\delta}^4 \epsilon}{\pi} \left(1 - 2\sin^2 \theta \right)^2 - \frac{\bar{\delta}^4 \epsilon}{\pi} \right] + \frac{4 \bar{\delta}^6 \epsilon}{\pi^2} = 0 \quad (4.20)
$$

The full solution of (4.20) can be obtained numerically, and solutions for the largest positive root, s_m, for $\sqrt{\epsilon} = 0.8$ are shown in Fig. 4.1 and Fig. 4.2. These graphs show that for small values of $\bar{\delta}$, $\mathrm{Re}[s_m]$ is largest when $\theta = 3\pi/4$. For larger values of $\bar{\delta}$, a cross-over occurs and $\mathrm{Re}[s_m]$ becomes largest when $\theta = \pi/4$. The directions of maximal growth are interchanged again at still larger values of $\bar{\delta}$. The solution for s_m as a function of both $\sqrt{\epsilon}$ and $\bar{\delta}$ at fixed $\theta = 3\pi/4$ is shown in Fig. 4.3; and the solution for s_m as a function of both θ and $\bar{\delta}$ at fixed $\sqrt{\epsilon} = 0.8$ is shown in Fig. 4.4. A detailed numerical study of the solutions of (4.20) shows that $\mathrm{Re}[s_m]$ is positive in the range $0 < \bar{\delta} < 1$ for all values of $\sqrt{\epsilon}$ less than approximately $1/\pi$. The directions of maximal growth are also found to remain in either the $\theta = \pi/4$ or $\theta = 3\pi/4$ directions. The real parts of the other roots of (4.20) are either negative or much smaller in magnitude than $\mathrm{Re}[s_m]$.

For the case $\bar{\delta} \ll 1$, we may neglect terms in (4.20) of order $\bar{\delta}^3$ or higher to obtain

$$
s^4 + \left(\sqrt{\epsilon} + \frac{6}{\pi} \bar{\delta}^2 \sqrt{\epsilon} \right) s^3 + \bar{\delta}^2 \left[2 - \sqrt{\epsilon} \left(2 + \frac{1}{2\pi} \right) \sin 2\theta \right.
$$
$$
\left. + \frac{3}{\pi} \epsilon \right] s^2 + \bar{\delta}^2 \left(\frac{\epsilon \sin 2\theta}{\pi} - \sqrt{\epsilon} \right) s + \mathcal{O}(\bar{\delta}^3) \simeq 0 \quad (4.21)
$$

Equation (4.21) allows for a perturbative study of its solutions through which the stability properties of the problem can be made more transparent. Noting that one root of (4.21) is $s_1 = 0$, we seek solutions for the other roots as series in $\bar{\delta}^2$ and $\bar{\delta}$: $s_2 = \sum_{n=0}^{\infty} a_n \bar{\delta}^{2n}$ and $s_{3,4} = \sum_{n=1}^{\infty} b_n \bar{\delta}^n$. A substitution of the this ansatz into (4.21) yields the following solutions:

$$
s_2 = -\sqrt{\epsilon} + \left[\frac{3}{\sqrt{\epsilon}} - \frac{3\sqrt{\epsilon}}{\pi} - \left(2 + \frac{3}{2\pi} \right) \sin 2\theta \right] \bar{\delta}^2 + \mathcal{O}(\bar{\delta}^4)
$$
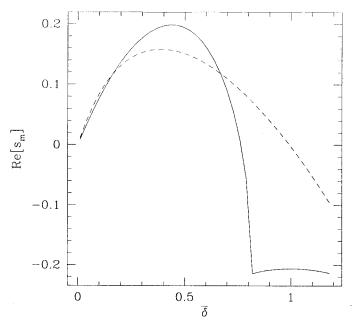
Figure 4.1: The real part of s_m as a function of $\sqrt{\bar{\delta}}$ at fixed $\theta = \pi/4$ (solid line) and $\theta = 3\pi/4$ (dotted line). The value of $\sqrt{\epsilon}$ is 0.8.
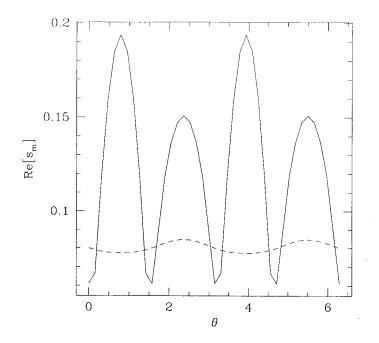
Figure 4.2: The real part of s_m as a function of θ for $\bar{\delta} = 0.5$ (solid line) and $\bar{\delta} = 0.1$ (dotted line). The value of $\sqrt{\epsilon}$ is 0.8.
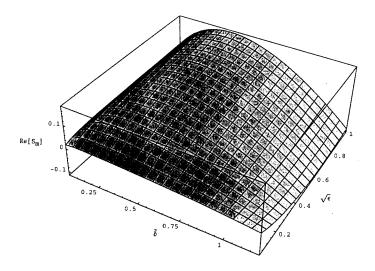
Figure 4.3: The real part of s_m as a function of $\sqrt{\epsilon}$ and $\bar{\delta}$ at fixed $\theta = 3\pi/4$.

$$\tag{4.22}$$

$$s_3 = \sqrt{1 - \frac{\sqrt{\epsilon}\sin 2\theta}{\pi}\,\bar{\delta}} + \mathcal{O}(\bar{\delta}^3) \tag{4.23}$$

$$s_4 = -\sqrt{1 - \frac{\sqrt{\epsilon}\sin 2\theta}{\pi}\,\bar{\delta}} + \mathcal{O}(\bar{\delta}^3) \tag{4.24}$$

For small values of $\bar{\delta}$, it is seen that the only growing mode corresponds to s_3 and that the maximal growth rate occurs in the $\theta = 3\pi/4$ direction. For long enough wavelengths, transient linear growth in real space is largest at 45 degrees from the streamwise direction; for intermediate wavelengths, the growth rate is largest at 135 degrees from the streamwise direction (note that the direction of the wavevector of a mode is at right angles to the direction of the strips of equal phase in real space).

4.2   Nonlinear Mechanism and Multistability

We next outline a nonlinear mechanism which is initiated by the transiently growing linear modes and which we believe is the mechanism leading to cluster formation in sheared systems. A large enough granular system, and therefore one having a large number of degrees of freedom, experiences statistical fluctuations of every macroscopic
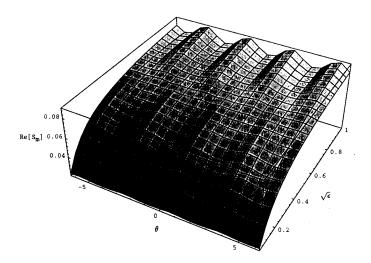
Figure 4.4: The real part of s_m as a function of θ and $\bar{\delta}$ at fixed $\sqrt{\epsilon} = 0.8$.

physical quantity except those that are strictly conserved. Consider a sheared hard-disk fluid at an 'initial' temperature T_i. Such a system may have a shear fluctuation of the form $\delta \mathbf{v} = (0, v_0 \sin kx)$, where k is consistent with periodic boundary conditions in a finite domain. Since equipartition is expected to hold during early times before the dynamics of the system becomes dominated by clustering, the typical amplitude v_0 of such a fluctuation can be estimated by computing the energy stored in the velocity field corresponding to this fluctuation and comparing the result to mT_i, which is the energy per degree of freedom (m is the mass of a particle). It is easy to show that the energy E_s stored in a single shear mode $\delta \mathbf{v} \equiv (0, v_0 \sin kx)$ is $E_s = \rho v_0^2 L^2$, where L is the linear dimension of the flow domain. Thus, $E_s \sim mT_i$ implies that $v_0 \sim \sqrt{T_i/N}$, where N is the total number of particles in the system, and therefore the typical magnitude of

$$h \equiv \partial \delta v_2 / \partial x \qquad (4.25)$$

is $h \sim k\sqrt{T_i/N}$. Let the value of k^{-1} correspond to the expected dominant length scale (i.e. the intercluster separation; see below). If we assume that k^{-1} is long enough so that diffusion effects can be neglected with respect to viscous heating and inelastic dissipation (an assumption to be verified *a posteriori*) then we can approximate (4.1)

by:

$$\nu\dot{T} \simeq \frac{\sqrt{\pi}}{16}\sigma\sqrt{T}\,\mathrm{Tr}\hat{D}_{ij}^2 - \frac{8}{\sqrt{\pi}}\frac{\nu^2}{\sigma}\epsilon T^{3/2}. \tag{4.26}$$

Note that we are still considering the dynamics of the system at early times when the effect of convection can be neglected. Consider firstly the case when the initial temperature T_i is so large that h is large compared to γ. This happens when T_i is much larger than T_0, the asymptotic value of the temperature given by (4.5) (the more precise statement of the condition is $T_i \gg \sqrt{N}T_0$). The viscous heating function in this case can be approximated as follows

$$\mathrm{Tr}\hat{D}_{ij}^2 = 2(\gamma + h)^2 \simeq 2h^2\left(1 + \frac{2\gamma}{h}\right) + \mathcal{O}\left(\frac{\gamma^2}{h^2}\right) \qquad h \gg \gamma. \tag{4.27}$$

Assuming that the density can be considered to be fixed in (4.26) and that the shear fluctuation is practically stationary with respect to the rate of decay of the temperature to its asymptotic value (assumptions again to be justified *a posteriori*), it can be shown that the solution to (4.26) is

$$T(t) = \frac{l^2h^2}{\pi\epsilon}A(t)\left[1 + \frac{2\gamma}{h}\right] + \mathcal{O}(\frac{\gamma^2}{h^2}) \tag{4.28}$$

where

$$A(t) = \left[\frac{1 - \alpha\exp(-\sqrt{\epsilon}ht)}{1 + \alpha\exp(-\sqrt{\epsilon}ht)}\right]^2 \tag{4.29}$$

and

$$\alpha \equiv \left[1 - \sqrt{T_i/(l^2h^2/\pi\epsilon)}\right] / \left[1 + \sqrt{T_i/(l^2h^2/\pi\epsilon)}\right]. \tag{4.30}$$

This solution is obtained using a series of substitutions similar to (2.41)-(2.44). The condition that the diffusion term in (4.1) can be neglected relative to, say, the inelastic dissipation term can easily be shown to be

$$kl < \sqrt{\epsilon} \tag{4.31}$$

The condition that diffusion is slow relative to the rate of saturation of $T(t)$ to its final value and that the shear fluctuation is quasi-stationary turns out also to be equivalent to (4.31). This result, already derived in Section 2.4.3 for free systems, is physically plausible since diffusion is important only at large k, and the shear fluctuation, being of hydrodynamic scale, can decay only by a diffusive (i.e. viscous) mechanism. When

$\gamma/h \ll 1$, the temperature rapidly saturates to the value dictated by the (local) velocity field corresponding to the shear fluctuation and a corresponding temperature gradient is formed in the system. As a result, a pressure gradient is established as well, its value being given by

$$P = \rho_s \nu T \simeq \rho_s \nu \frac{l^2 h^2}{\pi \epsilon} A(t). \tag{4.32}$$

Since $l = \pi\sigma/8\nu$, we have

$$P \sim \rho_s \sigma^2 h^2 / \epsilon \nu \tag{4.33}$$

i.e. the pressure that is established is inversely proportional to the density. Thus the pressure in dense regions is low relative to the pressure in dilute regions, causing mass to be transfered from the latter into the former. The excess of mass causes the dense regions to cool at a faster rate (since the collision rate there is increased), causing a further reduction in the values of the pressure in them and thus to a further mass flow into them. All in all, a small departure from a state of uniform density will generate an internal pressure difference that amplifies the departure, leading finally to the formation of high density clusters. For clustering to be possible, the mass must agglomerate at a faster rate than that of it being stretched apart by the mean shear, and fast enough to render diffusive processes inefficient. The time scale for mass motion leading to clustering can be estimated from the part of (4.2) which contains the pressure induced forces alone:

$$\rho\dot{\mathbf{v}} = -\nabla P. \tag{4.34}$$

Using (4.3), it follows that

$$\ddot{\rho} = \Delta P \tag{4.35}$$

and the time scale, τ_m, for mass motion is easily seen to be

$$\tau_m \sim \frac{1}{k}\sqrt{\frac{\rho}{P}} \sim \frac{\sqrt{\epsilon}}{klh}. \tag{4.36}$$

The condition that τ_m be shorter than the convective time scale τ_c given by (4.6) is therefore: $(\gamma/h)\sqrt{\epsilon} < kl$. When this is combined with (4.31), we have

$$\sqrt{\epsilon}\frac{\gamma}{h} < kl < \sqrt{\epsilon} \tag{4.37}$$

Notice that h depends on T_i and hence its value can be made large enough so that $\gamma/h < 1$. Thus the condition (4.37) on k can be easily satisfied. In fact (4.37) also encompasses the assumption in the linear analysis that the mean flow may be considered static on the time scale for linear growth, since from (4.23) we have

$$1/s_3 \sim \sqrt{\epsilon}/kl\gamma \qquad (4.38)$$

and $1/s_3 < 1/\gamma$ implies that $kl > \sqrt{\epsilon}$. Since τ_m is shorter the larger the value of k (it takes less time for mass to move a distance k^{-1} the shorter the distance), the fastest and dominant clustering process will occur at the largest allowed value of k. Thus the clustering process occurs on the scale determined by $kl \sim \sqrt{\epsilon}$. Since mass accumulates at the minima of h (where the temperature is lowest), this scale corresponds to the typical separation between clusters in the flow.

The case $\gamma/h \gg 1$ (i.e. $T_i < T_0$) can be analyzed in a similar way and the corresponding conditions on k are

$$kl > \sqrt{\frac{\gamma}{h}}\sqrt{\epsilon} \qquad (4.39)$$

$$kl < \sqrt{\epsilon} \qquad (4.40)$$

Condition (4.39) follows from the requirement that the time scale τ_m' for mass motion, which in this case is given by

$$\tau_m' \sim \sqrt{\frac{\gamma}{h}}\frac{\sqrt{\epsilon}}{kl\gamma}, \qquad (4.41)$$

to be shorter than the convective time scale τ_c. It can be shown that (4.40) is simultaneously the condition for the quasistationarity of the shear mode relative to the local dissipative processes and the condition for neglecting the diffusion term in (4.1). Clearly (4.39) and (4.40) cannot be satisfied simultaneously, and thus no clustering is possible at early times. Indeed, in this case, numerical simulations reveal growing modes in both the 45 and 135 degrees directions in the density field during early times yet no clustering. In contrast, when $\gamma/h \ll 1$, the nonlinear instability sets in much before the linear modes have a chance to significantly grow in amplitude. The mass motion is so fast that large clusters are formed and they rapidly coalesce to form extended regions of high density, thus masking out the transient growth of the linear modes. For the case $\gamma/h \gg 1$, clustering is possible at later times when $T(t)$

increases to its asymptotic value, but mass that agglomerated is also quickly dispersed by convection. When this happens, the quantity $\sqrt{\gamma/h}$ is no longer arbitrarily large but takes an $\mathcal{O}(1)$ value which allows (4.39) and (4.40) to be satisfied simultaneously. This again implies a scale for the clustering process determined by $kl \sim \sqrt{\epsilon}$. The microstructure in this case (shown in Fig. 4.5) consists of moderately dense and interspersed clusters which are continually dispersed and recreated in the flow. The clusters also scatter continually into each other as they are being rotated and stretched by the mean shear, resulting in a highly time-dependent microstructure. It is noted that the stripwise organization of the clusters as shown in Fig. 4.5 persists despite the strong time-dependence. This organization is stabilized by a complex mechanism involving the interplay of mass agglomeration along the extensional axis of the shear, convective dispersion and cluster-cluster scattering, the details of which have been presented in Chapter 3.

To reprise, the two flow states shown in Fig. 4.5 and Fig. 4.6, which are reached by the system asymptotically after long times, correspond respectively to the case in which $T_i < T_0$ and that in which $T_i \gg T_0$. The flows shown will respectively be refered to as the 'quasihomogeneous' flow and the 'plugged' flow. The numerical simulations show that the dynamical history of a system that converges to the quasihomogeneous flow is significantly different from the history of one that converges to the plugged flow. In the former system, clusters appear uniformly and simultaneously throughout the system and are dispersed by convection and scattering on a time scale that is comparable to the time scale for the mass agglomeration that creates them. Since clusters are 'mass attractors' and two clusters close together will coalesce, the fact that the agglomeration time scale is comparable to the dispersive one ensures that a stronger clustering effect does not occur and that the system remains quasihomogeneous asymptotically. This is not the case for the plugged flow, since the initial mass agglomeration time scale, being inversely proportional to the square root of the transient temperature, is so fast that convection by the mean shear has no time to act on the clusters that are formed. Nevertheless, convection in this case plays a role at later times by gradually sweeping the clusters together and causing them to coalesce into extended regions of high density. Thus, we see that the history
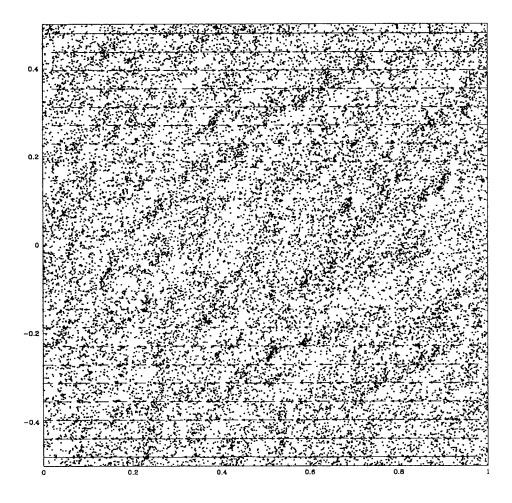
Figure 4.5: The particle configuration of a quasihomogeneous shear flow at steady state on which a vector plot of the velocity field is superposed. The parameters characterizing the flow are: $\tilde{e} = 0.6$, $\nu_0 = 0.05$, $N = 20000$.
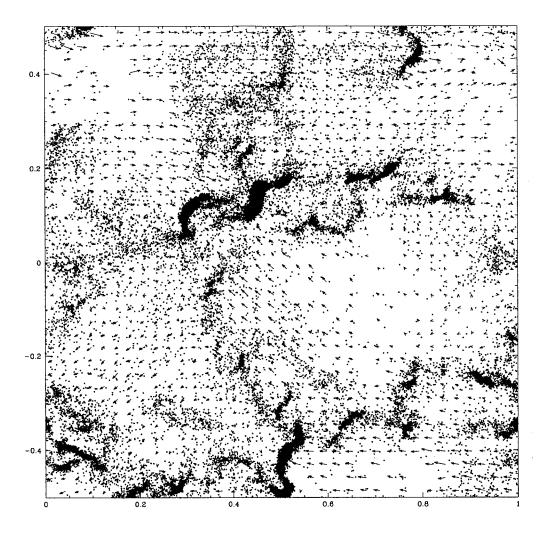
Figure 4.6: The particle configuration of a plugged shear flow at steady state on which a vector plot of the velocity field is superposed. The parameters characterizing the flow are the same as those of the flow shown in Fig. 4.5.

dependence or hysteresis in shear flows arises because of the dependence of the time scale for mass agglomeration on the transient temperature. When this time scale is short, most of the mass of the system becomes rapidly entrapped in clusters, leaving a very dilute and voluminous ambient that has little further dynamical effect. The subsequent dynamics of the system becomes dominated by the dense clusters that are formed. When the time scale for mass agglomeration is comparable to those of the convection and diffusion, the latter processes continually rehomogenize the flow and all three processes competitively determine the dynamics of the system, rendering it quasihomogeneous but highly time-dependent.

4.3   Other Routes to Multistability

In addition to the 'quasihomogeneous' and 'plugged' flow states discussed above, a simple shear flow can exhibit yet another stable flow state that is characterized by the same set of external parameters. This state can be reached by changing the shear rate instantaneously or incrementally from one value to another; or by shearing the system from an initial condition corresponding to that of a regular gas in static equilibrium. The shear rate is changed by increasing or decreasing the velocity difference between the periodic images of the system adjacent to the top and bottom boundaries. A change in this difference introduces a velocity differential between the boundary and the interior of the system, thereby increasing the magnitude of the velocity gradient in regions near the boundaries. Note that reducing the velocity difference between the periodic images could also (temporarily) increase the magnitude of the velocity gradient. This increase causes the rate of viscous heating to increase as well, thus increasing the internal kinetic energy of the regions near the boundaries. The pressure is raised as a result, and mass is pushed towards the center of the system. As the velocity differential diffuses into the system, the heated regions increase in size, sweeping particles into two thick streamwise layers of elevated density at the edges of the heated region. These layers span the length of the system as shown in Fig. 4.7. The elevated density increases the rate of collisions in the layers, lowering their temperature and causing their pressure to drop even further, thus drawing even more

mass into them. The layers converge at the center of the system after some time as shown Fig. 4.8, creating a dense but still fluidized plug surrounded by extended, dilute and energetic regions on both sides. After its creation, the plug persists because of the macroscopic heat flux originating near the boundaries and directed towards the centerline, which maintains a persistent temperature gradient in the system. Measurements of the heat flux[16] show that the flux vectors near the boundaries mostly point towards the center of the system. These fluxes produce a steady flow whose energetics involves the diffusion of kinetic energy generated near the boundaries towards the centerline where most of the dissipation takes place.

We have discovered yet another route to multistable states in shear flows which involves the application of a transient periodic perturbation to the shear rate. The set-up consists of adding a small but finite sinusoidal perturbation (whose period is long relative to the average time between collisions of a particle) to the velocities of the periodic images of a system that has converged to a quasihomogeneous state. The perturbation is applied for several periods before they are switched off, resetting the shear rate to it original value. We found that for sufficiently strong perturbations, the system cannot 'recover' from the large changes in density that are induced near the boundaries by the perturbation and it lapses into a state that resembles the one shown in Fig. 4.8. A more detailed investigation of this set-up is given in Ref. [16].

4.4 Summary

We have shown that the uniform state of a dilute simple shear flow is transiently unstable and that the most unstable modes lie along the compressional and extensional axes of the shear. These modes initiate a nonlinear mechanism that leads to the formation of clusters whose typical separation is $l/\sqrt{\epsilon}$. The source of hysteresis in shear flows is explained in terms of competing time scales whose relative importance is determined by the character of the transients affecting the flow. Although we have demonstrated the hysterectic effect using the contrasting scenarios of extremely high and low temperatures for the initial state of the shear flow, one could use less artificial transients, such as those that are imposed externally, e.g. impulsive motion or
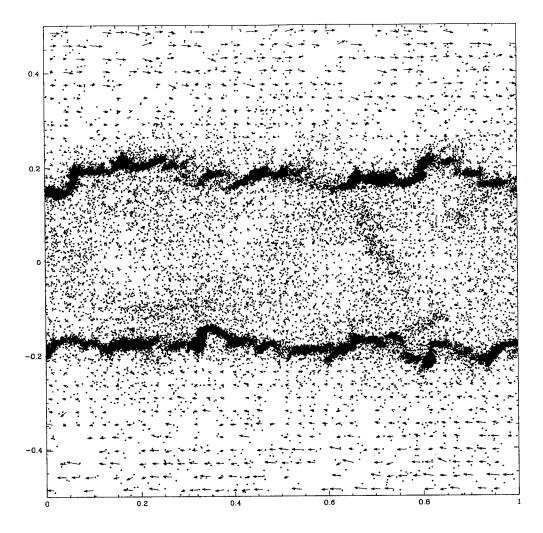
Figure 4.7: The particle configuration of an incrementally sheared system at an early time after the lapse of 20 collisions per particle following a static and homogeneous initial condition. The velocities of the periodic images are given by $U = \pm U_0 [1 - \exp(-t/\tau)]$ where U_0 is a constant and τ is a characteristic time chosen to be much longer than the collision time in the system. A vector plot of the velocity field is superposed. The parameters characterizing the system are the same as those of the system shown in Fig. 4.5.
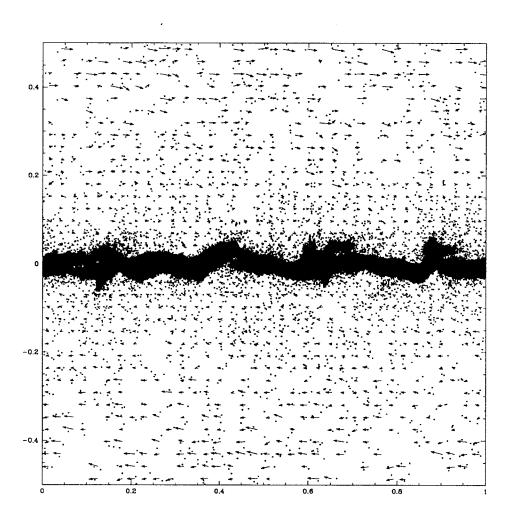
Figure 4.8: The particle configuration of the same incrementally sheared system as the one shown in Fig. 4.7 but after long times. A vector plot of the velocity field is superposed. The layers are seen to have converged to a plug in the center of the system.

rapid shear heating near a boundary, that could trigger the effect. Indeed it is found that a system incrementally sheared from a static configuration develops eventually into another stable flow state distinct from the ones produced by varying the initial temperature of the system.

Chapter 5

The Single-Particle Distribution Function for Granular Shear Flows

In this chapter we show that the single-particle velocity distribution function for a two-dimensional simple granular shear flow has the form of an exponential function of a second-order polynomial in the norm of the fluctuating velocities with angle-dependent coefficients. This form is markedly different from the Gaussian (with corrections taking into account the state of shear) or the generalized Gaussian distributions which have been used in kinetic theories of granular flows. In particular, it is nonanalytic in the Cartesian components of the fluctuating velocities. This result is obtained from molecular dynamics simulations involving hundreds of thousands of particles by means of a cumulative sampling algorithm which is effective in filtering the noise inherent in the numerical data. Less massive numerical simulations performed in the past cannot effectively be used to determine the distribution function because of the noise in the data and because small granular systems are qualitatively different from large ones. The cumulative sampling algorithm is separately applied to different ranges in the pertinent variables, such as the density and granular temperature, thus accounting for the fact that the flow is inhomogeneous. The implications of the form of the distribution function obtained on theories of granular flows are discussed.

5.1 Accurate Determination of the Distribution Function

A proper theoretical understanding of rapid granular flows requires the knowledge of the appropriate statistics, and in this respect the single-particle distribution function is an object of central importance. For dilute flows, this distribution function should be deduced from a Boltzmann-like equation which accounts for inelastic collisions (this equation is only 'slightly' different from the standard Botzmann equation). The solution of this equation is a nontrivial task, since detailed balance does not exist in the microscopic dynamics. The alternative is to study the single-particle distribution function in numerical experiments involving basic flow configurations (such as simple shearing). Despite its importance, this distribution function has not previously been accurately measured from numerical simulations. The reason for this seems to be that previous numerical studies of sheared systems (e.g. Ref. [44]) could not generate sufficient statistics to accurately deduce the distribution function. Under some rather restrictive assumptions, such as those of spatial homogeneity, isotropy and molecular chaos, a closed kinetic equation for this function was obtained and solved using a Monte-Carlo method[54]. The assumptions used in deriving the kinetic equation in Ref. [54] do not take into account the inhomogeneous nature of granular flows in general and the effects of microstructures in particular.

5.2 Cumulative Sampling Algorithm

Here we present a new algorithm that accurately determines the single-particle distribution function from data obtained in the simulations. This function will be denoted by $f_1(\mathbf{r}, \mathbf{v}; t)$, where $\mathbf{r}$ and $\mathbf{v}$ denote the position and fluctuating velocity respectively and t denotes the time. The algorithm is based on the observation that a monotonic integral of a noisy positive-definite quantity is comparatively less susceptible to distortion by noise and poor statistics than the quantity itself and may thus be fitted more readily to smooth functions. The relevant integral here is a cumulative distribution function, to be defined below, which corresponds to an integral of f_1.

This integral is constructed from data, then fitted to an appropriate smooth function which is then differentiated. The resulting function is still smooth and can be fitted again to a different functional form that is more convenient than the one used in the first fit. The second fit, though simpler, will be no less accurate since the noise in the data has already been eliminated with the first fit. Thus, the problem of noise in the data is overcome by a two-tier fitting procedure, and the problem of poor statistics, which can be serious in regimes of very low and very high $|\mathbf{v}|$, is alleviated by the use of a cumulative sampling technique. The quality of the statistics improves as more configurations ('snapshots' of the system) are used in determining f_1. The use of several configurations corresponding to different times is justified since the flow is statistically steady.

We assume that the shear flow is statistically stationary in time so that $f_1(\mathbf{r}, \mathbf{v}; t)$ is not an explicit function of time. It is well-known that the single particle distribution function can be represented as:

$$f_1(\mathbf{r}, \mathbf{v}) = \langle \sum_{i=1}^{N} \delta(\mathbf{r} - \mathbf{r}_i)\delta(\mathbf{v} - \mathbf{v}_i) \rangle \qquad (5.1)$$

where $\mathbf{r}_i$ and $\mathbf{v}_i$ are the position and velocity of the i-th particle and $\langle \cdots \rangle$ denotes an average over a statistical ensemble of systems characterized by the same parameters as the one of interest (in contrast to Section 1.4.3 in which $\langle \cdots \rangle$ denotes an average over particles in a cell). The function f_1 obeys the normalization

$$\int_{\mathbf{v}} f_1(\mathbf{r}, \mathbf{v})d\mathbf{v} = \langle \sum_{i=1}^{N} \delta(\mathbf{r} - \mathbf{r}_i) \rangle = \rho(\mathbf{r}) \qquad (5.2)$$

$$\int_{\mathbf{r}} \int_{\mathbf{v}} f_1(\mathbf{r}, \mathbf{v})d\mathbf{v}d\mathbf{r} = N \qquad (5.3)$$

where $\rho(\mathbf{r})$ is the number density; and the subscript $\mathbf{v}$ denotes integration over velocity and the subscript $\mathbf{r}$ denotes integration over the coordinates. Since the mean velocity field corresponds to linear shear, it is reasonable to assume that f_1 depends on the position $\mathbf{r}$ through the local density, $\rho(\mathbf{r})$, the local temperature, $T(\mathbf{r})$, and the local mean velocity, $\mathbf{V}(\mathbf{r})$. Also, f_1 should depend on $\mathbf{V}(\mathbf{r})$ through the difference $\mathbf{v} - \mathbf{V}(\mathbf{r})$. All in all, we assume that f_1 can be written as

$$f_1(\rho(\mathbf{r}), T(\mathbf{r}), \mathbf{v}) \equiv f^{(1)}(\rho(\mathbf{r}), T(\mathbf{r}), \mathbf{v} - \mathbf{V}(\mathbf{r})). \qquad (5.4)$$

Notice that $f^{(1)}$ is assumed not to depend *explicitly* on the gradients of the velocity, temperature and density fields. This does not imply that $f^{(1)}$ does not depend on these gradients; rather it is assumed that if in a statistically steady state of a specific system there is a one-to-one correspondence between the values of the fields and their gradients, then $f^{(1)}$ will depend implicitly on the latter. That is, if the density, temperature and fluctuating velocity in a coarse-graining cell are given, then their gradients within the cell are implied. Note also that the gradient of $V(r)$ is found to be highly uniform in the system (cf. Section 3.1.4). Hence we regard this gradient as a fixed parameter of the problem, viz. the shear rate γ. Our assumptions are justified *a posteriori* by numerical results obtained by applying the algorithm. We note also that $f^{(1)}$ depends on the parameters defining the system, though this dependence is not made explicit in (5.4) for the sake of notational simplicity.

Notice that the above assumptions does not imply a decoupling of the spatial and velocity distribution functions. On the contrary, since values of the density and temperature are taken to determine the values of their gradients, a strong correlation between the spatial and velocity distributions is implied. The physical basis for this lies in the particular structure of the statistically steady state of the shear flow which we are considering here: A point in the flow is inside either a cluster or a dilute region, or it is at the 'interface' between a cluster and the dilute region immediately surrounding it. In each case, the density and temperature are in one-to-one correspondence with the location of the point. Hence the values of the density and temperature determine the local gradients of these quantities.

It follows that $f^{(1)}$ can be determined, for given values of the density $\rho = \rho_0$ and temperature $T = T_0$, by collecting statistics in regions of the flow whose density and temperature are simultaneously ρ_0 and T_0 respectively. In practice, one has to define small windows in the density and temperature that are centered around predetermined values of these quantities so that statistically significant results can be obtained. Hence the sampling procedure consists of the following steps: (1) The system is divided into cells and the temperature and density in each cell is determined as explained in Section 1.4.3; (2) the cells whose temperature and density lie within the predetermined windows are identified; (3) a process of 'binning' the fluctuating

velocities of the particles in these cells, in terms of the norms and polar angles (relative to the streamwise direction) of these velocities, is performed (the fluctuating velocity is computed by subtracting the velocity of the particle from the average velocity of all particles in the cell in which the particle resides). The information obtained from the binning process is used as described below.

Let Ω_{ρ_0, T_0} denote the total area of the cells whose density lies within a window around ρ_0 and T_0 . Let $S(\rho_0, T_0)$ denote this set of cells. Also let $\hat{f}^{(1)}$ denote the numerical approximation to $f^{(1)}$ given by

$$\hat{f}^{(1)}(\rho_0, T_0, \mathbf{v} - \mathbf{V}(\mathbf{r})) \equiv \frac{1}{\Omega_{\rho_0, T_0}} \int_{S(\rho_0, T_0)} f^{(1)}(\rho(\mathbf{r}), T(\mathbf{r}), \mathbf{v} - \mathbf{V}(\mathbf{r})) d\mathbf{r} \quad (5.5)$$

$$= \left\langle \frac{1}{\Omega_{\rho_0, T_0}} \int_{S(\rho_0, T_0)} \sum_{i=1}^{N} \delta(\mathbf{r} - \mathbf{r}_i) \delta(\mathbf{v} - \mathbf{v}_i) d\mathbf{r} \right\rangle \quad (5.6)$$

$$= \left\langle \frac{1}{\Omega_{\rho_0, T_0}} \sum_{i \in S(\rho_0, T_0)} \delta(\mathbf{v} - \mathbf{v}_i) \right\rangle \quad (5.7)$$

where the integrals in (5.5) and (5.6) extend only over those cells whose values of the density and temperature are within the predefined windows around ρ_0 and T_0 respectively. The index i in (5.7) runs only over the particles in these cells. As mentioned, $\langle ... \rangle$ denotes an average over an ensemble of realizations; in practice it means averaging over a series of snapshots of the system. The volume Ω_{ρ_0, T_0} is included in the ensemble average because it may vary from one system to another in the ensemble. For notational simplicity, we drop the subscript 0 in ρ_0 and in T_0 and introduce $\rho \equiv N_{\rho, T} / \Omega_{\rho, T}$, where $N_{\rho, T}$ is the total number of particles in cells of density ρ and temperature T. For narrow enough windows it follows that:

$$\hat{f}^{(1)}(\rho, T, \mathbf{v} - \mathbf{V}(\mathbf{r})) = \rho \left\langle \frac{1}{N_{\rho, T}} \sum_{i} \delta(\mathbf{v} - \mathbf{v}_i) \right\rangle. \quad (5.8)$$

Let $\mathbf{v}'_i \equiv \mathbf{v}_i - \mathbf{V}(\mathbf{r}_i)$ denote the fluctuating component of the velocity of particle i. Then it is easy to see that $\hat{f}^{(1)}$ can be rewritten as follows:

$$\hat{f}^{(1)}(\rho, T, \mathbf{v}) = \rho \left\langle \frac{1}{N_{\rho, T}} \sum_{i} \delta(\mathbf{v} - \mathbf{v}'_i) \right\rangle. \quad (5.9)$$

The advantage of (5.9) is that it is not coordinate-dependent in an explicit way and as such it is convenient for demonstrating that the distribution function depends on the

thermodynamic parameters and local velocity fluctuations. We define the function

$$\tilde{f}^{(1)}(\rho, T, \mathbf{v}) \equiv \langle \frac{1}{N_{\rho,T}} \sum_i \delta(\mathbf{v} - \mathbf{v}'_i) \rangle \tag{5.10}$$

which is related to (5.9) in an obvious way. The cumulative distribution function for a two-dimensional system is defined by

$$h(v, \theta) \equiv \int_{v'=0}^{v} \int_{\theta'=0}^{\theta} \tilde{f}^{(1)}(v', \theta') v' dv' d\theta' \tag{5.11}$$

where we have used polar coordinates for $\mathbf{v}$, and the dependence on ρ and T is implicitly assumed for notational convenience. Clearly, $h(v, \theta)$ is proportional to the number of particles whose fluctuating velocity has a magnitude less than v and a direction between 0 and θ. Obtaining this quantity is merely a matter of counting. The normalization for $\tilde{f}^{(1)}$ is

$$\int_{v'=0}^{\infty} \int_{\theta'=0}^{2\pi} \tilde{f}^{(1)}(v', \theta') v' dv' d\theta' = 1 \tag{5.12}$$

and hence $h(\infty, 2\pi) = 1$. Two further observations may be made here: the derivative of $h(v, \theta)$ with respect to θ,

$$h_\theta(v, \theta) = \int_{v'=0}^{v} \tilde{f}^{(1)}(v', \theta) v' dv' \tag{5.13}$$

is periodic in θ since $\tilde{f}^{(1)}(v, \theta)$ is periodic in θ. Also, it is obvious that for small enough values of v, the function h_θ is given, to leading order in v, by $v^2 \times$ (function of θ). We make use of the first observation to write h_θ as a Fourier series:

$$h_\theta(v, \theta) = c_0(v) + \sum_{n \neq 0} c_n(v) \exp(in\theta). \tag{5.14}$$

Integration of (5.14) with respect to θ yields:

$$\begin{aligned} h(v, \theta) &= \int_{\theta'=0}^{\theta} h_{\theta'} d\theta' \\ &= \sum_{n \neq 0} \frac{i}{n} c_n(v) + c_0(v)\theta + \sum_{n \neq 0} c_n(v) \frac{\exp(in\theta)}{in}. \end{aligned} \tag{5.15}$$

Thus $h(v, \theta)$ may be expressed as a sum of terms that are independent of θ, a term that is linear in θ and terms that are periodic in θ. Notice that by (5.11), $h(v, 0) = 0$

and by eq. (5.15), $h(v, 2\pi) - h(v, 0) = h(v, 2\pi) = 2\pi c_0(v)$. It follows from (5.11) and (5.15) that the double derivative of h with respect to the angle θ and the velocity v can be expressed as follows:

$$h_{v\theta}(v, \theta) = v\tilde{f}^{(1)}(v, \theta) = \varphi_v(v) + \psi_{\theta v}(\theta, v) \tag{5.16}$$

where

$$\psi(\theta, v) \equiv \sum_{n \neq 0} c_n(v) \frac{\exp(in\theta)}{in} \tag{5.17}$$

$$\varphi(v) \equiv \frac{h(2\pi, v)}{2\pi} = c_0(v) \tag{5.18}$$

Once $h(v, \theta)$ is obtained from data (by counting as we said), $\varphi(v)$ may then be computed using (5.18), and $\psi(\theta, v)$ can be obtained from the identity

$$\psi(\theta, v) = h(v, \theta) - \frac{1}{2\pi} \int_{\theta=0}^{\theta=2\pi} h(v, \theta)d\theta + (\pi - \theta)\varphi(v) \tag{5.19}$$

which follows from (5.15) by using the fact that the average of the last term on its r.h.s. over the full range of angles vanishes. It is easy to check that ψ as given by (5.19) is periodic in θ as it should be.

We have found, on the basis of the data we obtained from the simulations, that the functions $\varphi(v)$ and $\psi(\theta, v)$ can be closely fitted by the functions $\varphi^*(v)$ and $\psi^*(\theta, v)$ respectively, where

$$\varphi^*(v) = \frac{1 - \exp(-J(v))}{2\pi} \tag{5.20}$$

$$\psi^*(v, \theta) = \sum_{p=1}^{4} A_p(v) \sin[2p(\theta + \beta)] \tag{5.21}$$

with

$$J(v) \equiv \sum_{m=2}^{4} a_m v^m \tag{5.22}$$

$$A_p(v) \equiv \alpha_p \{1 - \exp[-Q_p(v)]\} \tag{5.23}$$

$$Q_p(v) \equiv \sum_{m=2}^{6} d_{pm} v^m \tag{5.24}$$

where $J(v)$ is of quartic order in v, $Q_p(v)$ are polynomials of sixth order in v, and α_p is the asymptotic value of $A_p(v)$ for large v. The reason only even multiples of θ appear
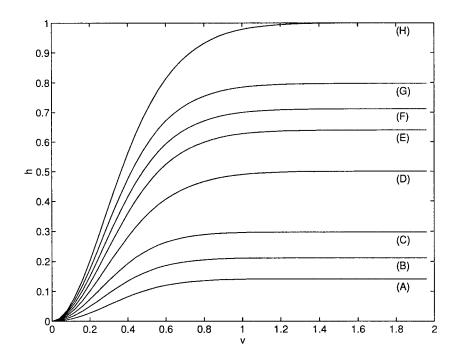
Figure 5.1: The cumulative distribution function $h(v, \theta)$ versus v for values of $\theta = n\pi/4$, $n = 1, 2, \cdots, 8$, corresponding to the curves (A) to (H) respectively. Notice that $h(v, \theta)$ is smooth and that it increases monotonically with v and θ. The data correspond to System **III** , and the windows in ρ and T are $(2.8 \pm 0.2) \times 10^5$/unit area and 0.11 ± 0.0075 respectively. The average temperature, $\overline{T}$, for the system is 0.15.
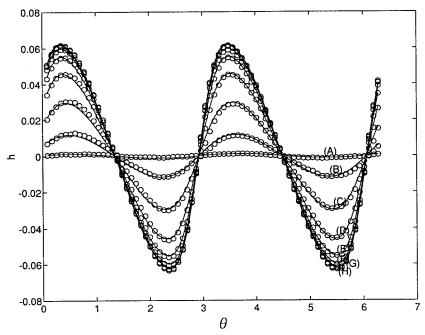
Figure 5.2: The periodic part, $\psi(v,\theta)$, of the function $h(v,\theta)$ shown in Fig. 5.1, versus θ for the values of v: 0.2, 0.4, 0.6, 0.8, 1.2, 2.0, corresponding to the sets of curves (A) to (F) respectively. The points correspond to the data and solid curves are given by (5.21). Notice that $\psi(v,\theta)$ crosses the θ axis at the same values of θ for different v .

in (5.21) is the 'rotation by π' symmetry obeyed by the shear flow. The expansions in (5.22) and (5.24) start with $m = 2$ since h_θ is proportional to v^2 for small values of v. The number of terms in the truncated sine series in (5.21) is determined by requiring the fit to be accurate to within 1% for large values of v and to within 5% for small values of v. The error tolerance level is relaxed for small values of v because the numerical data for these values tend to be noiser—a fact which is to be expected since the cumulative sampling technique used in the algorithm improves the statistics at moderate values of v but is not as effective for small v. For large v, the accuracy can be maintained since the numerical data tend to an asymptotic functional form.

The value of the phase β is found to depend on ρ, T, and $\tilde{e}$. Graphs of $h(v,\theta)$ versus v for several values of θ are shown in Fig. 5.1. A graph of $J(v)$ and its fit as given by (5.22) is shown in Fig. 5.3, and a graph of $\psi(v,\theta)$ along with its fit given by (5.21) is shown in Fig. 5.2. These graphs are derived from data taken from a time series of 20 configurations of System **III** sampled at times separated by intervals
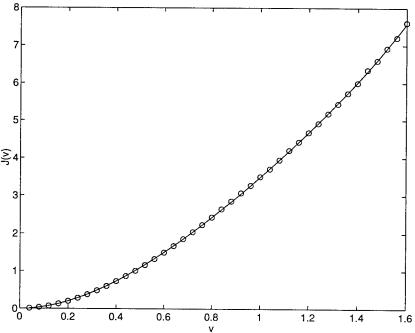
Figure 5.3: $J(v)$ (points) and its fit (solid line) given by (5.22). The cumulative distribution, $h(v, \theta)$, from which this graph is derived is shown in Fig. 5.1.

corresponding to the accumulation of one collision per particle in the system.

Next, a fit to $h_{v\theta}$ is obtained by differentiating the functions in (5.20) and in (5.21). Since the differentiation is performed on smooth functions, the fit of $h_{v\theta}$ that is obtained is smooth as well. The result, which is written as

$$h_{v\theta}^*(v, \theta) = \varphi_v^*(v) + \psi_{v\theta}^*(\theta, v),$$ (5.25)

is referred to below as the 'once-fitted' approximation of the distribution function; that is, we define

$$\tilde{f}^{(1)*} \equiv h_{v\theta}^*(v, \theta)/v$$ (5.26)

where the once-starred quantities refer to results of the fitting procedure. The next step is to fit the function $-\log(\tilde{f}^{(1)*})$ by another analytic function so as to obtain a form which is similar to those used in the kinetic theory of gases (i.e. one that is the exponential function of an expression in the velocity). We have found that the following expression furnishes a close fit to $-\log(\tilde{f}^{(1)*})$:

$$-\log(\tilde{f}^{(1)**}) = b^{(0)}(\theta) + b^{(1)}(\theta)v + b^{(2)}(\theta)v^2$$ (5.27)
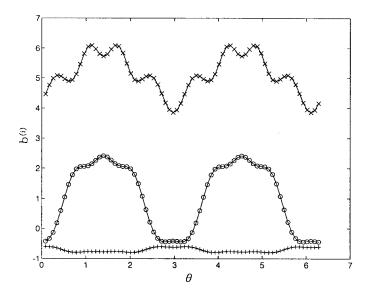
Figure 5.4: The coefficients $b^{(i)}$, $i = 0, 1, 2$, denoted by $+$, $\circ$, and $\times$ respectively, versus θ for given values of T and ρ (these values are the same as for Fig. 5.1). The solid curves through the data points are given by (5.29).

where the coefficients $b^{(i)}$, $i = 0, 1, 2$, are functions of θ. The double-star superscript in $\tilde{f}^{(1)**}$ indicates that it is a fit to the function in (5.26) that is superscripted by a single star, viz. $\tilde{f}^{(1)*}$. Equation (5.27) is called the 'twice-fitted' approximation and we have the final result

$$
\begin{aligned}
\hat{f}^{(1)}(v, \theta; \rho, T, \tilde{e}\,) \;\simeq\; & \rho \tilde{f}^{(1)**} \\
= \; & \rho \exp\!\big(-b^{(0)}(\theta; \rho, T, \tilde{e}\,) - b^{(1)}(\theta; \rho, T, \tilde{e}\,)v - b^{(2)}(\theta; \rho, T, \tilde{e}\,)v^2\big)
\end{aligned}
$$

$$(5.28)$$

in which we have made explicit the dependence on the macrofields and the parameters of the system. For all the parameter values, in particular for all density and temperature values that we have checked, we find that powers of v higher than the second are not needed to fit $-\log(\tilde{f}^{(1)*})$ accurately, and that the fit in fact worsens when a third or fourth power of v is allowed. As $\hat{f}^{(1)}$ is periodic in θ with period π, so are the functions $b^{(0)}$, $b^{(1)}$, and $b^{(2)}$. It follows that these coefficients can be expanded
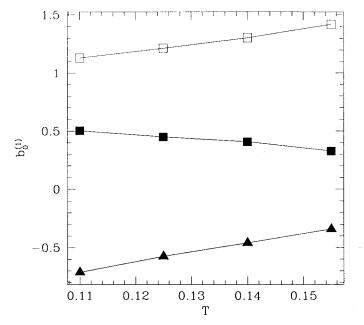
Figure 5.5: Nondimensionalized zeroth order amplitudes, $b_0^{(0)}$, $\sqrt{2T}b_0^{(1)}$, and $2Tb_0^{(2)}$, corresponding to $\triangle$, $\square$, and $\square$ respectively, versus T for given ρ (whose value is the same as for Fig. 5.1).

in a sine series as follows:

$$b^{(i)*}(\theta; \rho, T, \tilde{e}\,) = b_0^{(i)*}(\rho, T, \tilde{e}\,) + \sum_{j=1}^{6} b_{2j}^{(i)*}(\rho, T, \tilde{e}\,) \sin\{2j\,[\theta + \varepsilon_{2j}(\rho, T, \tilde{e}\,)]\}, \quad i = 0, 1, 2$$

(5.29)

In the above expansion, the amplitudes $b_{2j}^{(i)*}$ and phase shifts ε_{2j} depend on ρ, T, and $\tilde{e}$. Note that the set of phase shifts ε_{2j} is the same for all $b^{(i)*}$, $i = 0, 1, 2$, as expected from the 'rotation by π' symmetry of the flow. A graph of ε_{2j} versus T at fixed ρ is shown in Fig. 5.6. As indicated in (5.29), the truncation of the series to only six sine harmonics is sufficient to reproduce the $b^{(i)}$'s accurately. The quality of the fit $b^{(i)*}$ to the corresponding $b^{(i)}$ which were obtained from the data (cf. (5.27)) is demonstrated in Fig. 5.4. The zeroth order amplitudes, $b_0^{(i)*}$, of this fit, i.e. the mean values of $b^{(i)*}$, are shown versus T at fixed ρ in Fig. 5.5. The points shown are nondimensionalized as explained in the figure caption. It is useful to note that the corresponding graph for an an elastic system in a state of equilibrium would be given by $2T\tilde{b}_0^{(2)} = 1$ and $\sqrt{2T}\tilde{b}_0^{(1)} = 0$.

An additional assessment of the quality of the fits given by (5.26) and (5.27) can
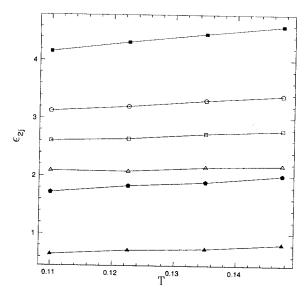
Figure 5.6: Phase shifts ε_{2j}, $j = 1, \cdots, 6$, corresponding to $\triangle$, $\square$, $\diamond$, $\triangle$, $\square$, and $\diamond$ respectively, versus T for given ρ (whose value is as for Fig. 5.1).

be obtained by comparing the kinetic stresses calculated by using $\tilde{f}^{(1)*}$ and $\tilde{f}^{(1)**}$. Let

$$\tau^{(k)*}(\rho, T) = \begin{pmatrix} \int v^3 \cos^2 \theta \, \tilde{f}^{(1)*}(v, \theta) \mathrm{d}v \mathrm{d}\theta & \int v^3 \cos \theta \sin \theta \, \tilde{f}^{(1)*}(v, \theta) \mathrm{d}v \mathrm{d}\theta \\ \int v^3 \cos \theta \sin \theta \, \tilde{f}^{(1)*}(v, \theta) \mathrm{d}v \mathrm{d}\theta & \int v^3 \sin^2 \theta \, \tilde{f}^{(1)*}(v, \theta) \mathrm{d}v \mathrm{d}\theta \end{pmatrix}$$

$$(5.30)$$

and let $\tau^{(k)**}(\rho, T)$ be defined in a similar way by replacing $\tilde{f}^{(1)*}$ by $\tilde{f}^{(1)**}$ in (5.30). The integrations in (5.30) are over all values of v (where $v \geq 0$) and θ. The values of $\tau^{(k)*}$ and $\tau^{(k)**}$ can also be compared to the value of $\tau^{(k)}(\rho, T)$, i.e. the stress tensor that is obtained directly from numerical data. The latter quantity at fixed values of ρ and T can be computed by using

$$\tau^{(k)}(\rho, T) = \int_{S(\rho, T)} \tau^{(k)}(\mathbf{r}) \mathrm{d}\mathbf{r} \tag{5.31}$$

where $\tau^{(k)}(\mathbf{r})$ is given by (1.4) and the notation $S(\rho, T)$ has been explained in the text preceding (5.5)—it means that the integration is to be carried over a set of cells whose values of the density and temperature lie in a small window around ρ and T. Fig. 5.7 shows the traces of $\tau^{(k)}$, $\tau^{(k)*}$, and $\tau^{(k)**}$ versus T at fixed ρ. The value of $\mathrm{Tr}(\tau^{(k)*})$ is seen to be very close to $\mathrm{Tr}(\tau^{(k)})$, the discrepancy between the two values being less
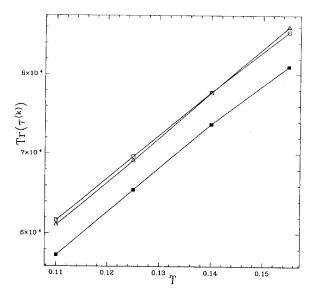
Figure 5.7: Comparison of $\text{Tr}(\tau^{(k)})$, $\text{Tr}(\tau^{(k)*})$, and $\text{Tr}(\tau^{(k)**})$, corresponding to the points $\triangle$, $\square$, and $\square$ respectively. The parameters other than T are as for Fig. 5.1.

than 1%. This should obviously be so since the comparison is made between the data (as represented by $\tau^{(k)}$ after coarse-graining) and a best possible functional fit (which is $\tau^{(k)*}$) that is not subject to any phenomenological constraint. When $\tau^{(k)**}$, which is computed from a physically plausible form for $\tilde{f}^{(1)}$ given by (5.28), is compared to $\tau^{(k)}$, the discrepancy is found to be about 5%. This discrepancy appears to be of systematic nature and is attributed to the fact that for large values of v, $\tilde{f}^{(1)**}$ underestimates $\tilde{f}^{(1)*}$.

5.3 Form and Parameter Dependence of the Distribution Function

The accuracy of the fit for f_1 obtained in Section 5.1 depends on the amount of statistics collected: the more particles that are used in the simulation and the more configurations analyzed, the better the fit. With more statistics, accurate values for the functions $b^{(0)}$, $b^{(1)}$, and $b^{(2)}$, as well as their parametric dependence on T, ρ and $\tilde{e}$ can be determined. The parametric dependence can be determined, for example,
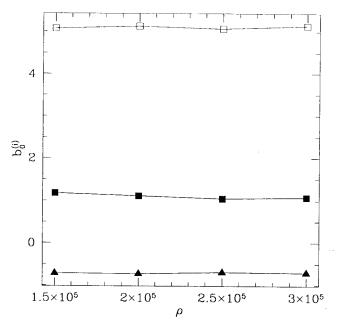
Figure 5.8: Nondimensionalized zeroth order amplitudes, $b_0^{(0)}$, $\sqrt{2T}b_0^{(1)}$, and $2Tb_0^{(2)}$, corresponding to $\triangle$, $\square$, and $\square$ respectively, versus ρ for fixed T (whose value is as for for Fig. 5.1).

by expanding $b_{2j}^{(i)*}$ for each i and each j in powers of T with coefficients that depend on ρ and $\tilde{e}$, and then determining these coefficients by fitting the data. Since the variation of T in the flow for $\tilde{e}$ not too close to zero is not large, a linear or quadratic dependence in T may be sufficient for the fit. We have found that linear fits are sufficient for the cases of $b_0^{(i)*}$ versus T and for $b_0^{(i)*}$ versus ρ, as Fig. 5.5 and Fig. 5.8 show. A summary of the various parameter dependences is presented in Appendix B in which results for $\tilde{e}$ =0.6, 0.7, 0.8, and 0.9 are presented (the parameters other than $\tilde{e}$ are as for System **III**). It seems that the dependence of the amplitudes $b_{2j}^{(i)}$ for $j > 0$ (i.e. the amplitudes beyond the zeroth order) on the parameters of the problem is more complex than anticipated, though we believe that this complexity is still due in part to noise and insufficient statistics. Since the present work has been performed on a superworkstation, it is expected that when additional statistics are generated using a supercomputer, the remaining noise can be significantly reduced. The qualitative and semi-quantitative dependence (accurate to within 20-30%) of these amplitudes on the parameters of the problem is not changed when additional statistics is collected.
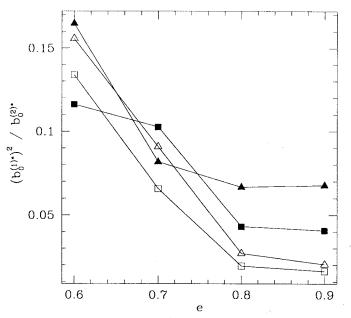
Figure 5.9: The dimensionless ratio $(b_0^{(1)*})^2/b_0^{(2)*}$ versus $\tilde{e}$. For each $\tilde{e}$, this ratio is computed for different values of ρ (where $\rho = 1.6 \times 10^5$/unit area, 2.0×10^5/unit area, 2.4×10^5/unit area, and 2.8×10^5/unit area, corresponding to the points $\triangle$, $\square$, $\triangle$, and $\square$ respectively) and for the value of T that corresponds to the average temperature in the system with the given value of $\tilde{e}$. The external parameters other than $\tilde{e}$ are the same as those of System **III** .

Fig. 5.9 plots the dimensionless ratio $(b_0^{(1)*})^2/b_0^{(2)*}$ versus $\tilde{e}$ for several values of ρ and for a fixed value of T that corresponds to the average temperature in the system (characterized by the given value of $\tilde{e}$). Fig. 5.9 indicates that, relative to the size of quadratic coefficient, $b_0^{(2)*}$, the size of the linear coefficient, $b_0^{(1)*}$, is largest when $\tilde{e}$ is small; it decreases as $\tilde{e}$ increases and it tends to zero as $\tilde{e}$ approaches the value 1, as one expects in the elastic limit. When $\tilde{e}$ is not close to unity and the flow is highly inhomogeneous, regions with very different characteristic values of the fluctuating speed (different 'phases') coexist in the same statistical steady state (i.e. in 'dynamic equilibrium') and therefore the difference between the values of $b^{(1)}$ corresponding to these regions can be large. The amplitudes of the higher harmonics in $b^{(i)}$, $i = 0, 1, 2$, also increase as $\tilde{e}$ becomes smaller, indicating that the flow is more anisotropic as well. These higher harmonics disappear as $\tilde{e}$ tends to 1.
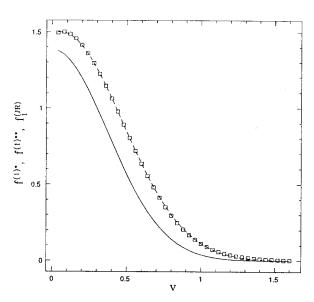
Figure 5.10: The generalized Gaussian distribution for dilute shear flow, $f_1^{(JR)}$, versus $f^{(1)*}$ and $f^{(1)**}$. The $\square$ points correspond to $f^{(1)*}$, while the dashed line correspond to $f^{(1)**}$ and the solid line to $f_1^{(JR)}$. All distributions are shown versus v at fixed $\theta = \pi$ and $T = 0.11$.

The form of $f^{(1)}$ obtained in this work is significantly different from the ones assumed in existing kinetic theories for granular flow. These distributions are analytic in the Cartesian components of the velocity and have simple angular dependences. However, the form of $f^{(1)}$ which we have determined is both non-analytic in these components and highly anisotropic. Specifically, this form, while not containing, in the exponent, powers of the fluctuating speed v beyond the second (as in previous results), does contain a linear power of v. The linear power renders the function non-analytic in the Cartesian components of **v**. Morever, the magnitude of the linear coefficient, $b^{(1)}$, in highly inelastic systems is of the same order as that of the quadratic coefficient, $b^{(2)}$, though it is still smaller in size in general. Each of the coefficients $b^{(i)}$, $i = 0, 1, 2$, contains a finite number of nonnegligible Fourier components implying a rather complicated angular dependence in $f^{(1)}$.

A comparison of $f^{(1)}$ with the distribution function for homogeneous shear flows derived by Jenkins and Richman[39] who assumed a generalized Gaussian form is

given in Fig. 5.10 and Fig. 5.11. The two-dimensional generalized Gaussian ('anisotropic Maxwellian') form is

$$f_1^{(JR)} = \frac{\rho}{2\pi\sqrt{\det \mathbf{K}}} \exp\left(-\frac{1}{2}\mathbf{v}\cdot\mathbf{K}^{-1}\cdot\mathbf{v}\right) \tag{5.32}$$

where $\mathbf{K}$ is the second moment of the velocity fluctuations given by

$$\rho\mathbf{K} \equiv \int_{\mathbf{V}} \mathbf{v}\mathbf{v} f_1^{(JR)} d\mathbf{v}. \tag{5.33}$$

In the dilute limit of the generalized Gaussian theory for shear flow, $f_1^{(JR)}$ takes the form:

$$\log f_1^{(JR)} \propto -\frac{v^2}{T}\left[1 + A^2 + A\sqrt{1+A^2}\sin(2\theta + \chi)\right] \tag{5.34}$$

where $\chi = -\tan^{-1}(A)$, and A depends, in this limit, on $\tilde{e}$ only. Thus $\log f_1^{(JR)}$ contains only a single harmonic in θ with a phase shift χ that depends on $\tilde{e}$ only. The results presented in this chapter suggest that the actual single-particle distribution function has a much richer structure.

The high degree of anisotropy in f_1 and its non-analyticity in the components of the velocity implies that it cannot be adequately approximated by a generalized Gaussian or by a standard perturbative expansion in the field variables. The generalized Gaussian form used by Jenkins and Richman provides a representation of f_1 which is superior to that of a Gaussian. In fact, it generates a theory that predicts closely the average value of the temperature in the shear flow (cf. Fig. 3.2). In contrast, earlier theories (e.g. Ref. [6]), which do not account for the anisotropy of the second moment $\mathbf{K}$, predict a zero intercept for the graph in Fig. 3.2, i.e. they give $B = 0$ in (3.1). Although the most general representation of f_1 in two dimensions is an arbitrary (and normalizable) function of v and θ (with a similar function of the spherical polar coordinates applicable in three dimensions), the number of significant harmonics in the θ dependence is small and therefore a good approximation of f_1 may be obtained by perturbatively correcting a generalized Gaussian form with an expansion in powers of both v and $\hat{\mathbf{v}}$, where $\hat{\mathbf{v}}$ is the unit vector in the direction of $\mathbf{v}$. This approximation is very general; the coefficient of each corrective power in the expansion will depend on the moments of v or $\hat{\mathbf{v}}$ and it can be determined by deriving equations of motion for the corresponding moments. The moments of $\hat{\mathbf{v}}$ will
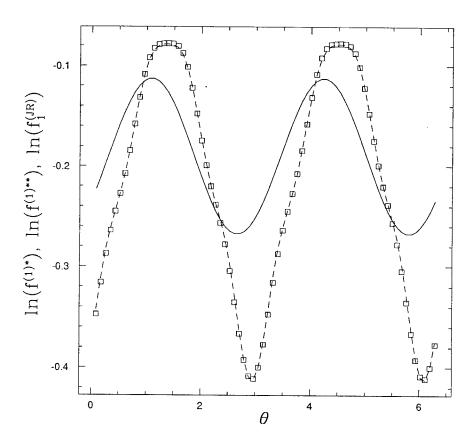
Figure 5.11: The generalized Gaussian distribution for dilute shear flow, $f_1^{(JR)}$, versus $f^{(1)*}$ and $f^{(1)**}$. The □ points correspond to $f^{(1)*}$, while the dashed line correspond to $f^{(1)**}$ and the solid line to $f_1^{(JR)}$. All distributions are shown versus θ at fixed $v = 1.6$ and $T = 0.11$

then correspond to additional field variables that account for the angular anisotropy of the flow.

5.4   Summary

In this paper, we have accurately determined the single-particle distribution function for a simple granular shear flow and shown that it has a structure that is more complicated than hitherto assumed. The form of the function is neither a Gaussian nor a generalized Gaussian and it cannot be represented by a moment expansion in the usual densities of mass, momentum and granular temperature. A linear term in the speed and highly anisotropic coefficients are present in the exponent of the function due to the anisotropy of the flow. The magnitude of the linear term increases with increasing inelasticity, and hence with flow inhomogeneity, since dense microstructures are created when the flow is very inelastic. The anisotropic angular structure becomes more pronounced in this regime as well. The fact that the distribution function is non-analytic and highly anisotropic implies that field variables that measure the anisotropy, in addition to the standard hydrodynamic variables, must be included in any successful theory describing the dynamics of granular flow.

Appendix A

Numerical Method and Performance Tests

The numerical method used in this work is based on the 'event-driven' algorithm which is extremely efficient for simulating the dynamics of particle systems with short-range interaction potentials. The idea behind the algorithm is to decompose the flow domain into a mesh of computational cells and then compute the flow by executing a sequence of 'events', where an 'event' is either a binary collision or the propagation of a particle from one computational cell to an adjacent cell. The events for each particle are 'scheduled' by searching for possible future collisions and cell-crossings within a neighborhood of cells around the given particle. By localizing the search for future collisions, the algorithm reduces the operation count from $\mathcal{O}(N^2)$ to $\mathcal{O}(N \log N)$, where N is the number of particles in the system. A brief description of this algorithm is provided below; the reader is refered to Ref. [55] for more details. A three-dimensional version of the code based on the same algorithm was implemented as well, and some preliminary results of three-dimensional simulations are presented in Appendix C.

A.1 The Event-Driven Algorithm

In a rigid disk system on which no body forces are exerted, particles move with constant velocities between instantaneous collisions in trajectories that are piecewise linear. Since a given particle typically collides only with neighboring particles, the search for possible collisions with the given particle need only be carried out among particles lying within its immediate neighborhood. Such a neighborhood can be defined for each particle in a straightforward way by superposing an rectangular mesh of cells, whose interstices are smaller than the range of the interparticle interaction, on the flow domain. For the case of identical rigid disks, the range of interaction is equal to the diameter of the disk. Note also that the event-driven algorithm deals only with binary collisions. The neighboring particles among which collisions with a given particle need be checked are just those that lie within a 3 × 3 array of cells in which the cell at the center is the one where the given particle resides. Clearly, a particle may also collide with another particle in a cell that lies beyond the set of neighhboring cells defined above. In this case, the particle has to cross into another cell before the collision and therefore such a collision is mediated by a change in the particle's 'cell residence'. With the mesh in place, the change of cell residence of a particle is continually computed as part of the event-driven algorithm. The dynamical history of the particle is segmented into 'events' corresponding to either collisions with neighboring particles (binary events) or, in the absence of such collisions, crossings into neighboring cells (unary events). The dynamical history of the system as a whole is computed by computing the events, which are either 'collision' events or 'crossing' events, for each particle in it. The events are 'scheduled' for each particle by computing their trajectories and they are then put into a list in order of the time of occurrence. The events in the list are then executed sequentially so that the system advances in time-steps corresponding to the intervals between the times of occurrence of these events.

The computational effort required to predict future events in the system is reduced, by using the superposed array of computational cells, from $\mathcal{O}(N^2)$ to $\mathcal{O}(N)$, where N is the number of particles in the system. There are several ways of organizing the

list of future events which allow for their rapid addition and deletion and also for the 'compaction' of the event list. A very efficient method is that of the dynamically allocated linked-list structure supplemented by a two-tier referencing (i.e. a pointer-to-pointer) strategy to enhance speed of access to actual data. We have implemented code to provide for the efficient allocation of data structures on an as-needed basis and for fast streamlined access of linked-list data. We have produced both two- and three-dimensional codes based on these methods and also extended the basic event-driven algorithm to simulate flows with several boundary conditions, including rigid-wall boundary conditions[16].

Dividing the flow domain into computational cells allows many types of boundary conditions to be applied easily. In the case of the Lees-Edwards boundary condition, the particles near the top or bottom boundaries will collide with those near the corresponding boundaries in the images of the system. This type of collisions have to be computed only for particles lying within a layer of cells adjacent to the boundaries. In practice, one takes a layer of cells adjacent to the bottom (say) boundary, copies the data of the particles into temporary storage, applies a Galilean transformation determined by the velocity parameter to the coordinates and velocities of all particles in the layer (now stored in the temporary storage), repartitions the layer into cells, and then attaches the layer next to the top boundary. The scheduling of collisions for the particles in the cells adjacent to the top boundary then proceeds as the scheduling that is done for particles elsewhere. Once a collision between a particle in the system near the boundary (call it particle 1) and another in the system's image, which is really the image of a particle (call it particle 2) near the opposite boundary in the system, has been scheduled and is to be executed, a Galilean transformation is applied to the coordinate and velocity of particle 2. The post-collisional velocities are then computed and a transformation that is the inverse of the one applied before is then applied to particle 2 (whose velocity will have been changed by the collision).

The case of a reflective boundary condition can also be handled easily by the event-driven algorithm. An example of a reflective boundary condition is one corresponding to a moving rigid wall or one applied at ledges or the surfaces of obstacles in the flow. We assume that the boundaries at which the condition is applied are

aligned along the edges of the computational cells into which the flow domain has been divided. The cells adjacent to the boundary, i.e. the cells one or more of whose edges are parts of the boundary, are appropriately flagged to reflect their special status. The flag will contain information as to which edges of the cell are boundaries and which edges are common with those of adjacent cells. A particle in a cell adjacent to a boundary which is propagated to the boundary is reflected from it in the way specified by the elementary interaction corresponding to the type of boundary condition applied. If the particle is propagated to an edge common with that of an adjacent cell, then it is simply transfered to the adjacent cell. Thus algorithmically the reflective boundary conditions are applied when the crossing events corresponding to a 'boundary crossing' (as opposed to a 'cell crossing') are executed; and herein lies the simplicity of the event-driven algorithm with respect to the implementation of complex boundary conditions—these conditions are applied as part of the 'normal' routine of scheduling and executing crossing events. Some results of complex flow simulations are presented in Ref. [16].

In systems on which body forces are exerted, the trajectories of the particles are no longer piecewise linear. For constant body forces such as gravity, the trajectories are parabolae, since the distance traveled by a particle depends on the square of the time taken. Thus multiple solutions are obtained when predicting the future collision and cell crossing times for a particle and only the smallest positive solution must be admitted. Apart from the slight complication with the choice of collision or crossing times, the event-driven algorithm proceeds in the same way as for the case of systems without body forces. Results of gravity-driven flow simulations are available in Ref. [16].

A.2 Performance Tests

The main conclusions on performance that can be drawn from our tests of the event-driven code are (1) the most efficient computational meshes are those containing on the average between one to two particles per cell; (2) the efficiency improves for moderately dense systems since a smaller proportion of the computational effort
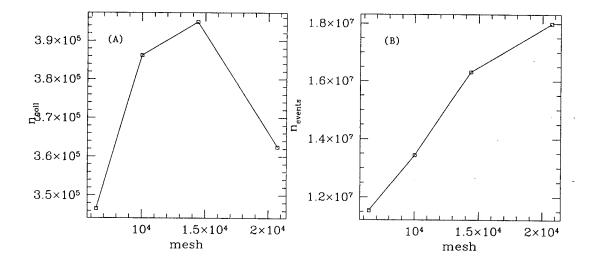
Figure A.1: (A) n_{coll} and (B) n_{event} versus the number of cells in the mesh. The number of particles in the system is 20000 and $\tilde{e}$ =0.6. The mesh sizes corresponding to the datapoints are: 6400 (80×80), 10000 (100×100), 14400 (120×120), and 20736 (144×144).
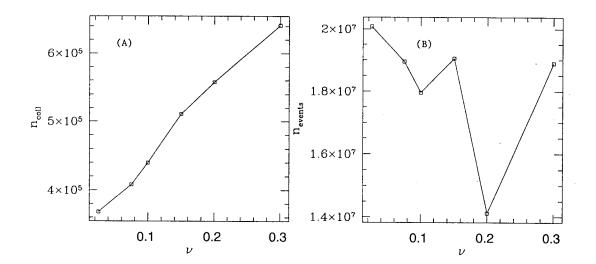
Figure A.2: (A) n_{coll} and (B) n_{event} versus the solid fraction, ν, of the system. The number of particles in the system is 20000 and $\tilde{e}$ =0.6. The mesh size is (144×144) and is the same for all values of ν.

is spent on computing the crossing events; and (3) the efficiency improves as the inelasticity decreases, since inhomogeneities in the system are reduced. These trends are depicted in Fig. A.1, Fig. A.2 and Fig. A.3. The most meaningful measure of the efficiency of the code is the the total number of collisions computed per hour of computing time; n_{coll}, since the average time interval between successive collisions of a particle corresponds to a 'relaxation' or 'randomization' time for the system and thus the accumulated number of collisions in the system is a measure of how much it has evolved dynamically. Fig. A.1 shows that the more efficient meshes are the ones containing on the average between one to two particles per cell. As the mesh size decreases, the cell size *increases* and more particles are found in each cell. This decreases the computational efficiency since the number of neighboring particles among which collisions with a given particle must be searched is larger and the operation count for the search scales as the square of the number of neighboring particles. On the other hand, a reduction in the number of cell crossings, which *increases* the computational efficiency, is possible if the cell size is smaller. Thus a cross-over to lower efficiency occurs when the mesh size is chosen to be too large.
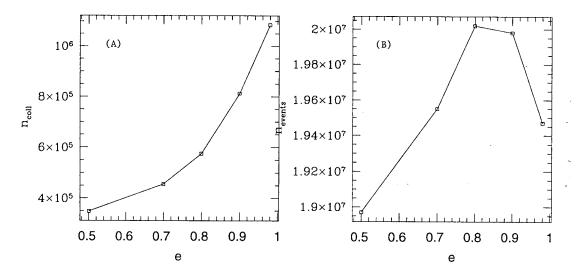
Figure A.3: (A) n_{coll} and (B) n_{event} versus $\tilde{e}$. The number of particles in the system is 20000 and $\nu = 0.05$. The mesh size is 20736 (144×144) and is the same for all values of $\tilde{e}$.

Fig. A.2 shows that n_{coll} increases with the solid fraction ν. This is easy to understand since the mean free path of the particles *decreases* with increasing ν, and therefore a particle travels a shorter distance and thus crosses a lesser number of cells before each collision. When the system is close to random packing density, the particle may collide many times before it even traverses a single cell. The conclusion to be drawn here is that the event-driven algorithm is more efficient at higher densities. However, at very high densities the simulations performed using the event-driven method may not be physically meaningful since multiple-particle contacts will become important in this regime.

Fig. A.3 shows that n_{coll} increase with $\tilde{e}$, while n_{events} first increases and then decreases with $\tilde{e}$. This is again easy to understand since particle clustering is more pronounced—hence density is more inhomogeneous—when the system is more inelastic, which implies that the distribution of particles in the computational mesh will become more uneven. There will be accumulation of large numbers of particles in some cells which leads to a lowering of the overall computational efficiency, since the operation count for the search for possible collisions scales as the square of number

of particles in a given cell and its immediate neighbors. Clearly the compensating depletion of particles from other cells does nothing to improve the efficiency, since empty cells are merely bypassed in the computation of collisions.

Appendix B

Parametric Dependence of f_1

The variables and parameters in the 'twice-fitted' approximation to $f^{(1)}$ given in these tables are explained in Section 5.2.

$\tilde{e}$	ρ	T	j	ε_{2j}	$b_{2j}^{(0)}$	$b_{2j}^{(1)}$	$b_{2j}^{(2)}$
0.6	$(1.6 \pm 0.2)10^5$	0.11 ± 0.0075	0		-0.7174	1.1740	5.0767
			1	-0.8460	0.0513	1.2346	1.5310
			2	3.0205	0.0189	0.0948	0.3543
			3	0.6037	0.0351	0.1943	0.3243
			4	1.3285	0.0618	0.3601	0.5150
			5	2.0533	0.0046	0.0520	0.1299
			6	2.7782	0.0010	0.0123	0.0297
		0.125 ± 0.0075	0		-0.5616	0.9208	4.9318
			1	-0.8367	0.1291	1.7669	0.9603
			2	3.0389	0.0591	0.4315	0.1538
			3	0.6314	0.0023	0.0171	0.0068
			4	1.3655	0.0063	0.0807	0.2802
			5	2.0996	0.0051	0.0786	0.2344
			6	2.8336	0.0013	0.0191	0.0490
		0.14 ± 0.0075	0		-0.4608	0.8662	4.6282
			1	-0.8226	0.1520	1.8696	0.8173
			2	3.0672	0.0962	0.5603	0.2390
			3	0.6738	0.0072	0.0265	0.2098
			4	1.4221	0.0548	0.1661	0.0510
			5	2.1703	0.0016	0.0256	0.0350
			6	2.9185	0.0025	0.0184	0.0336
		0.155 ± 0.0075	0		-0.2821	0.5337	4.5315
			1	-0.8076	0.2907	2.8314	0.5347
			2	3.0960	0.1551	0.9858	0.7691
			3	0.7170	0.0413	0.1506	0.0855
			4	1.4795	0.0327	0.2533	0.4452
			5	2.2421	0.0070	0.0925	0.2246
			6	3.0047	0.0021	0.0218	0.0482

$\tilde{e}$	ρ	T	j	ε_{2j}	$b_{2j}^{(0)}$	$b_{2j}^{(1)}$	$b_{2j}^{(2)}$
0.6	$(2.0 \pm 0.2)10^5$	0.11 ± 0.0075	0		-0.727	1.111	5.226
			1	-0.9056	0.0369	0.9908	1.8696
			2	-0.2403	0.0119	0.1311	0.1446
			3	0.4249	0.0124	0.1192	0.3186
			4	1.0901	0.0378	0.2417	0.3337
			5	-1.3863	0.0040	0.0477	0.1079
			6	2.4206	0.0007	0.0092	0.0221
		0.125 ± 0.0075	0		-0.586	0.983	4.842
			1	-0.8994	0.1538	1.8601	0.6301
			2	2.9136	0.0895	0.5842	0.3607
			3	-2.6981	0.0239	0.1198	0.0213
			4	1.1149	0.0098	0.0227	0.0669
			5	-1.3553	0.0028	0.0395	0.1313
			6	2.4577	0.0010	0.0129	0.0322
		0.14 ± 0.0075	0		-0.412	0.650	4.7189
			1	-0.8789	0.2209	2.2043	0.2391
			2	2.9546	0.1098	0.6574	0.4164
			3	-2.6367	0.0403	0.2185	0.1454
			4	1.1968	0.0014	0.0018	0.0352
			5	-1.2529	0.0041	0.0513	0.1460
			6	2.5806	0.0006	0.0099	0.0276
		0.155 ± 0.0075	0		-0.340	0.666	4.512
			1	-0.8534	0.1829	1.9872	0.6765
			2	3.0055	0.0749	0.4413	0.1012
			3	0.5813	0.0193	0.1434	0.3109
			4	1.2987	0.0790	0.4433	0.5591
			5	-1.1256	0.0006	0.0201	0.0618
			6	2.7334	0.0026	0.0219	0.0416

$\tilde{e}$	ρ	T	j	ε_{2j}	$b_{2j}^{(0)}$	$b_{2j}^{(1)}$	$b_{2j}^{(2)}$
0.6	$(2.4 \pm 0.2)10^5$	0.11 ± 0.0075	0		-0.694	1.047	5.066
			1	0.980	0.089	1.573	0.682
			2	2.753	0.050	0.374	0.137
			3	0.203	0.013	0.006	0.106
			4	0.794	0.023	0.165	0.288
			5	1.757	0.004	0.051	0.127
			6	1.976	0.001	0.010	0.022
		0.125 ± 0.0075	0		-0.5679	0.856	4.959
			1	0.958	0.158	1.757	0.741
			2	2.797	0.103	0.701	0.561
			3	0.269	0.064	0.224	0.114
			4	0.882	0.074	0.256	0.052
			5	1.646	0.001	0.032	0.074
			6	2.109	0.002	0.010	0.014
		0.14 ± 0.0075	0		-0.4789	0.857	4.617
			1	0.944	0.091	1.298	1.499
			2	2.830	0.014	0.007	0.256
			3	0.311	0.024	0.217	0.527
			4	0.938	0.091	0.486	0.526
			5	1.577	0.002	0.011	0.008
			6	2.192	0.001	0.001	0.001
		0.155 ± 0.0075	0		-0.3177	0.562	4.496
			1	0.921	0.181	1.896	0.633
			2	2.871	0.118	0.631	0.359
			3	0.379	0.029	0.162	0.096
			4	1.029	0.001	0.042	0.194
			5	1.463	0.006	0.080	0.216
			6	2.329	0.001	0.012	0.034

$\tilde{e}$	ρ	T	j	ε_{2j}	$b^{(0)}_{2j}$	$b^{(1)}_{2j}$	$b^{(2)}_{2j}$
0.6	$(2.8 \pm 0.2)10^5$	0.11 ± 0.0075	0		-0.711	1.075	5.135
			1	2.088	0.096	1.523	0.845
			2	2.605	0.036	0.247	0.031
			3	3.122	0.020	0.145	0.182
			4	0.645	0.023	0.163	0.293
			5	4.157	0.003	0.036	0.091
			6	1.722	0.001	0.008	0.017
		0.125 ± 0.0075	0		-0.58	0.861	4.971
			1	2.080	0.115	1.481	1.107
			2	2.639	0.097	0.492	0.139
			3	3.198	0.002	0.020	0.106
			4	0.715	0.038	0.234	0.316
			5	4.316	0.002	0.033	0.079
			6	1.833	0.001	0.014	0.028
		0.14 ± 0.0075	0		-0.460	0.772	4.652
			1	2.148	0.083	1.249	1.463
			2	2.726	0.006	0.094	0.286
			3	3.303	0.054	0.352	0.576
			4	0.739	0.050	0.296	0.369
			5	4.459	0.002	0.028	0.059
			6	1.894	0.000	0.003	0.012
		0.155 ± 0.0075	0		-0.340	0.589	4.578
			1	2.176	0.244	2.276	0.155
			2	2.780	0.143	0.875	0.737
			3	3.385	0.045	0.207	0.126
			4	0.818	0.001	0.039	0.058
			5	4.594	0.004	0.038	0.108
			6	2.007	0.000	0.008	0.022

$\tilde{e}$	ρ	T	j	ε_{2j}	$b_{2j}^{(0)}$	$b_{2j}^{(1)}$	$b_{2j}^{(2)}$
0.7	$(1.6 \pm 0.2)10^5$	0.12 ± 0.02	0		0.1183	0.3927	2.5448
			1	2.3863	0.0463	0.6947	0.4123
			2	0.0601	0.0059	0.0094	0.1344
			3	0.8756	0.0568	0.2471	0.2144
			4	1.6911	0.0310	0.3600	0.5464
			5	2.5065	0.0011	0.0179	0.0203
			6	0.1804	0.0006	0.0026	0.0032
		0.16 ± 0.02	0		0.3530	0.3761	2.1193
			1	2.4254	0.0873	0.7425	0.5703
			2	0.1383	0.1066	0.6482	0.9137
			3	0.9929	0.1324	0.7017	0.8130
			4	1.8474	0.0407	0.2451	0.2325
			5	2.7020	0.0056	0.0398	0.0776
			6	0.4150	0.0018	0.0105	0.0129
		0.20 ± 0.02	0		0.5444	0.4247	1.7447
			1	2.4569	0.1676	1.2429	0.0276
			2	0.2014	0.0053	0.1103	0.2508
			3	1.0874	0.0366	0.2101	0.1761
			4	1.9735	0.0180	0.0556	0.0165
			5	2.8596	0.0011	0.0102	0.0178
			6	0.6041	0.0002	0.0016	0.0031
		0.24 ± 0.02	0		0.7131	0.4233	1.4928
			1	2.4614	0.0276	0.5295	0.8091
			2	0.2104	0.1220	0.6974	1.0116
			3	1.1010	0.1276	0.6550	0.7767
			4	1.9916	0.0761	0.4707	0.6825
			5	2.8822	0.0067	0.0449	0.0705
			6	0.6312	0.0061	0.0368	0.0507

$\tilde{e}$	ρ	T	j	ε_{2j}	$b_{2j}^{(0)}$	$b_{2j}^{(1)}$	$b_{2j}^{(2)}$
0.7	$(2.0 \pm 0.2)10^5$	0.12 ± 0.02	0		-0.4986	0.6074	4.6197
			1	2.3338	0.1266	1.2486	0.3775
			2	-0.0447	0.0030	0.0748	0.4164
			3	0.7183	0.0751	0.5568	0.8881
			4	1.4814	0.0712	0.4385	0.6580
			5	2.2444	0.0028	0.0299	0.0637
			6	3.0074	0.0009	0.0074	0.0137
		0.16 ± 0.02	0		-0.2407	0.5693	3.6365
			1	2.3745	0.0539	0.6863	1.2909
			2	0.0367	0.0488	0.3542	0.7331
			3	0.8404	0.0192	0.1444	0.3170
			4	1.6441	0.0141	0.1247	0.1267
			5	2.4479	0.0007	0.0109	0.0468
			6	0.1100	0.0002	0.0019	0.0050
		0.20 ± 0.02	0		-0.0479	0.6065	3.0250
			1	2.4127	0.1378	1.3896	0.2179
			2	0.1130	0.0467	0.3574	0.7612
			3	0.9548	0.0161	0.1274	0.2876
			4	1.7967	0.0006	0.0487	0.1547
			5	2.6386	0.0002	0.0060	0.0160
			6	0.3389	0.0001	0.0009	0.0017
		0.24 ± 0.02	0		0.1592	0.4788	2.6746
			1	2.4256	0.0592	0.8696	1.1121
			2	0.1388	0.1041	0.9100	1.8483
			3	0.9937	0.1312	0.9483	1.5137
			4	1.8485	0.0634	0.4503	0.7845
			5	2.7033	0.0042	0.0327	0.0627
			6	0.4165	0.0051	0.0411	0.0743

$\tilde{e}$	ρ	T	j	ε_{2j}	$b_{2j}^{(0)}$	$b_{2j}^{(1)}$	$b_{2j}^{(2)}$
0.7	$(2.4 \pm 0.2)10^5$	0.12 ± 0.02	0		-0.5185	0.6875	4.5430
			1	2.2666	0.1178	1.1161	0.4865
			2	2.9624	0.0078	0.0038	0.2704
			3	0.5166	0.0208	0.1708	0.3298
			4	1.2124	0.0283	0.2047	0.3934
			5	1.9082	0.0006	0.0017	0.0094
			6	2.6040	0.0001	0.0006	0.0013
		0.16 ± 0.02	0		-0.2419	0.5428	3.6687
			1	2.3121	0.0644	0.7186	1.1707
			2	3.0535	0.0515	0.3419	0.6933
			3	0.6532	0.0244	0.1284	0.2704
			4	1.3946	0.0146	0.1657	0.2356
			5	2.1359	0.0007	0.0077	0.0379
			6	2.8773	0.0001	0.0017	0.0045
		0.20 ± 0.02	0		-0.0369	0.5615	2.9887
			1	2.3558	0.0558	0.8185	0.9484
			2	3.1407	0.0495	0.3519	0.7809
			3	0.7841	0.0050	0.0497	0.1615
			4	1.5690	0.0168	0.2494	0.5146
			5	2.3540	0.0006	0.0110	0.0163
			6	3.1389	0.0002	0.0018	0.0040
		0.24 ± 0.02	0		0.1833	0.3679	2.7302
			1	2.3769	0.0500	0.7292	1.3415
			2	0.0414	0.0683	0.6301	1.3627
			3	0.8475	0.0838	0.5939	0.9950
			4	1.6536	0.0172	0.0222	0.0471
			5	2.4596	0.0016	0.0116	0.0436
			6	0.1241	0.0018	0.0139	0.0237

$\tilde{e}$	ρ	T	j	ε_{2j}	$b_{2j}^{(0)}$	$b_{2j}^{(1)}$	$b_{2j}^{(2)}$
0.7	$(2.8 \pm 0.2)10^5$	0.12 ± 0.02	0		-0.5437	0.8009	4.3872
			1	2.2012	0.0760	0.7509	0.9357
			2	2.8316	0.0483	0.2929	0.1726
			3	0.3205	0.0357	0.2048	0.1765
			4	0.9509	0.0225	0.1723	0.2228
			5	1.5813	0.0011	0.0121	0.0404
			6	2.2118	0.0005	0.0034	0.0054
		0.16 ± 0.02	0		-0.2445	0.5138	3.7167
			1	2.2442	0.1336	1.2379	0.3006
			2	2.9177	0.0314	0.1555	0.3704
			3	0.4495	0.0213	0.1792	0.3408
			4	1.1230	0.0053	0.0371	0.0326
			5	1.7964	0.0001	0.0004	0.0226
			6	2.4699	0.0001	0.0002	0.0019
		0.20 ± 0.02	0		-0.0175	0.4320	3.1189
			1	2.3101	0.0932	0.9498	0.8019
			2	3.0493	0.0700	0.5396	1.0573
			3	0.6470	0.0656	0.4471	0.6909
			4	1.3863	0.0097	0.0077	0.0124
			5	2.1255	0.0010	0.0045	0.0116
			6	2.8648	0.0010	0.0070	0.0108
		0.24 ± 0.02	0		0.2011	0.2987	2.7155
			1	2.3258	0.0880	1.1312	0.4334
			2	3.0808	0.0633	0.4359	0.4180
			3	0.6943	0.0496	0.1510	0.0978
			4	1.4493	0.0437	0.0548	0.0222
			5	2.2043	0.0031	0.0356	0.0321
			6	2.9593	0.0007	0.0072	0.0137

$\tilde{e}$	ρ	T	j	ε_{2j}	$b_{2j}^{(0)}$	$b_{2j}^{(1)}$	$b_{2j}^{(2)}$
0.8	$(1.6 \pm 0.2)10^5$	0.18 ± 0.03	0		-0.0409	0.5204	2.7159
			1	2.5894	0.1523	1.0072	0.0043
			2	0.4665	0.0451	0.2470	0.2041
			3	1.4851	0.0143	0.1101	0.1282
			4	2.5037	0.0551	0.2692	0.2972
			5	0.3808	0.0028	0.0211	0.0350
			6	1.3994	0.0010	0.0060	0.0084
		0.24 ± 0.03	0		0.2492	0.3627	2.2009
			1	2.5970	0.0038	0.2309	0.8932
			2	0.4817	0.0542	0.3468	0.5777
			3	1.5079	0.0785	0.4038	0.4680
			4	2.5341	0.0185	0.0003	0.0449
			5	0.4188	0.0012	0.0022	0.0045
			6	1.4450	0.0016	0.0095	0.0130
		0.30 ± 0.03	0		0.4535	0.3663	1.7964
			1	2.6026	0.0637	0.5321	0.5662
			2	0.4928	0.0312	0.1958	0.3391
			3	1.5246	0.0493	0.1538	0.1421
			4	2.5564	0.0608	0.3156	0.3881
			5	0.4466	0.0003	0.0040	0.0074
			6	1.4784	0.0012	0.0064	0.0083
		0.36 ± 0.03	0		0.6380	0.3124	1.5614
			1	2.5998	0.0601	0.0174	1.2012
			2	0.4872	0.0502	0.3287	0.5233
			3	1.5162	0.0129	0.0873	0.2056
			4	2.5453	0.0750	0.5953	0.8010
			5	0.4327	0.0025	0.0210	0.0134
			6	1.4617	0.0009	0.0065	0.0108

$\tilde{e}$	ρ	T	j	ε_{2j}	$b_{2j}^{(0)}$	$b_{2j}^{(1)}$	$b_{2j}^{(2)}$
0.8	$(2.0 \pm 0.2)10^5$	0.18 ± 0.03	0		-0.0156	0.3993	2.8037
			1	2.5219	0.0614	0.4890	0.5529
			2	0.3313	0.0042	0.0349	0.1222
			3	1.2824	0.0027	0.0139	0.0477
			4	2.2334	0.0277	0.1302	0.1408
			5	0.0429	0.0005	0.0051	0.0094
			6	0.9940	0.0000	0.0002	0.0004
		0.24 ± 0.03	0		0.2448	0.3428	2.2272
			1	2.5438	0.0655	0.6386	0.2557
			2	0.3753	0.0232	0.1435	0.2732
			3	1.3483	0.0248	0.1322	0.1608
			4	2.3213	0.0249	0.0939	0.0994
			5	0.1528	0.0003	0.0046	0.0063
			6	1.1258	0.0003	0.0019	0.0026
		0.30 ± 0.03	0		0.4814	0.2534	1.8668
			1	2.5621	0.1007	0.7335	0.2609
			2	0.4118	0.0201	0.1602	0.2818
			3	1.4031	0.0309	0.0713	0.0273
			4	2.3945	0.0035	0.0480	0.0512
			5	0.2442	0.0002	0.0018	0.0084
			6	1.2355	0.0002	0.0009	0.0006
		0.36 ± 0.03	0		0.6463	0.2750	1.5823
			1	2.5601	0.0689	0.7019	0.2682
			2	0.4078	0.0459	0.2126	0.2902
			3	1.3971	0.0318	0.1382	0.1924
			4	2.3864	0.0574	0.1849	0.1817
			5	2.9075	-0.0008	0.0126	0.0144
			6	1.2233	0.0013	0.0069	0.0085

$\tilde{e}$	ρ	T	j	ε_{2j}	$b_{2j}^{(0)}$	$b_{2j}^{(1)}$	$b_{2j}^{(2)}$
0.8	$(2.4 \pm 0.2)10^5$	0.18 ± 0.03	0		0.0083	0.3162	2.8359
			1	2.4717	0.0741	0.6255	0.2072
			2	0.2271	0.0119	0.0980	0.1999
			3	1.1392	0.0095	0.0227	0.0460
			4	0.7504	0.0128	0.1106	0.1876
			5	0.1766	0.0002	0.0038	0.0078
			6	1.5960	0.0000	0.0002	0.0004
		0.24 ± 0.03	0		0.2497	0.3145	2.2593
			1	2.4896	0.1330	0.9912	0.1916
			2	0.2668	0.0175	0.0705	0.0161
			3	1.1857	0.0544	0.2697	0.2884
			4	2.1045	0.0417	0.2177	0.2731
			5	3.0233	0.0020	0.0138	0.0211
			6	0.8005	0.0002	0.0015	0.0022
		0.30 ± 0.03	0		0.4981	0.1660	1.9272
			1	2.5215	0.0954	0.7220	0.1634
			2	0.3306	0.0164	0.1523	0.3036
			3	1.2813	0.0582	0.3167	0.3910
			4	2.2320	0.0201	0.1191	0.1097
			5	0.0412	0.0008	0.0070	0.0183
			6	0.9919	0.0005	0.0031	0.0041
		0.36 ± 0.03	0		0.6391	0.2693	1.5945
			1	2.5280	0.0815	0.5727	0.4669
			2	0.3436	0.0917	0.4555	0.5709
			3	1.3008	0.0709	0.3516	0.4263
			4	2.2580	0.0396	0.1113	0.0822
			5	0.0737	0.0009	0.0004	0.0004
			6	1.0309	0.0025	0.0141	0.0184

$\tilde{e}$	ρ	T	j	ε_{2j}	$b_{2j}^{(0)}$	$b_{2j}^{(1)}$	$b_{2j}^{(2)}$
0.8	$(2.8 \pm 0.2)10^5$	0.18 ± 0.03	0		0.0115	0.2647	2.9136
			1	2.4509	0.1149	0.7983	0.0055
			2	0.1726	0.0212	0.1552	0.1653
			3	1.0800	0.0371	0.1283	0.1339
			4	1.5774	0.0983	0.7491	1.0921
			5	2.2915	0.0015	0.0037	0.0071
			6	0.2935	0.0008	0.0043	0.0055
		0.24 ± 0.03	0		0.2610	0.2543	2.3017
			1	2.4278	0.0908	0.7331	0.0750
			2	0.1410	0.0331	0.1628	0.0928
			3	1.0077	0.0132	0.0430	0.0249
			4	1.8104	0.1262	0.8661	1.2006
			5	2.6340	0.0013	0.0033	0.0096
			6	0.3817	0.0014	0.0084	0.0119
		0.30 ± 0.03	0		0.4882	0.1556	1.9542
			1	2.4635	0.0163	0.2257	0.7326
			2	0.2146	0.0670	0.2984	0.4502
			3	1.1073	0.0713	0.3961	0.4968
			4	2.0000	0.0172	0.1093	0.2111
			5	2.8927	0.0021	0.0157	0.0308
			6	0.6439	0.0013	0.0081	0.0116
		0.36 ± 0.03	0		0.6512	0.1735	1.7031
			1	2.4787	0.0969	0.6417	0.3247
			2	0.2451	0.2221	1.1143	1.1810
			3	1.1530	0.0151	0.1916	0.2381
			4	2.0610	0.1069	0.4262	0.4212
			5	2.9689	0.0046	0.0382	0.0611
			6	0.7352	0.0095	0.0547	0.0738

$\tilde{e}$	ρ	T	j	ε_{2j}	$b_{2j}^{(0)}$	$b_{2j}^{(1)}$	$b_{2j}^{(2)}$
0.9	$(1.6 \pm 0.2)10^5$	0.4 ± 0.05	0		0.8307	0.2635	1.1462
			1	2.7845	0.2213	0.8378	0.2087
			2	0.8504	0.0169	0.0198	0.0018
			3	2.2994	0.0445	0.2128	0.1827
			4	0.4919	0.2197	0.7424	0.5839
			5	1.5284	0.0140	0.0456	0.0307
			6	2.9625	0.0025	0.0088	0.0072
		0.5 ± 0.05	0		1.0052	0.3183	0.9006
			1	2.8180	0.1107	0.4629	0.0482
			2	0.8872	0.0416	0.1462	0.1143
			3	2.1717	0.0451	0.1202	0.0718
			4	2.0378	0.0711	0.2195	0.1372
			5	0.6968	0.0018	0.0074	0.0094
			6	0.9156	0.0008	0.0025	0.0020
		0.6 ± 0.05	0		1.2168	0.2361	0.7758
			1	2.7977	0.0826	0.3805	0.1004
			2	0.9193	0.0092	0.0557	0.0621
			3	2.1336	0.0440	0.0939	0.0441
			4	2.4834	0.0857	0.2716	0.1997
			5	0.4582	0.0009	0.0021	0.0014
			6	2.5272	0.0005	0.0014	0.0009
		0.7 ± 0.05	0		1.4017	0.1296	0.7303
			1	2.8218	0.2059	0.8342	0.2108
			2	0.9312	0.0995	0.3332	0.2389
			3	2.1822	0.1132	0.3194	0.2046
			4	0.2916	0.0282	0.0719	0.0592
			5	1.5426	0.0019	0.0061	0.0069
			6	2.7936	0.0033	0.0104	0.0073

$\tilde{e}$	ρ	T	j	ε_{2j}	$b_{2j}^{(0)}$	$b_{2j}^{(1)}$	$b_{2j}^{(2)}$
0.9	$(2.0 \pm 0.2)10^5$	0.4 ± 0.05	0		0.8641	0.1915	1.1712
			1	2.7390	0.3271	1.1822	0.4924
			2	0.7872	0.0478	0.1354	0.0883
			3	2.1548	0.0168	0.0598	0.0375
			4	1.7221	0.0546	0.1886	0.1444
			5	3.0666	0.0040	0.0123	0.0097
			6	0.9122	0.0011	0.0038	0.0028
		0.5 ± 0.05	0		0.9976	0.1870	0.9118
			1	2.7854	0.1114	0.4501	0.0393
			2	0.8813	0.0214	0.0377	0.0057
			3	2.0361	0.0230	0.0494	0.0206
			4	2.5299	0.0580	0.1758	0.1167
			5	0.7309	0.0018	0.0070	0.0067
			6	1.6692	0.0004	0.0013	0.0009
		0.6 ± 0.05	0		1.2268	0.1855	0.8075
			1	2.8596	0.0123	0.0885	0.2686
			2	0.8406	0.0034	0.0353	0.0488
			3	2.1235	0.0328	0.0676	0.0372
			4	1.8256	0.0778	0.2811	0.2199
			5	0.0678	0.0017	0.0076	0.0066
			6	2.8329	0.0002	0.0007	0.0005
		0.7 ± 0.05	0		1.3946	0.1250	0.7321
			1	2.8071	0.0918	0.4073	0.0677
			2	0.9017	0.0325	0.0568	0.0078
			3	2.1380	0.0053	0.0138	0.0202
			4	0.2327	0.0089	0.0503	0.0303
			5	1.4690	0.0002	0.0005	0.0022
			6	2.7052	0.0001	0.0003	0.0002

$\tilde{e}$	ρ	T	j	ε_{2j}	$b_{2j}^{(0)}$	$b_{2j}^{(1)}$	$b_{2j}^{(2)}$
0.9	$(2.4 \pm 0.2)10^5$	0.4 ± 0.05	0		0.8724	0.1469	1.2002
			1	2.7130	0.1550	0.6177	0.1340
			2	0.8478	0.0236	0.0535	0.0174
			3	0.7922	0.0988	0.3154	0.2170
			4	2.9145	0.0498	0.1526	0.1055
			5	0.7300	0.0029	0.0102	0.0080
			6	2.9247	0.0019	0.0061	0.0045
		0.5 ± 0.05	0		1.0490	0.1872	0.9711
			1	2.7363	0.1017	0.4171	0.0294
			2	0.7664	0.0876	0.2509	0.1303
			3	1.9679	0.0064	0.0411	0.0442
			4	0.4157	0.0582	0.1972	0.1313
			5	1.4637	0.0008	0.0023	0.0039
			6	2.7562	0.0014	0.0045	0.0033
		0.6 ± 0.05	0		1.2707	0.0741	0.8578
			1	2.7520	0.0163	0.1267	0.2233
			2	0.7915	0.0411	0.1260	0.0629
			3	1.9727	0.0091	0.0078	0.0004
			4	0.0122	0.0689	0.1936	0.1227
			5	1.1934	0.0003	0.0027	0.0036
			6	2.3746	0.0009	0.0030	0.0022
		0.7 ± 0.05	0		1.4258	0.0537	0.7536
			1	2.7515	0.0418	0.0083	0.2818
			2	0.7906	0.0192	0.0645	0.0153
			3	1.9714	0.0428	0.1514	0.0999
			4	0.0105	0.0240	0.1143	0.0849
			5	1.1912	0.0006	0.0033	0.0009
			6	2.3719	0.0003	0.0008	0.0006

$\tilde{e}$	ρ	T	j	ε_{2j}	$b_{2j}^{(0)}$	$b_{2j}^{(1)}$	$b_{2j}^{(2)}$
0.9	$(2.8 \pm 0.2)10^5$	0.4 ± 0.05	0		0.8902	0.0992	1.2273
			1	2.6738	0.1819	0.7564	0.2695
			2	0.6508	0.0549	0.1763	0.1275
			3	1.7436	0.1094	0.3282	0.2221
			4	2.5443	0.0647	0.1928	0.1362
			5	0.1709	0.0016	0.0063	0.0049
			6	1.8236	0.0033	0.0109	0.0080
		0.5 ± 0.05	0		1.0621	0.1626	0.9710
			1	2.6751	0.0424	0.2399	0.1145
			2	0.6578	0.0056	0.0677	0.0421
			3	1.6938	0.0064	0.0444	0.0394
			4	0.8425	0.1411	0.4719	0.3398
			5	0.4754	0.0010	0.0051	0.0055
			6	2.5215	0.0002	0.0005	0.0004
		0.6 ± 0.05	0		1.2517	0.1147	0.8353
			1	2.6947	0.0545	0.2760	0.0691
			2	0.7133	0.0443	0.1606	0.0910
			3	1.7280	0.0092	0.0209	0.0119
			4	1.9838	0.1020	0.3290	0.2416
			5	0.0346	0.0010	0.0041	0.0040
			6	1.0694	0.0013	0.0044	0.0032
		0.7 ± 0.05	0		1.4129	0.0712	0.7498
			1	2.6925	0.0030	0.1173	0.1972
			2	0.6725	0.0674	0.1579	0.1203
			3	1.7942	0.1417	0.3758	0.2259
			4	2.9159	0.0385	0.1335	0.1380
			5	0.8960	0.0045	0.0172	0.0182
			6	2.0176	0.0047	0.0150	0.0110

Appendix C

Three-Dimensional Simulations and Simulations with Spin

Here we present some results of three-dimensional simulations of free and simply sheared systems as well as results of two-dimensional simulations of shear flows with spin degrees of freedom. More detailed results of these simulations can be found in [16].
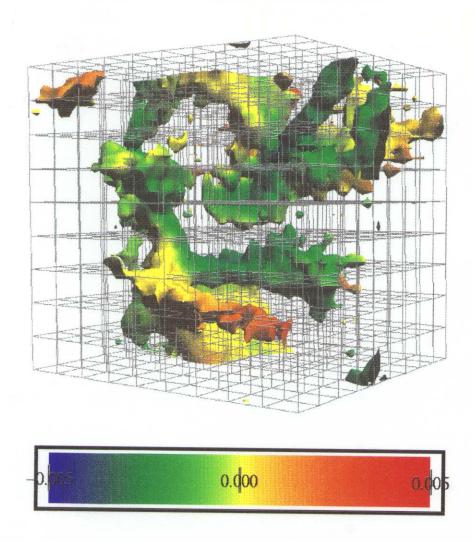
Figure C.1: Density isosurfaces of a three-dimensional dilute free flow in a periodic cubic enclosure after the transition to an inhomogeneous state. The parameters of the system are: $N = 120000, \nu = 0.05, \tilde{e} = 0.6$. The isosurfaces are colored according to the value of the streamwise velocity as indicated in the legend. Notice the dense meandering fingers of particles reminiscent of the dense wandering clusters observed in two-dimensional systems. The phenomenology of two-dimensional free flows appears to carry over to their three-dimensional counterparts.
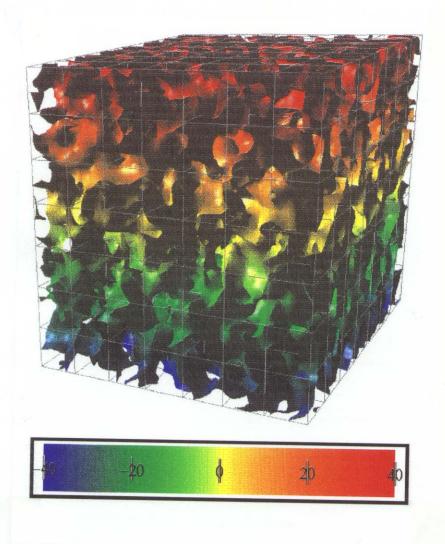
Figure C.2: Density isosurfaces of a three-dimensional dilute shear flow driven by the Lees-Edwards boundary conditions. The parameters of the system are: $N = 120000, \nu = 0.05, \tilde{e} = 0.6, U = \pm 100, L_x = L_y = L_z = 1$. The isosurfaces are colored according to the value of the streamwise velocity as indicated in the legend. The shearing is applied to the top and bottom boundaries with the top boundary moving to the right and the bottom boundary to the left. Notice the formation of *dense clusters* aligned at 45° to the streamwise direction, much like the clusters in a two-dimensional sheared system.
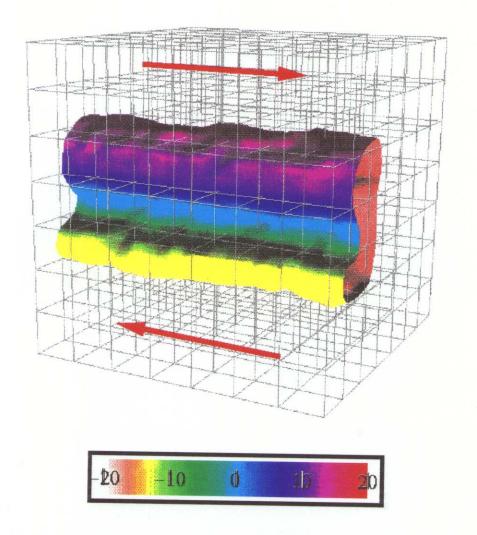
Figure C.3: Density isosurfaces of a three-dimensional dilute shear flow driven by the Lees-Edwards boundary conditions. The parameters of the system are: $N = 120000, \nu = 0.05, \tilde{e} = 0.6, L_x = L_y = L_z = 1$. The isosurfaces are colored according to the value of the streamwise velocity as indicated in the legend. The shearing is applied incrementally so that the velocity of the top and bottom boundaries increase (exponentially) from 0 to 50 over many collision times. The top boundary moves to the right and the bottom boundary to the left. Notice the formation of a dense streamwise plug in the center of the system. *This is the very first numerical observation ever in three-dimensional sheared systems of plug formation.*
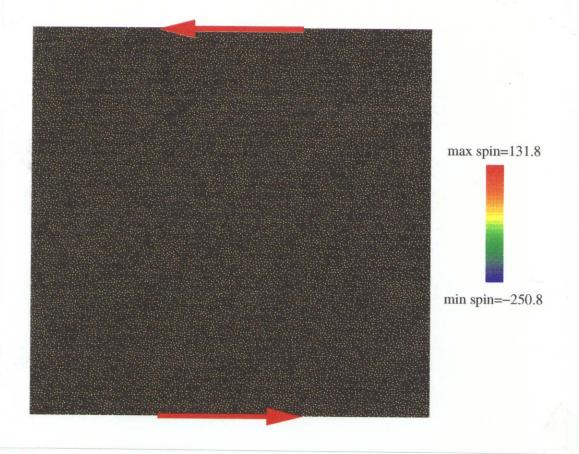
Figure C.4: Particle configuration plot for a simple shear flow with rotational degrees of freedom. The color of a particle depends on its angular velocity as indicated by the legend. The parameters of the system are: $N = 20000$, $\nu = 0.05$, $\tilde{e} = 0.6$ and $\beta = -0.8$ (β is the coefficient of tangential restitution; the collision model may be found in Ref. [8]). Notice the heterogeneous distribution of spins within the system. The origin of this heterogeneity lies in the fact that spinning particles close together will tend to align their spins in opposite directions so as to minimize the dissipation of rotational kinetic energy. Spin degrees of freedom may also play a role in reducing the density inhomogeneities in the system.
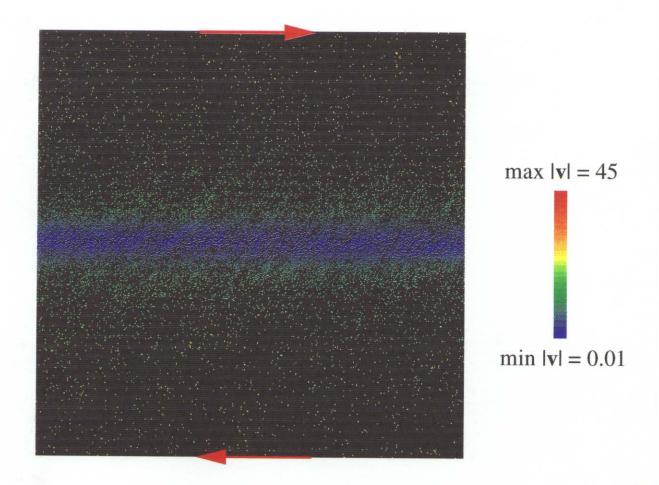
Figure C.5: Particle configuration plots for a wall-bounded shear flow driven by two flat frictional walls at the top and bottom moving in opposite directions with equal speed. The color of a particle depends on the magnitude of its velocity as indicated by the legend. The parameters of the system are: $N = 20000$, $\nu = 0.05$, $\tilde{e} = 0.9$ and $\beta = -0.8$. The collisions of particles with the moving walls are characterized by normal and tangential restitution coefficients equal to 0.8 and -0.8 respectively. Notice the formation of a dense streamwise plug of low internal kinetic energy similar to the plug in a simple shear flow driven from a static initial condition.

Bibliography

[1] R.P. Behringer. The dynamics of flowing sand. *Nonlinear Science Today*, 3(3):1–15, 1993.

[2] C.S. Campbell. Rapid granular flows. *Ann. Revs. Fluid Mech.*, 22:57–92, 1990.

[3] P.K. Haff. A physical picture of kinetic granular fluids. *J. Rheology*, 30(5):931–948, 1986.

[4] P.K. Haff. Grain flow as a fluid-mechanical phenomenon. *J. Fluid Mech.*, 134:401–430, 1983.

[5] J.T. Jenkins and M.W. Richman. Grad's 13-moment system for a dense gas of inelastic spheres. *Arch. Rat. Mech. Anal*, 87:355–377, 1985.

[6] J.T. Jenkins and M.W. Richman. Kinetic theory for plane flows of a dense gas of identical, rough, inelastic, circular disks. *Phys. Fluids*, 28:3485–3494, 1985.

[7] C.K.K. Lun and S.B. Savage. A simple kinetic theory for granular flow of rough inelastic spherical particles. *J. Appl. Mech.*, 154:47–53, 1987.

[8] C.K.K. Lun. Kinetic theory for granular flow of dense, slightly inelastic, slightly rough spheres. *J. Fluid Mech.*, 223:539–559, 1991.

[9] C.S. Campbell and A. Gong. The stress tensor in a two-dimensional granular shear flow. *J. Fluid Mech.*, 164:107–125, 1986.

[10] C.S. Campbell. The stress tensor for simple shear flows of a granular material. *J. Fluid Mech.*, 203:449–473, 1989.

[11] S. McNamara and W.R. Young. Inelastic collapse and clumping in a one-dimensional granular medium. *Phys. Fluids*, A4:496–504, 1992.

[12] S. McNamara and W.R. Young. Kinetics of a one dimensional granular medium in the quasielastic limit. *Phys. Fluids*, A5:34–45, 1993.

[13] N. Sela and I. Goldhirsch. Hydrodynamics of a one dimensional granular medium. *Phys. Fluids*, 7(3):507, 1995.

[14] O. Zik, D. Levine, S.G. Lipson, S. Shtrikman, and J. Stavans. Rotationally induced segregation of granular materials. *Phys. Rev. Lett.*, 73(5):644, 1994.

[15] H.J. Herrmann. Simulation of granular media. *Physica A*, 191:263–276, 1992.

[16] M-L. Tan and I. Goldhirsch. unpublished results. 1995.

[17] P. Bak, C. Tang, and K. Weisenfeld. Self-organized criticality: An explanation of 1/f noise. *Phys. Rev. Lett.*, 59:381–384, 1987.

[18] A. Mehta. Relaxational dynamics. avalanches, and disorder in real sandpiles. In *Granular Matter*, pages 1–33, 1993.

[19] R.L. Brown and J.C. Richards. *Principles of Powder Mechanics*. Pergamon, London, 1970.

[20] P.C. Johnson, P. Nott, and R. Jackson. Frictional-collisional equations of motion of particulate flows and their applications to chutes. *J. Fluid Mech.*, 210:501–535, 1990.

[21] H.M. Jaeger and Sidney R. Nagel. Physics of the granular state. *Science*, 255:1523, 1992.

[22] O.R. Walton and R.L. Braun. Stress calculations for assemblies of inelastic spheres in uniform shear. *Acta Mechanica*, 63:73–86, 1986.

[23] S. Araki. The dynamics of particle discs II: Effects of spin degrees of freedom. *Icarus*, 76:182–198, 1988.

[24] J.T. Jenkins and E. Askari. Rapid granular shear flows driven by identical, bumpy, frictionless boundaries. In S.I. Plasynski, W.C. Peters, and M.C. Roco, editors, *Proceedings of the Joint DOE/NSF Workshop on Flow of Particulates and Fluids*, W.P.I., Worcester, Mass., Oct 1991.

[25] Ted M. Knowlton, John W. Carson, George E. Klinzing, and Wen-Ching Yang. Particle technology: The importance of storage, transfer and collection. *Chemical Engineering Progress*, April:44, 1994.

[26] Thorsten Pöschel. Granular material flowing down an inclined chute: A molecular dynamics simulation. *J. Phys. II France*, 3:27–40, 1993.

[27] C.S. Campbell and C.E. Brennan. Chute flows of granular material: some computer simulations. *Trans. of the ASME: J. Appl. Mech.*, 52:172–178, 1985.

[28] R.H. Weiland, Y.P. Fessas, and B.V. Ramarao. On instabilities arising during sedimentation of two-component mixtures of solids. *J. Fluid Mech.*, 142:383–389, 1984.

[29] G.K. Batchelor and R.W. Janse van Rensburg. Structure formation in bidisperse sedimentation. *J. Fluid Mech.*, 166:379–407, 1986.

[30] J. R. Grace and J. Tuot. A theory for cluster formation in vertically conveyed suspensions of intermediate density. *Trans. Inst. Chem. Eng.*, 57(1):49, 1979.

[31] J.F. Brady and G. Bossis. Stokesian dynamics. *Ann. Revs. Fluid Mech.*, 20:111–157, 1988.

[32] R. Jackson. Hydrodynamic stability of fluid particle systems. In J.F. Davidson, R. Clift, and D. Harrison, editors, *Fluidization*. Academic, 1985.

[33] S. Dasgupta, R. Jackson, and S. Sundaresan. Turbulent gas-particle flow in vertical risers. *AIChE Journal*, 40(2):215, 1994.

[34] B.J. Glasser, I.G. Kevrekidis, and S. Sundaresan. One- and two-dimensional traveling wave solutions in gas-fluidized beds. submitted to J. Fluid Mech., 1995.

[35] S. McNamara. Inelastic collapse in two dimensions. *Phys. Rev. E*, 50:R28, 1994.

[36] M.A. Goodman and S.C. Cowin. A continuum theory for granular materials. *Arch. Rat. Mech. and Anal.*, 44:249–266, 1972.

[37] S. Chapman and T.G. Cowling. *The mathematical theory of nonuniform gases.* Cambridge U. P., 3rd ed. edition, 1970.

[38] P. Goldreich and S. Tremaine. The velocity dispersion in Saturn's rings. *Icarus*, 34:227–239, 1978.

[39] J.T. Jenkins and M.W. Richman. Plane simple shear of smooth inelastic circular disks: the anisotropy of the second moment in the dilute and dense limits. *J. Fluid Mech.*, 192:313–328, 1988.

[40] M.A. Hopkins and M.Y. Louge. Inelastic microstructure in rapid granular flows of smooth disks. *Phys. Fluids*, A3(1):47–57, 1991.

[41] M. Nakagawa, S.A. Altobelli, A. Caprihan, E. Fukushima, and E.-K. Jeong. Non-invasive measurements of granular flows by magnetic resonance imaging. *Experiments in Fluids*, 16:54–60, 1993.

[42] M-L. Tan, Y. H. Qian, I. Goldhirsch, and S. A. Orszag. Lattice-BGK approach to simulating granular flows. submitted to J. Stat. Phys., 1994.

[43] A.W. Lees and S.F. Edwards. The computer study of transport processes under extreme conditions. *J. Phys. C: Solid State Phys.*, 5:1921–1929, 1972.

[44] O.R. Walton and R.L. Braun. Viscosity and temperature calculations for shearing assemblies of inelastic, frictional disks. *J. Rheology*, 30:949–980, 1986.

[45] J.T. Jenkins. Boundary conditions for rapid granular flow: Flat, frictional walls. *Trans. of the ASME: J. Appl. Mech.*, 59:120, 1992.

[46] J.W. Duffy, J.J. Brey, and A. Santos. Some theoretical aspects of nonequilibrium simulation methods. In *Molecular-Dynamics Simulation of Statistical-Mechanical*

Systems: Varenna on Lake Como, Villa Monastero, 23 July-2 August 1985, pages 294–303, 1986.

[47] J.T. Jenkins and M.W. Richman. Grad's 13-moment system for a dense gas of inelastic spheres. *Arch. Rat. Mech. Anal*, 87:355–377, 1985.

[48] Schmid, P.J. and Kytömaa, H.K. Transient and asymptotic stability of granular shear flow. *J. Fluid Mech.*, 264:255–275, 1994.

[49] S.B. Savage. Instability of an unbounded uniform granular shear flow. *J. Fluid Mech.*, 241:109–123, 1992.

[50] M. Babic. On the stability of rapid granular flows. *J. Fluid Mech.*, 254:127–150, 1993.

[51] J.T. Jenkins and M.W. Richman. Kinetic theory for plane flows of a dense gas of identical, rough, inelastic, circular disks. *Phys. Fluids*, 28:3485–3494, 1985.

[52] C.K.K. Lun, S.B. Savage, D.J. Jeffrey, and N. Chepurnyi. Kinetic theories of granular flow: Inelastic particles in a couette flow and slightly inelastic particles in a general flow field. *J. Fluid Mech.*, 140:223–256, 1984.

[53] S. McNamara. Hydrodynamic modes of a uniform granular medium. *Phys. Fluids*, A5:3056–3070, 1993.

[54] M.A. Hopkins and H.H. Shen. A Monte-Carlo solution for rapidly shearing granular flows based on kinetic theory of dense gases. *J. Fluid Mech.*, 244:477–491, 1992.

[55] D.C. Rapaport. The event scheduling problem in molecular dynamics simulation. *J. Comp. Phys.*, 34:184–201, 1980.